NON-COVALENT INTERACTIONS IN ASYMMETRIC ORGANOCATALYSIS

A Dissertation

by

TREVOR JAMES SEGUIN

Submitted to the Office of Graduate and Professional Studies of
Texas A&M University
in partial fulfillment of the requirements for the degree of

DOCTOR OF PHILOSOPHY

Chair of Committee,	Steven E. Wheeler
Committee Members,	Robert R. Lucchese
	Perla B. Balbuena
	Lei Fang
Head of Department,	Simon W. North

December 2016

Major Subject: Chemistry

ABSTRACT

The stereochemical outcomes of asymmetric organocatalytic reactions are the result of myriad competing forces in the stereocontrolling transition states (TSs). An often potent factor governing stereoselectivity are differential non-covalent interactions, which modern computational techniques make possible to examine in detail. Studies of the origins of stereoselectivity in asymmetric organocatalytic reactions not only uncover key information regarding the mode of asymmetric induction, such as the strength of various non-covalent interactions, but can also inform future rational catalyst design.

In the first part of this dissertation, an analysis of the stereoselectivity in the first example of a stereoselective, catalytic Fischer indole synthesis, utilizing chiral phosphoric acid catalysts, shows that selectivity results from competition between CH/π and π/π interactions in the lowest-lying transition states. In the second part, a general model is presented for the stereoselectivity of chiral phosphoric acid-catalyzed *meso*-epoxide ring-openings, in which the lowest-lying transition state structure contains a favorable electrostatic CH···O interaction due to the stereospecific restriction of substrate orientations. In the third part, it is shown that a complex, variable interplay of non-covalent interactions are responsible for the stereoselectivity in chiral phosphoric acid-catalyzed enantioselective oxetane desymmetrizations. Finally, it is shown in a recent example of ion-pairing organocatalysis of a Diels-Alder reaction, that both dispersion and electrostatic-based interactions control the selectivity, the former as a result of cyclopentadiene nestled in a cleft between the dienophile and aromatic

backbone of the catalyst, and the latter as a result of stronger CH···O interactions between the cationic substrate and the anionic catalyst core in the favored transition state.

DEDICATION

To my wife, and son.

ACKNOWLEDGEMENTS

I would like to thank my advisor, Dr. Wheeler, for the opportunity to work in his group. He is an excellent mentor and professor, and I enjoyed working with him. I am grateful to Dr. Lucchese, Dr. Fang and Dr. Balbuena for serving on my committee.

Thanks to all of my professors through the years who have been involved in my chemical education and/or research; Dr. Zozulin, Dr. Westcott, Dr. Burkholder, Dr. DeYonker, and Dr. Webster in particular.

Thanks to my wonderful wife for her love and support.

CONTRIBUTORS AND FUNDING SOURCES

Contributors

This work was supervised by a dissertation committee consisting of Professor Steven E. Wheeler (advisor and committee chair), and Professors Robert R. Lucchese and Lei Fang of the Department of Chemistry, and Professor Perla B. Balbuena of the Department of Chemical Engineering.

Experimental data in Chapters II and V were published previously by Professor Benjamin List, and experimental data in Chapter IV were published previously by Professor Jianwei Sun. Chapter III contains experimental data published previously by both Professors Benjamin List and Jianwei Sun.

All other work in the dissertation was conducted independently by the student under the supervision of Steven E. Wheeler.

Funding Sources

The work in this dissertation was supported by The Welch Foundation (Grant A-1775) and the National Science Foundation (Grant CHE-1266022).

TABLE OF CONTENTS

Page

LIST OF FIGURES

Page

LIST OF TABLES

Page

CHAPTER I

INTRODUCTION

Since approximately the late 1990s, there has been a tremendous surge of interest in asymmetric organocatalysis, or the use of small transition-metal-free organic molecules to carry out enantioselective transformations.[1] This method of asymmetric catalysis is advantageous over traditional metal-based approaches for reasons related to cost, availability, environmental friendliness, and ease of use. For example, chiral phosphoric acids are being implemented in enantioselective syntheses of an ever-increasing range of desirable chemical functionalities.[2] These catalysts, which are derived from various chiral diols and feature highly adjustable substituents in the 3,3′-positions, typically play a bifunctional role in the mode of asymmetric induction by binding the substrates to both its Brønsted acidic and basic sites. In general, for reactions involving these catalysts, the Brønsted acid functionality activates the electrophile by either hydrogen bonding or a proton transfer prior to attack by the nucleophile which may be bound to the adjacent phosphoryl oxygen. Stereoselectivity arises from factors resulting from restricted substrate orientations within the chiral environment of the catalyst. Another burgeoning subarea of organocatalysis is asymmetric counterion-directed catalysis (ACDC), a term coined by Benjamin List referring to asymmetric organocatalysis in which chiral anions induce stereoselectivity while ion-paired with cationic substrates undergoing reaction.[3]

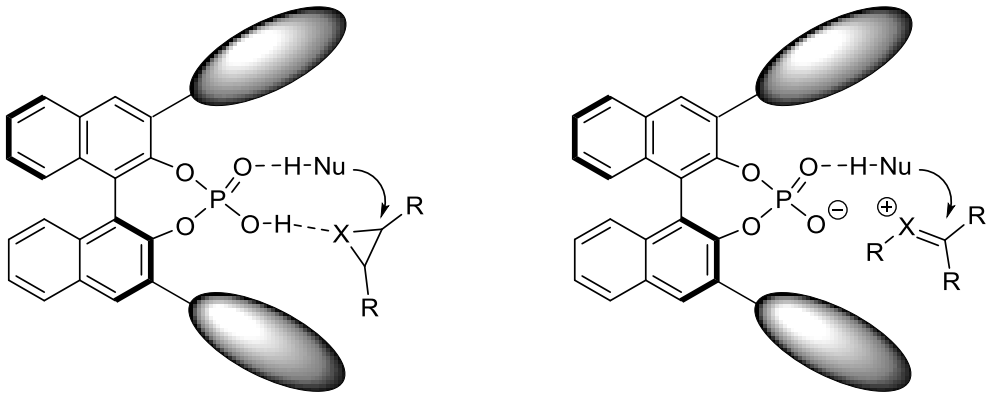

Chiral Brønsted Acid Catalysis Chiral Anion Catalysis

Figure I-1. Two popular strategies for asymmetric organocatalysis.

Though the field of asymmetric organocatalysis continues to flourish, insight into the mechanisms and origins of stereoselectivity of the transformations therein has not kept pace. Such information could be invaluable towards the future guidance of rational catalyst design. The work in this dissertation seeks to aid in this area in the form of theoretical investigations of several examples of asymmetric organocatalytic reactions using density functional theory (DFT) calculations.[4] These calculations can offer an intimate look at the mode of asymmetric induction by modelling the competing transition states (TS) leading to the different stereochemical outcomes.

Plausible transition state models are commonly based on the assumption that there are more steric repulsions between the substrate and catalyst in the disfavored transition state corresponding to the minor observed stereoisomer product. However, one crucial factor that can guide stereoselectivity is the net effect of many competing non-covalent interactions,[5] which is the focus of the work in this dissertation. Non-covalent

interactions are relatively weak, long range attractive interactions. Dispersion-driven interactions, originating in correlated fluctuations of the electron distributions of interacting species, are abundant in organocatalysis, especially those involving aromatic rings (See Figure I-II for prototypical examples of such interactions). Other interactions of importance include those which are electrostatic in origin, such as classical OH···O and non-classical CH···O hydrogen bonds.[6]

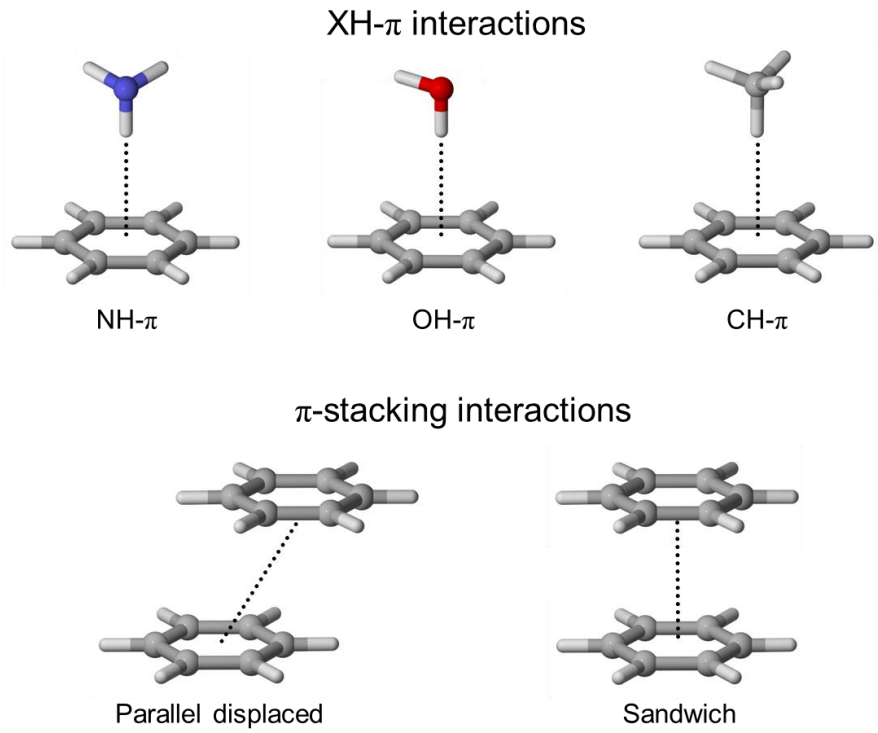

Figure I-2. Prototypical non-covalent interactions involving aromatic rings.

The failure of conventional DFT functionals to adequately describe dispersion-based interactions is well documented.[7] Therefore, the improvement of DFT to account for these interactions has been a subject of intense research interest in the last decade. One of the most popular methods in this area is the DFT-D method of Grimme.[8] In this approach, dispersion interactions are accounted for by a sum of pairwise terms which depend on the atom type and interatomic distance,

$$E_{disp} = -\sum_{i=1}^{N-1}\sum_{j=i+1}^{N}\frac{C_6^{ij}}{R_{ij}^6}f_{damp}(R_{ij}),$$

where f_{damp} is a damping function that smoothly reduces the dispersion correction to zero at close interatomic distances, and the C_6 coefficients are predefined for each functional from fitting to high accuracy data. The simple form of this "dispersion correction" can be calculated with essentially no computational cost and simply added onto the DFT energy,

$$E_{DFT-D} = E_{DFT} + E_{disp}.$$

When implemented in e.g. the B97-D[8] and wB97X-D[9] functionals, the reference values for the interaction energies of non-covalently bound complexes are reproduced with very good accuracy.[8, 10] The DFT-D3 methods that followed were an improvement on this scheme and are some of the most accurate and cost-effective approaches to modeling non-covalent interactions to date.[11] The functionals used for the work in this dissertation are mainly this type. We have also used M06-2X from the Minnesota suite of functionals,[12] which is also a respectable performer with regard to non-covalent interactions.[13] The origin of its performance in this regard is due to the form of the

functional containing a large number of parameters modeled in part from reference complexes containing non-covalent interactions.

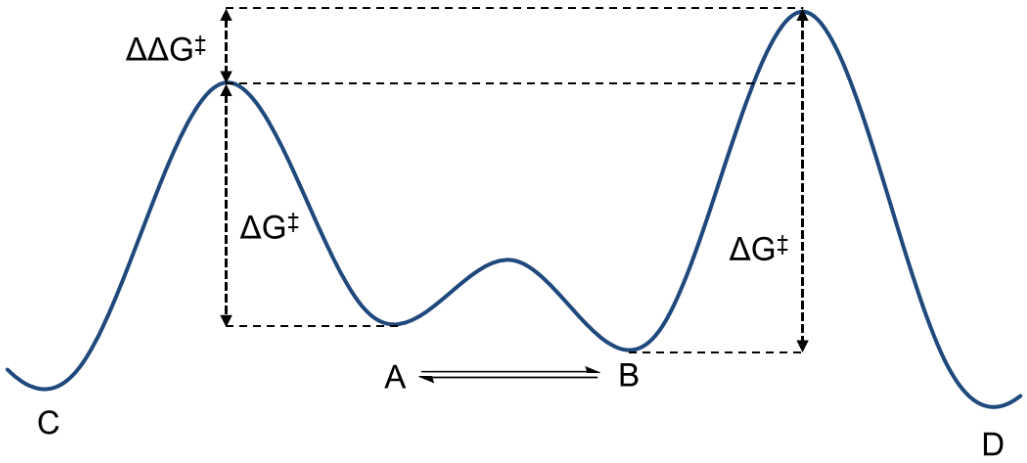

Figure I-3. Curtin-Hammett scenario. A and B are in rapid equilibrium, so the distribution of C and D only depends on the difference in free energy of the transition states leading to each product, $\Delta\Delta G^{\ddagger}$.

In many cases, the relative distribution of the different stereoisomeric products of a reaction can be assumed to follow the Curtin-Hammett principle[14] which, briefly, states that the distribution of products depends not on the distribution of possible reactant configurations (e.g. as different non-bonded reactant complexes) when their interconversions are separated by relatively small barrier heights, but rather the difference in free energies of the transition states leading to the those products, $\Delta\Delta G^{\ddagger}$.

From classical transition state theory (TST),[15] the enantiomeric ratio (*er*) can be related to the difference in free energy of the transition states as

$$er = e^{\frac{\Delta\Delta G^{\ddagger}}{RT}},$$

where *R* is the ideal gas constant and *T* is the temperature.

When modelling the competing transition states of stereoselective reactions, it is imperative to find the lowest energy structure leading to each corresponding stereoisomer product. The challenge in this undertaking can be considerable, as 100s or 1000s of conformations can be possible in modern organocatalytic systems, which are often rather large (~100-150 atoms) and flexible. Considerable effort has been put into the conformation searches of all catalytic systems in the work of this dissertation, using some combination of automatic conformation search methods (e.g. by the MacroModel program[16]) and preparations/adjustments of structures "by hand" in molecular editing programs.

With the lowest-lying structures in hand, analyses on the origin of stereoselectivity can begin with a variation of the distortion-interaction model of Houk and co-workers.[17] In this model, the gas-phase difference in energy is decomposed as the difference in interaction energy (here, the interaction energy is defined as the difference in energy between an intact catalytic system and the sum of the energies of the separated substrates and catalyst) and the difference in energy of the distorted substrates and catalyst in the TS geometries as

$$\Delta\Delta E^{\ddagger} = \Delta\Delta E_{int} + \Delta\Delta E_{cat} + \Delta\Delta E_{sub}.$$

The difference in interaction energy captures the difference in non-covalent interactions between the substrates and catalyst in the competing transition states, while the difference in catalyst and substrate energies captures the difference in distortion energies for these species (though the "distortion energy" contains a significant difference in intramolecular interactions in some cases; these need to be recognized and accounted for appropriately). To isolate particular non-covalent interactions contained in $\Delta\Delta E_{int}$, we can take the structures and create a series of truncated models in which structural components are trimmed and replaced with hydrogen atoms which are optimized while all other atoms are fixed. Then the interaction energies of each of these models reflects only the interactions isolated to each particular model, and the sum of each of these terms approximately sums to the total difference in interaction energy,

$$\Delta\Delta E_{int} \approx \Delta\Delta E_{int}(M1) + \Delta\Delta E_{int}(M2) + \Delta\Delta E_{int}(M3) + \ldots$$

where M1, M2, M3, … are the truncated model systems.

In the chapters that follow, we apply these methods to enantioselective Fischer indolization reactions (Chapter II), the asymmetric openings of meso-epoxides (Chapter III) and oxetanes (Chapter IV), and to the ACDC of the Diels-Alder cycloaddition of cyclopentadiene to cinnamates (Chapter V).

CHAPTER II

ENANTIOSELECTIVITY IN CATALYTIC ASYMMETRIC FISCHER INDOLIZATIONS HINGES ON THE COMPETITION OF Π-STACKING AND CH/Π INTERACTIONS[*]

The use of phosphoric acids derived from chiral diols in organocatalysis has exploded since their introduction a decade ago.[2, 18] However, for many such reactions, the mode of asymmetric induction is not fully understood, hindering the rational design of new catalysts. Herein, we use modern computational tools to unravel the impact of competing CH/π and π-stacking interactions on enantioselectivity in the first catalytic asymmetric Fischer indolization[19].

The Fischer indole reaction[20] provides a popular route to indoline frameworks that occur widely in natural products.[21] However, until recently, there were no asymmetric versions of this reaction that were also catalytic. This changed in 2011, when List *et al.*[19] reported the first catalytic asymmetric indolization, using a chiral phosphoric acid catalyst derived from SPINOL (**1**, Scheme II-1).[22] This provided a simple, mild, and efficient method for the enantioselective synthesis of highly diverse indoline scaffolds from simple starting materials. Their initial report utilized **1a** to catalyze the conversion of the *N*-protected hydrazone formed by the condensation of phenylhydrazines and 3-substituted cyclohexanones to the corresponding 3-substituted

[*] Adapted with permission from "Enantioselectivity in Catalytic Asymmetric Fischer Indolizations Hinges on the Competition of π-Stacking and CH/π Interactions" by T. J. Seguin, T. Lu, and S. E. Wheeler, 2015. *Org. Lett.* **17**, 3066. Copyright 2015 American Chemical Society.

tetrahydrocarbazoles [equation 2.1].[19] Reported *er*'s generally exceeded 90:10 across a broad range of substrates. Other, similar catalysts, including **1b** and **1c**, as well as BINOL-derived catalysts such as **2b** and **2c**, provided significantly lower *er*'s for this reaction (see Table II-1).

List *et al*.[23] later showed that SPINOL-derived phosphoric acids could also catalyze equation 2.2 to provide access to 3,3-disubstituted fused indolines. However, for these transformations, **1d** provided higher enantioselectivities than **1a**. Most recently, List and co-workers[24] showcased the utility of catalytic asymmetric indolizations in the first organocatalytic synthesis of helicenes [equation 2.3]. In this case, **1a** and **1d** proved sub-optimal, and **1e** provided the highest *er*'s of the catalysts tested.[24]

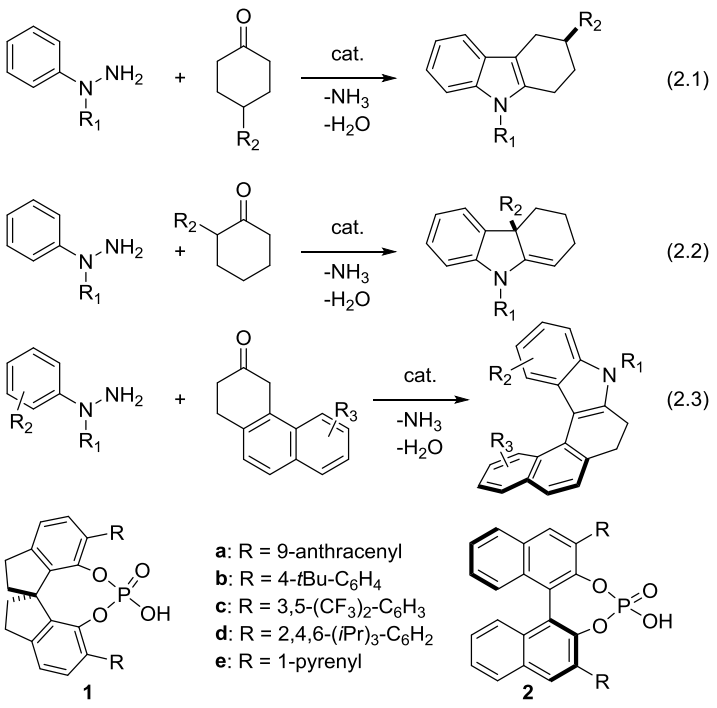

Scheme II-1

That enantioselectivities in these Fischer indolizations[19, 23-24] are highly sensitive to the identity of the pendant aryl groups suggests that subtle non-covalent interactions between the substrate and these aryl groups play a central role in enantioselectivity; identifying these non-covalent interactions is vital for the rational design of improved catalysts. Although pinpointing such interactions through experiment alone remains a challenge, computational quantum chemistry can provide key insights in such cases by identifying the non-covalent interactions at play in the stereocontrolling transition states (TSs).[5a, 25] Unfortunately, the impact of individual non-covalent interactions on the relative energies of competing transition states is rarely quantified.[25b, 26]

The first reliable computational study of Brønsted-acid promoted Fischer indolizations was not published until 2011, by Houk *et al*.[27] Others have used computations to study related acid-catalyzed [3,3]-sigmatropic rearrangements in recent years,[28] building on the work of Goodman *et al*.[29] on chiral phosphoric acid catalyzed reactions. This includes recent work by Ess, Kürti, *et al.*,[28a] as well as Tantillo and Tambar.[28b] Here, we use modern computational tools to quantify the impact of non-covalent interactions responsibe for the enantioselectivity of **1a** in the catalysis of equation 2.1 (R_1 = Bn, R_2 = Ph).

Table II-1. Experimental er's (S:R), corresponding free energy barrier differences (kcal mol^{-1}), and predicted relative free energy barriers for equation 2.1 catalyzed by 1a-c and 2b-c.[a]

cat.	exptl. *er*[b]	exptl. $\Delta\Delta G^{\ddagger}$	theor. $\Delta\Delta G^{\ddagger}$
1a	93.5:6.5	1.6	2.7
1b	43.5:56.5	–0.2	–0.1
1c	48.5:51.5	0.0	–0.9
2b	40.5:59.5	–0.2	–0.2
2c	59.5:40.5	0.2	0.1

[a] $\Delta\Delta G^{\ddagger} = \Delta G^{\ddagger}(R) - \Delta G^{\ddagger}(S)$ for the lowest-lying (*R*) and (*S*) transition states.
[b] 5% catalyst at 30 °C in benzene.[19]

The stereocontrolling step in acid catalyzed Fischer indolizations is the [3,3]-sigmatropic rearrangement of the protonated ene-hydrazine arising from the tautomerization of the protonated hydrazone (Scheme II-2).[23, 28a, 30] List *et al.*[19] proposed that the enantioselectivity for the catalysis of equation 2.1 by **1a** arises from the more rapid [3,3]-sigmatropic rearrangement of one of the two diastereomeric ion pairs formed by the deprotonated catalyst and protonated ene-hydrazine. This is justified by the lack of C–C bond rotation in the resulting intermediate, as shown by Ess and Kürti.[28a]

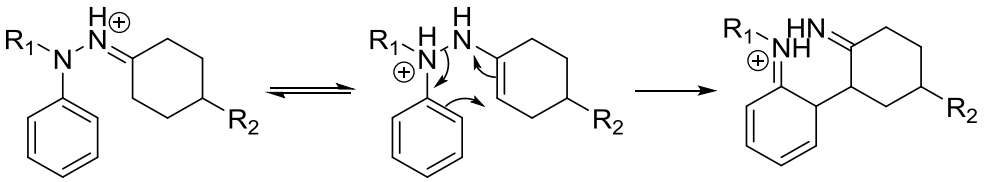

Scheme II-2

To understand the origin of enantioselectivity in these reactions, computations were performed using Gaussian 09[31] at the ωB97X-D/6-311+G(d,p)//ωB97X-D/6-31G(d) level of theory.[9] This level of theory provides reliable predictions of reaction barriers for acid-catalyzed [3,3]-sigmatropic shifts, compared to recent benchmark values from Houk *et al.*,[27] while also capturing the subtle, dispersion-dominated non-covalent interactions that underlie the enantioselectivity of the studied catalytic reaction. Solvent effects (benzene) were accounted for in all computations (except where noted) using CPCM[32] with UAKS radii. Thermal free energy corrections were obtained at 303K using standard rigid-rotor/harmonic oscillator approximations to compute partition functions. Structures were verified to be transition states based on the existence of a single imaginary vibration frequency.

In the presence of **1a**, we find that protonation of the ene-hydrazine preceding the [3,3]-sigmatropic rearrangement is exergonic by 6.7 kcal mol^{-1}. This proton transfer is crucial for reducing the activation energy of the rearrangement, consistent with previous work from Houk *et al.*[27] and Kürti *et al.*[28a] Following an extensive search of low-lying TS structures for this [3,3]-sigmatropic rearrangement catalyzed by **1a**, we identified the

low-lying transition states responsible for formation of the (*S*) and (*R*) products (see Figure II-1).

In TS_{1a}(*S*), the protonated substrate exhibits two NH-donated hydrogen bonds to the phosophoric acid, as expected.[19] On the other hand, TS_{1a}(*R*) features only one NH-donated hydrogen-bond. The other NH is directed towards one of the 9-anthracenyl substituents of the catalyst, although it is not in a position to engage in a favorable NH/π interaction.[a] The impact of these qualitative differences in hydrogen-bonding motifs on the enantioselectivety will be discussed below. Overall, we find that TS_{1a}(*R*) is 2.7 kcal mol^{-1} higher in free energy than TS_{1a}(*S*), which is a slight overestimation of the experimental enantioselectivity.[19] Computations provide even more reliable predictions for catalysis of equation 2.1 by other chiral phosphoric acid catalysts (see Table II-1). In particular, both the overall sense of stereoinduction and the magnitude of enantioselectivity are predicted very accurately for all but **1c**. In the case of **1c**, we predict modest enantioselectivity whereas this catalyst was found to be unselective experimentally. Surprisingly, it is only for **2c** that the low-lying TS structures are structurally similar to those for **1a**.

[a] The free energy of the lowest-lying (R)-transition state featuring dual NH-donated hydrogen bonds to the phosophoric acid is 7.3 kcal mol^{-1}, relative to TS1a(S).

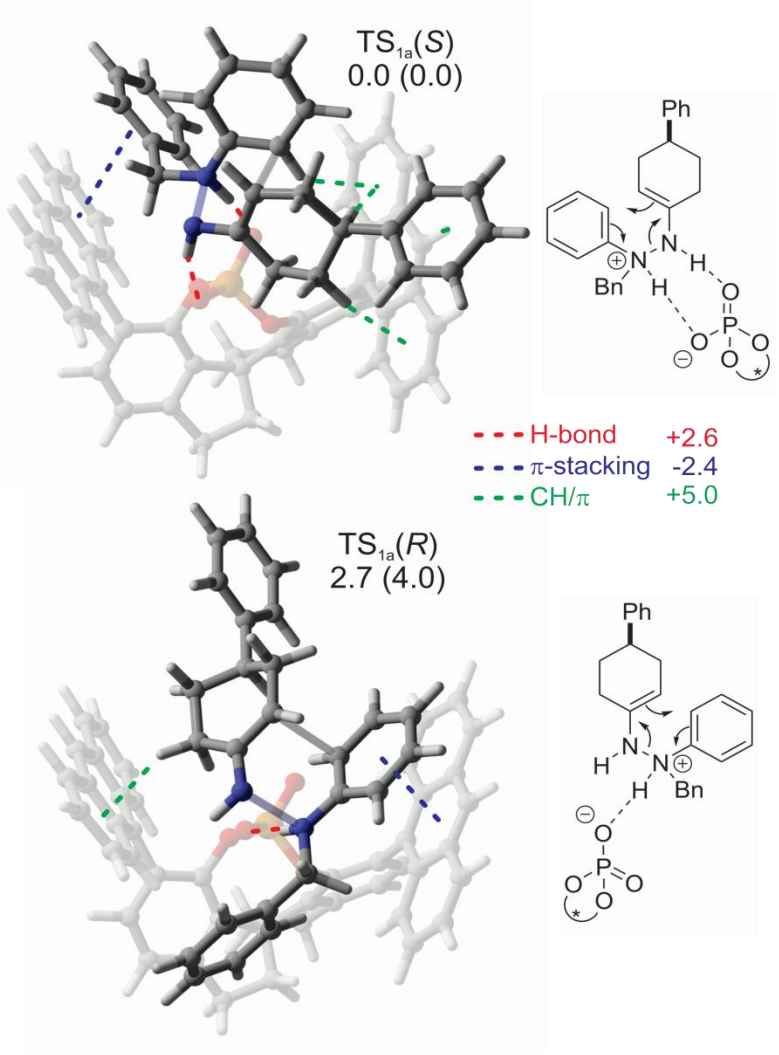

Figure II-1. Lowest-lying [3,3]-sigmatropic rearrangement transition state structures leading to the (*S*) and (*R*) products for equation 2.1 catalysed by **1a**. Solution-phase relative free energies are provided, in kcal mol^{-1} (relative gas-phase energies, $\Delta\Delta E^{\ddagger}$, are given in parentheses). Key non-covalent interactions between substrate and catalyst are denoted with dashed lines. Approximate contributions of these interactions to $\Delta\Delta E^{\ddagger}$ are shown in kcal mol^{-1}.

Qualitatively, it is already apparent from Figure II-1 that the structure of the substrate in $TS_{1a}(S)$ is more complementary to the chiral binding pocket of the catalyst,

compared to that in $TS_{1a}(R)$. To understand the origin of the 2.7 kcal mol^{-1} difference in free energy between $TS_{1a}(R)$ and $TS_{1a}(S)$, we first note that the gas-phase energy difference, $\Delta\Delta E^{\ddagger}$, is 4.0 kcal mol^{-1}. In other words, entropic and solvent effects reduce the energy gap between these transition states by 1.3 kcal mol^{-1}. This 4.0 kcal mol^{-1} difference in gas-phase energies between $TS_{1a}(R)$ and $TS_{1a}(S)$ can be decomposed into three components,[b]

$$\Delta\Delta E^{\ddagger} = \Delta\Delta E_{sub} + \Delta\Delta E_{cat} + \Delta\Delta E_{int},$$

where $\Delta\Delta E_{sub}$ is the difference in energy between the protonated ene-hydrazine substrate in the $TS_{1a}(R)$ and $TS_{1a}(S)$ geometries; $\Delta\Delta E_{cat}$ is the energy difference of the catalyst in these TS geometries; and $\Delta\Delta E_{int}$ is the difference in interaction energies between the catalyst and substrate in these TS geometries. These components of $\Delta\Delta E^{\ddagger}$ are depicted in Figure II-2a.

First, we note that $\Delta\Delta E_{sub}$ is negative—the substrate in $TS_{1a}(R)$ is 1.5 kcal mol^{-1} lower in energy than that in $TS_{1a}(S)$. This presumably arises from the more favorable *anti* conformation of the benzyl substituent in $TS_{1a}(R)$, compared to the *gauche* conformer in $TS_{1a}(S)$ (see SI for more details). These effects are overshadowed by the +4.8 kcal mol^{-1} difference in $\Delta\Delta E_{int}$, which, when combined with the +0.7 kcal mol^{-1} contribution from $\Delta\Delta E_{cat}$, leads to the 4.0 kcal mol^{-1} total difference in energy between $TS_{1a}(R)$ and $TS_{1a}(S)$. Thus, the enantioselectivity of **1a** arises from the more favorable

[b] This decomposition is similar in spirit, but different in aim, than the distortion-interaction analyses utilized by Houk and co-workers (see D. H. Ess and K. N. Houk, J. Am. Chem. Soc. 2007, 129, 10646) and the activation-strain model of Bickelhaupt et al. (see W.-J. van Zeist, F. M. Bickelhaupt, Org. Biomol. Chem. 2010, 8, 3118).

binding of the (*S*)-substrate than the (*R*)-substrate by **1a** in the TS for the [3,3] sigmatropic rearrangement, as proposed by List *et al.*[19] However, this effect is tempered by the energetic cost of adopting the less favorable *syn* conformation of the substrate in $TS_{1a}(S)$.

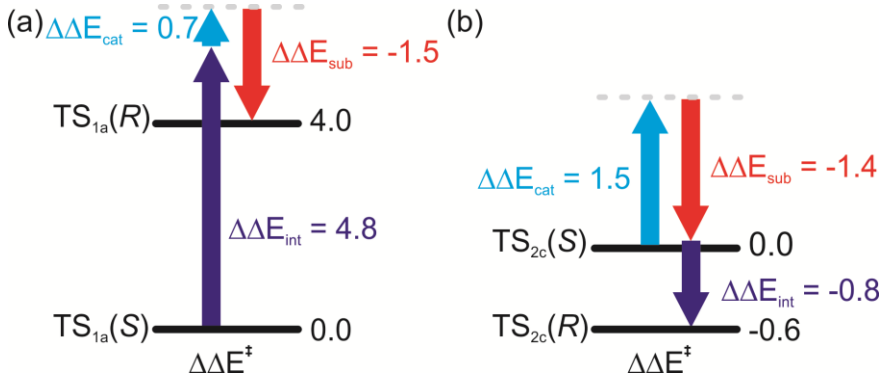

Figure II-2. (a) Decomposition of the energy difference between $TS_{1a}(R)$ and $TS_{1a}(S)$, $\Delta\Delta E^{\ddagger}$, into contributions from the difference in energy of the substrate ($\Delta\Delta E_{sub}$), the difference in energy of the catalyst ($\Delta\Delta E_{cat}$), and the difference in interaction energies of the substrate with the catalyst ($\Delta\Delta E_{int}$), in kcal mol^{-1}; (b) analogous decomposition of the energy difference between $TS_{2c}(R)$ and $TS_{2c}(S)$.

There are myriad non-covalent interactions present in $TS_{1a}(S)$ and $TS_{1a}(R)$ whose net effect leads to the 4.8 kcal mol^{-1} difference in interaction energies (see Figure II-1); unraveling the contributions of these interactions is impossible by simply examining the structures. To understand this difference, we approximately decomposed $\Delta\Delta E_{int}$ into contributions from non-covalent interactions between the substrate and the three components of the catalyst (see Figure II-1). Briefly, we partitioned the catalyst into three pieces by severing the C–C bonds connecting the two anthracenyl groups with the

phosphoric acid 'core', capping the open valences with hydrogen atoms.[26a] We then evaluated the interaction of the (*S*) and (*R*) transition state structures with each of these three catalyst components, providing an estimate of the H-bond interaction with the phosphoric acid functionality and the π-stacking and CH/π interactions with the two anthracenyl groups.

First, the qualitatively different hydrogen bonding interactions present in $TS_{1a}(R)$ and $TS_{1a}(S)$ contribute 2.6 kcal mol^{-1} to $\Delta\Delta E_{int}$, preferentially stabilizing $TS_{1a}(S)$ over $TS_{1a}(R)$. However, the enantioselectivity of **1a** does not arise from this difference alone; there are also substantial contributions from non-covalent interactions of the substrate with the anthracenyl groups. The most prominent interactions with the anthracenyl groups in these structures are π-stacking interactions.[33] For $TS_{1a}(S)$, these stacking interactions involve the benzyl *N*-protecting group, while in $TS_{1a}(R)$ the stacking interaction involves the phenyl ring of the phenyl hydrazine. These interactions contribute –2.4 kcal mol^{-1} to $\Delta\Delta E_{int}$. That is, π-stacking interactions of the substrate with the 9-anthracenyl group preferentially stabilize $TS_{1a}(R)$, significantly reducing the energy gap between $TS_{1a}(R)$ and $TS_{1a}(S)$!

The effects of π-stacking interactions are overcome by the difference in favorable CH/π interactions between the substrate and the other 9-anthracenyl group, which contributes 5.0 kcal mol^{-1} to $\Delta\Delta E_{int}$. In particular, in $TS_{1a}(S)$ there are aliphatic CH/π interactions of the cyclohexenyl ring with the 9-anthracenyl groups as well as aromatic CH/π interactions (edge-to-face interactions)[34] of the phenyl ring of the phenyl hydrazine with the anthracenyl group. These interactions outweigh the single CH/π contact in

$TS_{1a}(R)$; in $TS_{1a}(R)$, the substrate simply does not fit sufficiently tightly in the bonding pocket of **1a** to engage in favorable CH/π interactions with one anthracenyl group while maintaining π-stacking interactions with the other. This occurs in part because of the *anti* conformation of the substrate in $TS_{1a}(R)$. These energy differences are consistent with analyses based on the NCI index of Yang and co-workers,[35] which indicate more extensive dispersion-like interactions between the substrate and the 9-anthracenyl group in $TS_{1a}(S)$, compared to $TS_{1a}(R)$ (see SI Figure II-S1).

This can be contrasted with the TS structures for **2c**, for which the lowest-lying (*S*) transition state [$TS_{2c}(S)$] exhibits the same *gauche* conformation as $TS_{1a}(S)$, and the lowest-lying (*R*) transition state [$TS_{2c}(R)$] exhibits only a single NH-donated hydrogen bond. First, in the gas-phase $TS_{2c}(R)$ is 0.6 kcal mol^{-1} lower in energy than $TS_{2c}(S)$. This –0.6 kcal mol^{-1} energy difference is decomposed in Figure II-2b. In this case, $\Delta\Delta E_{int}$ is –0.8 kcal mol^{-1}; the H-bonding, π-stacking, and CH/π interactions between the substrate and catalyst are mostly balanced, slightly favoring the transition state leading to the (*R*) product. These are balanced by entropic and solvent effects, leading to the 0.1 kcal mol^{-1} difference in free energy between $TS_{2c}(R)$ and $TS_{2c}(S)$.

In conclusion, we have shown that the marked enantioselectivity exhibited by the first catalytic asymmetric Fischer indolization[19] arises from differences in hydrogen-bonding as well as favorable CH/π interactions in the rate-limiting [3,3]-sigmatropic rearrangement. The latter effect derives from the shape complementarity of the substrate and the binding pocket of **1a**, and echoes recent work from Jindal and Sunoj[25g] on a chiral phosphoric acid catalyzed asymmetric sulfoxidation reaction[36] as well as the

phosphoric acid catalyzed indole aza-Claisen reaction reported by Tantillo and Tambar.[28b] Vital to this shape complementarity is the *gauche* conformation of the benzyl group in the (*S*) transition state. The energetic cost of adopting this less-favorable conformation is more than compensated by the stronger non-covalent interactions that result. Furthermore, even though strong π-stacking interactions occur in both TS structures, their effect is to reduce the enantioselectivity of this reaction by preferentially stabilizing TS_{1a}(*R*). These data underscore the challenge of rationally designing catalysts that engage in the many coordinated non-covalent interactions required to achieve significant stabilization of a particular transition state,[5a] as well as the power of CH/π interactions as a means of achieving asymmetric induction.[25g, 28b] Whether similar effects are responsible for the enantioselectivity of equations 2.2 and 2.3 remains to be seen. Regardless, these results constitute a key first step toward a general understanding of asymmetric induction in chiral phosphoric acid catalyzed Fischer indolizations,[19, 23-24] which should aid the further development of organocatalysts for this transformation.

CHAPTER III

ELECTROSTATIC BASIS FOR ENANTIOSELECTIVE BRØNSTED-ACID CATALYZED ASYMMETRIC RING OPENINGS OF MESO-EPOXIDES[*]

3.1. Introduction

There have been concerted efforts in recent years to harness the power of favorable non-covalent interactions to develop more active and selective asymmetric organocatalysts.[25b, 25d, 31] This has been driven in part by Jacobsen and co-workers,[5a, 25c] who have argued that more effective organocatalysts should result from the stabilization of the preferred pathway through favorable non-covalent interactions rather than the destabilization of undesired pathways through steric interactions. Organocatalysts based on the former scheme should more closely mimic enzymes, which generally achieve stereoselectivity through a range of subtle electrostatic and other favorable non-covalent interactions.[37] Toste *et al*.[38] have embraced this idea within the context of chiral phosphate anion catalysis, demonstrating that highly stereoselective catalysts can be designed by exploiting favorable non-covalent interactions between the substrate and the 3,3′-aryl groups of the catalyst (*i.e.*, cation-π and π-stacking interactions, among others). This provided a powerful new strategy for the design of highly stereoselective catalysts,[38] particularly when paired with modern data analysis tools.[39] However, chiral phosphoric acid catalyzed reactions, which have exploded in popularity since their

[*]Adapted with permission from "Electrostatic Basis for Enantioselective Brønsted-Acid Catalyzed Asymmetric Ring Openings of meso-Epoxides" by T. J. Seguin and S. E. Wheeler, 2016. *ACS Catal.* **6**, 2681. Copyright 2016 American Chemical Society.

introduction a decade ago,[2, 18] are still often discussed in terms of traditional, steric-hindrance based modes of stereoinduction.[2]

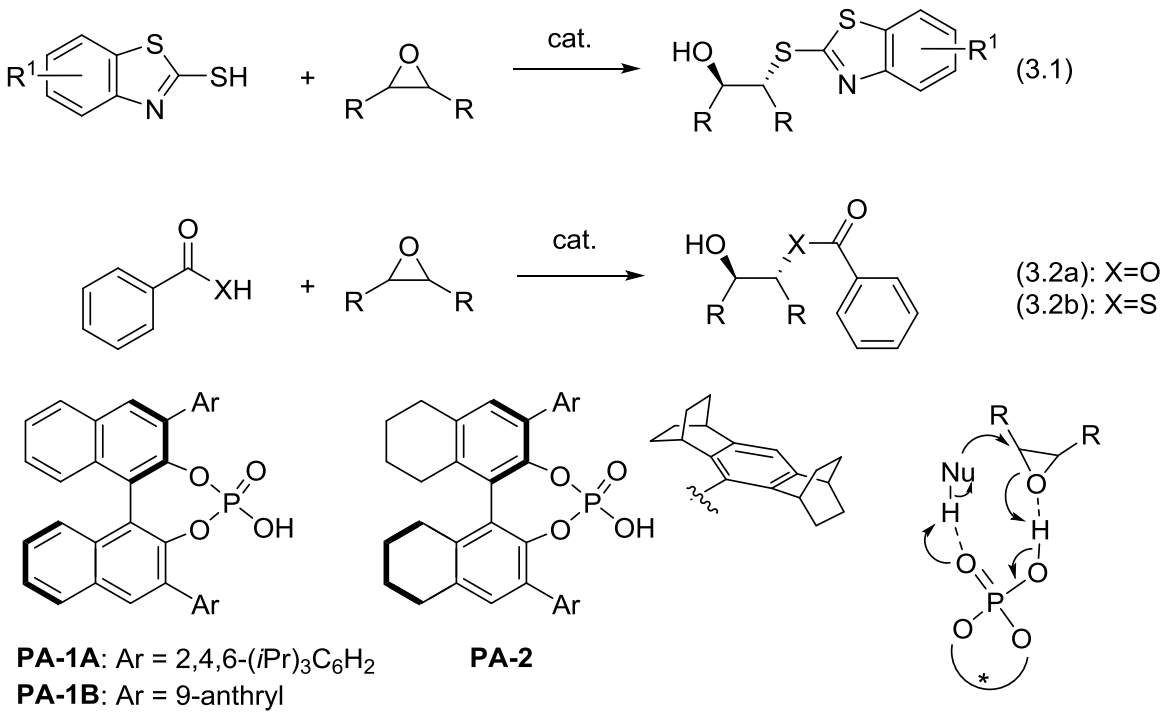

Scheme III-1. Brønsted-acid catalyzed asymmetric ring openings of meso-epoxides from Sun *et al*.[40] and List and co-workers.[41]

Table III-1. Predicted $\Delta\Delta G^{\ddagger}$ values (kcal mol^{-1}) and the corresponding *er*'s for equations 3.1 (where R^1 = OMe), 3.2a, and 3.2b catalyzed by **PA-1A**, **PA-1B**, and **PA-2**, along with available experimental data and reaction conditions. All reactions were run in toluene, except where noted.

Eq.	Cat.	Theor. $\Delta\Delta G^{\ddagger}$	Theor. *er*	Exptl. *er*	Exptl. $\Delta\Delta G^{\ddagger}$	Temp. (°C)
1	**PA-1A**	1.0	84.1:15.9	80.5:19.5[a,b]	0.8	25
1	**PA-1A**	0.9	90.3:9.7	92.5:7.5[a]	1.0	–78
1	**PA-1B**[c]	-0.3	36.4:63.6	54.5:45.5[a]	0.1	25
1	**PA-2**	0.4	66.9:33.1	-	-	25
2a	**PA-1A**	0.5	70.6:29.4	78.5:21.5[d]	0.8	25
2a	**PA-1B**	0.7	77.9:22.1	-	-	25
2a	**PA-2**	1.7	94.5:5.5	91.5:8.5[d]	1.4	25
2a	**PA-2**	1.6	97.0:3.0	96.5:3.5[d]	1.5	–40
2b	**PA-1A**	0.9	80.8:19.2	80.5:19.5[a,e]	0.8	25
2b	**PA-1B**	0.3	62.7:37.3	-	-	25
2b	**PA-2**	1.4	91.4:8.6	90.0:10.0[e]	1.3	25
2b	**PA-2**	1.3	94.6:5.4	95.0:5.0[e]	1.4	–40
2b	**PA-2**	1.3	96.5:3.5	98.0:2.0[e]	1.5	–78

[a] Ref. [40]. [b] dichloromethane used as solvent. [c] R^1 = H for the experimental and computational data for equation 3.1 catalyzed by **PA-1B**. [d] Ref. [41a]. [e] Ref. [41b].

Recently, chiral phosphoric acid catalysts have enabled the metal-free enantioselective synthesis of 1,2-difunctionalized compounds from the desymmetrization of *meso*-epoxides, a process previously limited to enzyme- and transition metal-based catalysts.[42] Such transformations provide routes to vicinal diols and β-hydroxythiols, which are key intermediates in the synthesis of myriad complex chiral molecules and pharmaceuticals.[43] The first chiral Brønsted acid-catalyzed, non-enzymatic nucleophilic *meso*-epoxide ring opening was demonstrated by Sun and co-workers in 2013.[40] Several phosphoric acid catalysts were surveyed for the opening of

cyclic and acyclic *meso*-epoxides with mercaptobenzothiazole nucleophiles (Scheme III-1, equation 3.1). The BINOL-derived catalyst TRIP (**PA-1A**) paired with 5-methoxymercaptobenzothiazole as the nucleophile provided the best performance, yielding *er*'s exceeding 85:15 for a broad range of epoxides. Other, related catalysts featuring less bulky aryl groups at the 3- and 3′-positions (*e.g.* **PA-1B**) proved much less enantioselective (see Table III-1). Sun *et al*. showed[40] that the aryl sulfides that result from equation 3.1 can be cleaved to yield the corresponding β-hydroxythiols with no loss of enantiomeric excess. The enantioselectivity of this reaction was attributed to greater steric repulsion between the epoxide and the 3,3′-aryl groups of the catalyst in the disfavored (*S,S*) transition state (see Figure III-1a). That is, in accord with conventional views of phosphoric acid catalyzed transformations,[44] Sun's model[40] rests on the assumption that the two competing transition states involve different orientations of the substrates within the chiral binding pocket of the catalyst (see Figure III-1a) and the preferred TS is the one that minimizes steric repulsions.

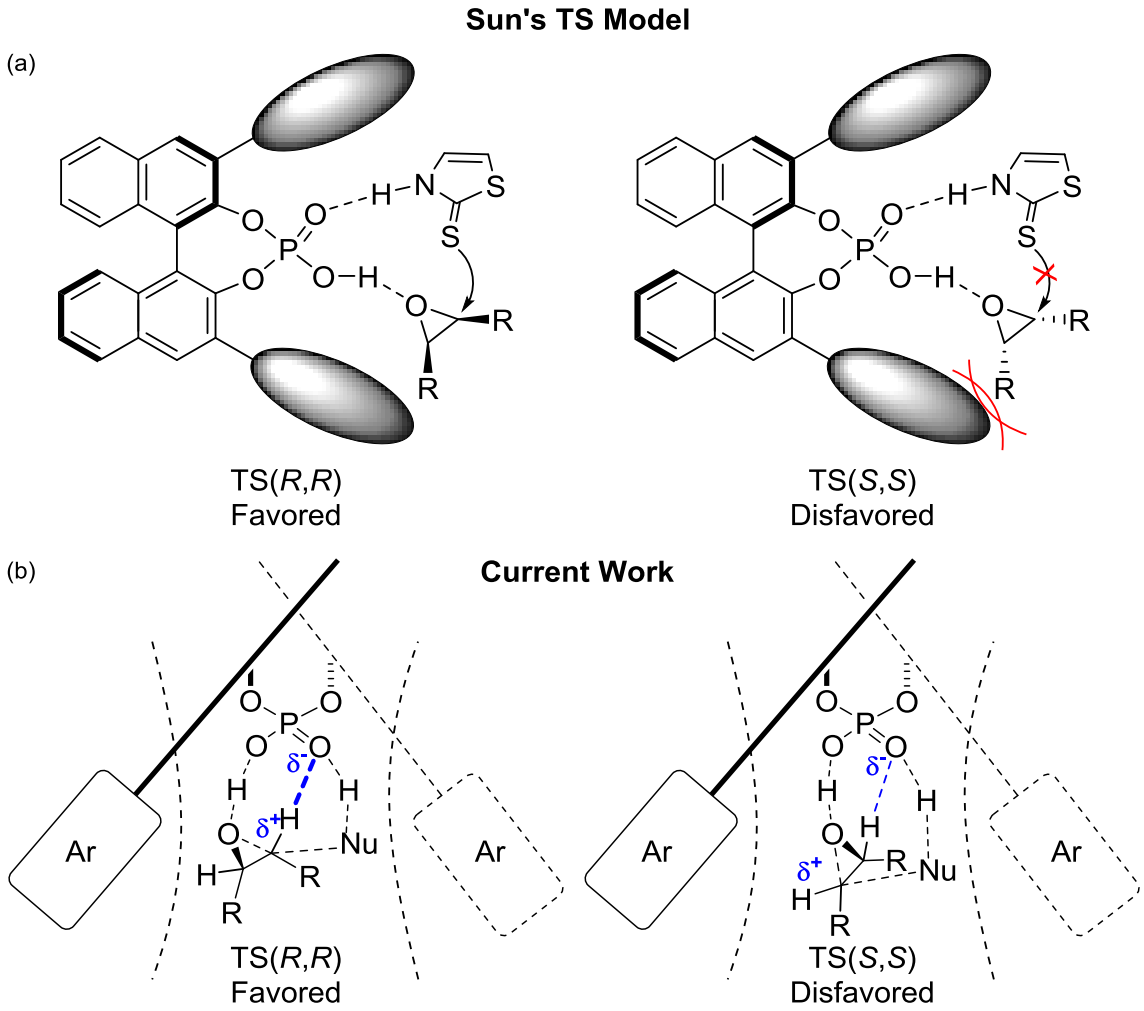

Figure III-1. (a) TS model of Sun and co-workers[40] to explain the enantioselectivity of equation 3.1 with catalyst **PA-1A**, in which steric interactions with the 3,3′-aryl groups destabilize TS(*S*,*S*). (b) Our model of enantioselectivity in chiral phosphoric acid catalyzed asymmetric *meso*-epoxide ring openings, in which electrostatic interactions of the electrophile with the phosphoryl oxygen of the catalyst drives the enantioselectivity. The 3,3′-aryl groups (Ar) serve primarily to create a restrictive binding groove that orients the substrates within the electrostatic environment of the catalyst.

Shortly thereafter, List *et al*.[41a] used **PA-2** in asymmetric ring openings of *meso*-epoxides with carboxylic acids to give monoprotected *trans*-1,2-diols (equation 3.2a). **PA-2**, which is built on an (H_8)-BINOL scaffold and incorporates a novel sterically demanding polycyclic ring system at the 3- and 3′-positions, was designed to improve enantioselectivity over **PA-1A** by providing a more tightly confined chiral reactive site. Subsequently, List and co-workers[41b] provided a strategy analogous to that of Sun *et al*.[40] for the asymmetric synthesis of β-hydroxythiols through chiral phosphoric acid catalyzed desymmetrizations of *meso*-epoxides based on an organocascade sequence (Scheme III-2). In the initial step (Scheme III-1, equation 3.2b), **PA-2** gave highly enantioenriched β-hydroxythioester intermediates from the addition of thiocarboxylic acids to various *meso*-epoxides. Free thiols were then accessed by a catalytic intramolecular acyl-transfer reaction at an elevated temperature (40 °C), while preserving the enantiomeric excess. This transformation worked for a range of epoxides, with the exception of five-membered cyclic oxides. The lack of reactivity in the latter case was attributed to the high energy bicyclic intermediate that would occur along the reaction pathway. This one-pot organocatalytic cascade represented an improvement over Sun's route to β-hydroxythiols[40] by requiring fewer steps and milder reaction conditions, yet with similar enantioselectivities.[41b]

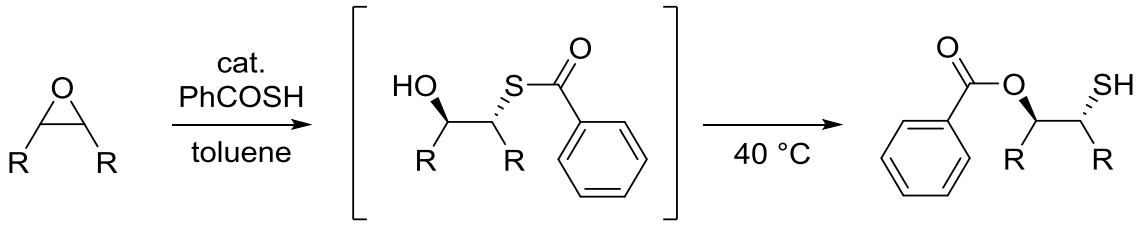

Scheme III-2. Organocatalytic cascade sequence of List et al. for the asymmetric synthesis of β-hydroxythiols.[41b]

The mode of stereoinduction proposed by Sun and co-workers[40] for equation 3.1 (Figure III-1a) is emblematic of the prevailing design strategy for chiral phosphoric acid catalysts.[29, 44a] However, favorable non-covalent interactions of the substrate with the 3,3′-aryl groups have been proposed in a number of chiral phosphoric acid catalyzed reactions,[25g, 45] and could be operative in equations 3.1 and 3.2. For instance, we recently showed[45c] that the enantioselectivity of List's asymmetric catalytic Fischer indole reaction[19] depends on favorable CH/π interactions between the substrate and the flanking aryl groups. There has also been increased appreciation in recent years of the role of non-classical CH···O interactions in asymmetric reactions,[25e] and CH-donated hydrogen bonds to the phosphoryl oxygen (P=O) of the catalyst have been invoked in a number of phosphoric acid catalyzed transformations.[25g, 28b, 29e, 45a, 46] Indeed, Ajitha and Huang[46j] very recently published a computational study of equation 3.2b catalyzed by **PA-2** focused on the different possible tautomeric states of the nucleophile. They attributed the enantioselectivity of this transformation to a combination of steric factors and CH···O

interactions, noting that the CH···O distance was much shorter in the preferred transition state, TS(*R*,*R*), compared to that in the competing transition state, TS(*S*,*S*).

However, there is another feature of chiral phosphoric acids that provides a potentially complementary means of achieving stereoinduction—the polarized electrostatic environment of the phosphoric acid functionality. More precisely, the phosphoryl oxygen of these catalysts provides a substantial partial negative charge that can not only accept a hydrogen bond from the nucleophile and from CH groups on the electrophile, but can also potentially stabilize transient positive charges in the preferred transition state. Herein, we apply modern density functional theory (DFT) methods to equations 3.1, 3.2a, and 3.2b catalyzed by **PA-1A**, **PA-1B**, and **PA-2** in order to develop a comprehensive model of the enantioselectivity of enantioselective Brønsted-acid catalyzed ring openings of *meso*-epoxides. We show that the enantioselectivity of these reactions arises from the enzyme-like electrostatic stabilization of the reacting electrophile by the phosphoryl oxygen of the catalyst, suggesting a complementary means of achieving stereoinduction in chiral phosphoric acid catalyzed reactions.

3.2. Theoretical Methods

Geometries, vibrational frequencies, and thermal free energy corrections were computed at the B97-D/def2-TZVP level of theory,[8, 47] accounting for solvent effects with PCM[48] (the solvent was toluene, except where noted in Table III-1). Transition state structures were verified by the presence of a single imaginary vibrational frequency. The presented theoretical free energy differences ($\Delta\Delta G^{\ddagger}$) correspond to the difference in free

energy between the lowest-lying (*S*,*S*) and (*R*,*R*) transition state structures for each reaction/catalyst combination based on an extensive search of possible conformations of the catalyst and substrates (see SI for more detail). It is assumed that these reactions are under Curtin-Hammett control, and that the enantioselectivity is dictated by $\Delta\Delta G^{\ddagger}$ for the stereocontrolling step (*vide infra*). Thermal free energy corrections were based on the quasi-rigid rotor/harmonic oscillator (quasi-RRHO) approximation of Grimme[49] (temperatures are specified in Table III-1). In the quasi-RRHO approach, the entropic contributions of low-frequency vibrational modes are interpolated between the values of a harmonic oscillator and an effective rigid rotor.[c] The final presented free energies were computed at the PCM-B97-D3/def2-TZVP//PCM-B97-D/def2-TZVP level of theory.[8, 11a, 47] This level of theory, which accounts for the sundry dispersion-driven non-covalent interactions operative in these transition states, predicts *ee*'s that are in excellent agreement with experimental enantioselectivities.[d] The free energy profile for the complete mechanism of the organocatalytic cascade of List and co-workers (Scheme III-2) was computed at the PCM-ωB97X-D/6-311+G(d,p)//PCM-ωB97X-D/6-31G(d) level of theory.[9] Atomic charges were computed using natural population analysis.[50] Throughout, cyclohexene oxide was used as a representative epoxide, except where

[c] These quasi-RRHO free energy differences are in much better agreement with the experimental er values than those derived from the standard RRHO approximation.

[d] M06-2X/6-311+G(d,p)//M06-2X/6-31G(d) provides er predictions that are nearly as reliable as those presented for most reaction/catalyst combinations. However, for equation 3.2b catalyzed by PA-1A, M06-2X predicts the opposite sense of stereoinduction compared to experiment. wB97X-D/6-311+G(d,p)//wB97X-D/6-31G(d) predicted relative free energy barriers provide more modest agreement with experiment. See Appendix Table B-1.

noted. All computations were performed using Gaussian 09,[51] and the B97-D computations employed density fitting techniques.

3.3. Results and Discussion

The stereocontrolling step in equations 3.1, 3.2a, and 3.2b catalyzed by **PA-1A**, **PA-1B**, and **PA-2** is the concerted, S_N2-like step depicted in Scheme III-1.[46j] The lowest-lying TS structures leading to the (*R*,*R*) and (*S*,*S*) ring-opened products for equation 3.1 catalyzed by **PA-1A** are shown in Figure III-2. The lowest-lying transition state structures for the other reaction/catalyst combinations are structurally very similar, suggesting a common mode of asymmetric induction in these reactions. In these transition state structures, the phosphoric acid protonates the epoxide as it undergoes nucleophilic attack. In some cases, this is accompanied by the deprotonation of the nucleophile by the phosphoric acid, whereas in other cases the deprotonation of the nucleophile occurs in a subsequent, low-barrier step. For equation 3.1, we find that the lowest-lying TS structures involve the thione tautomer of the mercaptobenzothiazole nucleophile, which is bound to the catalyst by an NH···O hydrogen bonding interaction. Similarly, the thiobenzoic acid in equation 3-2b also appears as the thione tautomer in the corresponding transition states, as previously shown by Ajitha and Huang,[46j] which hydrogen bonds to the catalyst in the same manner through its hydroxyl group.

Computed relative free energy barriers and *er* values are shown in Table III-1, and are in remarkable agreement with experiment. Indeed, for many of the reaction/catalyst combinations, the predicted $\Delta\Delta G^{\ddagger}$ values are within 0.1 kcal mol^{-1} of

the experimentally-derived $\Delta\Delta G^{\ddagger}$, and all are within 0.4 kcal mol^{-1}. Most importantly, the trends in enantioselectivities are very accurately captured, including the lack of enantioselectivity in the case of equation 3.1 catalyzed by **PA-1B**. Predictions for three reaction/catalyst combinations for which experimental enantioselectivities are unavailable are also provided. In particular, we predict that **PA-2** will provide low *er*'s for equation 3.1, while **PA-1B** will similarly give low *er* values for equations 3.2a and 3.2b.

For each reaction/catalyst combination, the lowest-lying (*R*,*R*) and (*S*,*S*) transition state structures are strikingly similar to each other, differing only slightly in the orientation of the epoxide (see Figure III-2); the orientation of the nucleophile is almost identical in TS(*S*,*S*) and TS(*R*,*R*), poised above the two epoxide carbons. The enantioselectivity of these reactions stems from the propensity for nucleophilic attack of one carbon over the other. In Sun's TS model,[40] steric interactions between the epoxide and 3,3′-aryl groups lead to preferential formation of the (*R*,*R*) adduct (see Figure III-1a). However, the structural similarity of TS(*R*,*R*) and TS(*S*,*S*) precludes any significant role of steric interactions in the enantioselectivity of these reactions. Indeed, initial examination of the structures of TS(*R*,*R*) and TS(*S*,*S*) reveal no obvious structural source of stereoinduction.

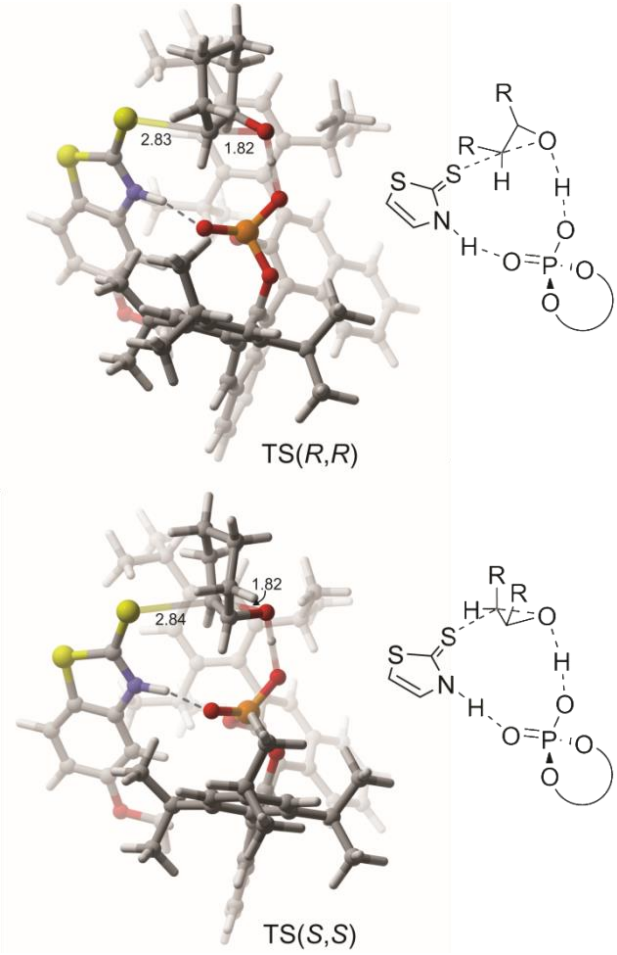

Figure III-2. Optimized structures of the stereocontrolling transition state structures for equation 3.1 catalyzed by **PA-1A**. TS structures for the other reaction/catalyst combinations are similar (see Appendix B). Distances of the forming S–C and breaking C–O bonds are provided in Angstroms. For clarity, in the line drawings the structure of the nucleophile is truncated and the catalyst backbone depicted as a simple curve.

To identify the origin of the free energy differences between TS(*S*,*S*) and TS(*R*,*R*) in equations 3.1, 3.2a, and 3.2b catalyzed by **PA-1A**, **PA-1B**, and **PA-2**, we first computed gas-phase energy differences ($\Delta\Delta E^{\ddagger}$) at the solution-phase TS geometries (see Table III-2). Apart from equation 3.1 catalyzed by **PA-2**, the gas-phase energy differences are comparable to the solution-phase free energy differences, indicating that

solvent and entropy effects have little net impact on the enantioselectivity of these reactions. In the case of equation 3.1 catalyzed by **PA-2**, solvent and entropic effects severely hinder the enantioselectivity by reducing the gas-phase energy difference of 1.7 kcal mol^{-1} to only 0.4 kcal mol^{-1}. For reaction catalyzed by **PA-1B**, which exhibits essentially no entantioselectivity experimentally, the effect of entropy and solvent effects is to change the +0.3 kcal mol^{-1} gas-phase energy difference between TS(*R*,*R*) over TS(*S*,*S*) to –0.3 kcal mol^{-1}.

For each of these transformations, we decomposed the gas-phase energy difference, $\Delta\Delta E^{\ddagger}$, into three contributions:[45c] the difference in energy required to distort the substrates into the geometries of the two low-lying TS structures ($\Delta\Delta E_{sub}$); the difference in energy required to distort the catalyst into the geometries in the two TS structures, ($\Delta\Delta E_{cat}$); and the difference in interaction energies between the distorted substrates and the catalyst, $\Delta\Delta E_{int}$. These data are collected in Table III-2. For all reaction/catalyst combinations except 2a/**PA-2**, the net effect of distortions is to reduce the energy gap between TS(*S*,*S*) and TS(*R*,*R*). Apparently, for equation 3.2a with **PA-2**, the bulk of the enantioselectivity arises from the greater energy required to distort the catalyst into the geometry of TS(*S*,*S*), compared to TS(*R*,*R*). For the other systems, the enantioselectivity is due to differences in interaction energies between the substrate and catalyst in the competing transition state structures ($\Delta\Delta E_{int}$); for these reaction/catalyst combinations, the interaction between the substrate and catalyst is more favorable in TS(*R*,*R*) than it is in TS(*S*,*S*).

Table III-2. Predicted gas-phase energy barrier height differences ($\Delta\Delta E^{\ddagger}$, in kcal mol^{-1}) for equations 3.1, 3.2a, and 3.2b catalyzed by **PA-1A**, **PA-1B**, and **PA-2**, the decomposition of $\Delta\Delta E^{\ddagger}$ into $\Delta\Delta E_{sub}$, $\Delta\Delta E_{cat}$, and $\Delta\Delta E_{int}$ and the differences in interaction energies for truncated model systems M1 and M2 (see Figure III-3).

Eq.	Cat.	$\Delta\Delta E^{\ddagger}$	$\Delta\Delta E_{sub}$	$\Delta\Delta E_{cat}$	$\Delta\Delta E_{int}$	$\Delta\Delta E_{int}$(M1)	$\Delta\Delta E_{int}$(M2)
1	**PA-1A**	0.9	-0.6	0.5	1.0	1.0	1.0
1	**PA-1B**	0.3	-0.4	0.1	0.6	0.8	0.8
1	**PA-2**	1.7	-1.0	1.2	1.5	2.3	2.0
2a	**PA-1A**	1.4	0.0	-0.8	2.2	2.7	2.4
2a	**PA-1B**	0.8	-0.3	0.0	1.1	1.5	1.3
2a	**PA-2**	1.4	-0.1	1.1	0.5	0.6	0.6
2b	**PA-1A**	0.5	-0.1	-0.5	1.1	1.2	1.1
2b	**PA-1B**	0.8	-1.8	0.2	2.3	3.2	0.9
2b	**PA-2**	1.1	0.0	-0.1	1.2	1.1	-0.1

To pinpoint the origin of these $\Delta\Delta E_{int}$ values, we considered a series of truncated model systems in which successive fragments of the catalyst are excised (see Figure III-3). First, gas-phase energy differences between TS(*S*,*S*) and TS(*R*,*R*) were computed after replacing the 3,3′-aryl groups of the catalyst with hydrogens (model M1, see Table III-2).[e] Remarkably, removing the flanking aryl groups from these TS structures leads to either little change or an increase in the interaction energy of TS(*S*,*S*) relative to TS(*R*,*R*). Apparently, in these structures, non-covalent interactions of the substrates with the 3,3′-aryl groups preferentially stabilize TS(*S*,*S*) and reduce the enantioselectivity of these reactions!

Next, the BINAP backbone of the catalysts was replaced with hydrogen atoms, and the gas-phase interaction energy differences recomputed (model M2). Once again, the energy difference between TS(*S*,*S*) and TS(*R*,*R*) remained largely unchanged, and in

[e] In both M1 and M2, the positions of the added hydrogens were optimized, while all other atoms remained fixed.

all but two cases the interaction energy difference in model M2 matches that of the intact TS structures. Consequently, for most of the nine examples of asymmetric ring openings of *meso*-epoxides, the enantioselectivity stems from interactions of the substrate with the phosphoric acid functionality of the catalyst. The catalyst backbone and 3,3'-aryl groups play only secondary roles, serving primarily to control the orientation of the substrates relative to the phosphoric acid functionality.

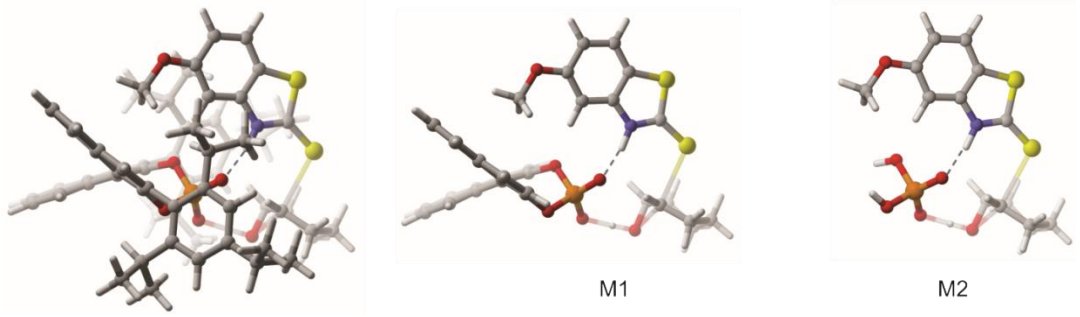

Figure III-3. Truncated model systems (M1 and M2) used to isolate the effects of the 3,3'-aryl groups and the catalyst backbone on energy differences between TS(*R*,*R*) and TS(*S*,*S*), using TS(*R*,*R*) for equation 3.1 catalyzed by PA-1A as an example. In M1, the 3,3′-aryl groups have been replaced with hydrogens, while in M2 the BINAP backbone is removed.

As noted recently by Ajitha and Huang,[46j] both TS(*R*,*R*) and TS(*S*,*S*) for equation 3.2b catalyzed by **PA-2** feature a non-classical C-H···O hydrogen bonding interaction[25e] between the epoxide and the phosphoryl oxygen of the catalyst, which is shorter in the lower-lying TS(*R*,*R*). In agreement with their results, we found that all nine reaction/catalyst combinations examined, the CH···O distance is substantially shorter in the favored TS(*R*,*R*) than in TS(*S*,*S*). Ajitha and Huang[46j] postulated that this was due to

the existence of favorable electrostatic interactions within the chiral electrostatic environment of the catalyst. To understand the role of the CH···O distances, we considered H_3PO_4 as a model chiral catalyst (see Appendix B Figure B-1). The free energy difference between TS(*S*,*S*) and TS(*R*,*R*) for this model is 0.6 kcal mol^{-1}, and the CH···O distance is 0.13 Å larger in TS(*S*,*S*) than in TS(*R*,*R*). This is qualitatively similar to the corresponding values for the real phosphoric acid catalysts. If the CH···O distance in TS(*S*,*S*) is constrained to match that in TS(*R*,*R*), this free energy difference increases slightly to 0.8 kcal mol^{-1}. In other words, the difference in CH···O distances is not the cause of the energy difference between TS(*R*,*R*) and TS(*S*,*S*) in these reactions; instead, the difference in CH···O distances is a consequence of other non-covalent interactions between the substrate and catalyst.

As postulated by Ajitha and Huang,[46j] these data are consistent with TS(*R*,*R*) being preferentially stabilized by electrostatic interactions within the chiral environment of the phosphoric acid (see Figure III-4). In particular, in the transition states there is a build-up of partial positive charge on the CH group undergoing nucleophilic attack (see Figure III-4b). In TS(*R*,*R*), this group bearing partial positive charge is ideally positioned to interact with the substantial negative charge of the phosphoryl oxygen of the catalyst (see Figure III-4b). In the disfavored (*S*,*S*)-transition state, the nucleophilic attack is occurring on the carbon located farther from the phosphoryl oxygen, preventing any significant electrostatic stabilization. This selective electrostatic stabilization of the fleeting positive charge in one transition state is the cause of the difference in CH···O distances, and appears to be a novel mode of stereoinduction in Brønsted-acid catalyzed

reactions. However, an analogous stabilizing electrostatic interaction was recently unveiled by Cheong, *et al*.,[52] who showed that stabilizing CH···O interactions underlie the stereoselectivity of an NHC-catalyzed dynamic kinetic resolution of α-substituted-β-ketoesters. In that case, the CH group was located on the catalyst, and stabilized a fleeting negative charge on the reacting substrate. This electrostatic mode of stereoinduction is also reminiscent of proposed formyl CH···O interactions in the oxazaborolidinium catalysts of Corey and co-workers[53] and the formyl CH···Cl interactions discussed in the context of bidentate Lewis-base catalyzed alkylation reactions by Lu and co-workers.[26a, 54] However, whereas the latter two cases relied on permanent partial charges on formyl CH groups, the models in this work and in that of Cheong *et al*. hinge on the fleeting charges in the transition state.

Despite minor differences among the individual contributions to the free energy barrier differences for the various reaction/catalyst combinations, these data support a relatively general stereochemical model of chiral phosphoric acid catalyzed ring openings of *meso*-epoxides (see Figure III-1b). The sterically bulky 3,3′-aryl groups of these catalysts serve primarily to create a narrow binding groove that restricts the possible binding orientations of the substrate in both TS(*R*,*R*) and TS(*S*,*S*). These restricted binding poses place the two enantiotopic carbons of the epoxide in considerably different electrostatic environments. Nucleophilic attack of the carbon nearest the phosphoric acid functionality [leading to the (*R*,*R*)-ring opened product] results in favorable electrostatic interactions with the phosphoryl oxygen of the catalyst

during the TS, whereas attack of the distal carbon [leading to the (*S*,*S*)-product] does not lead to such stabilization.

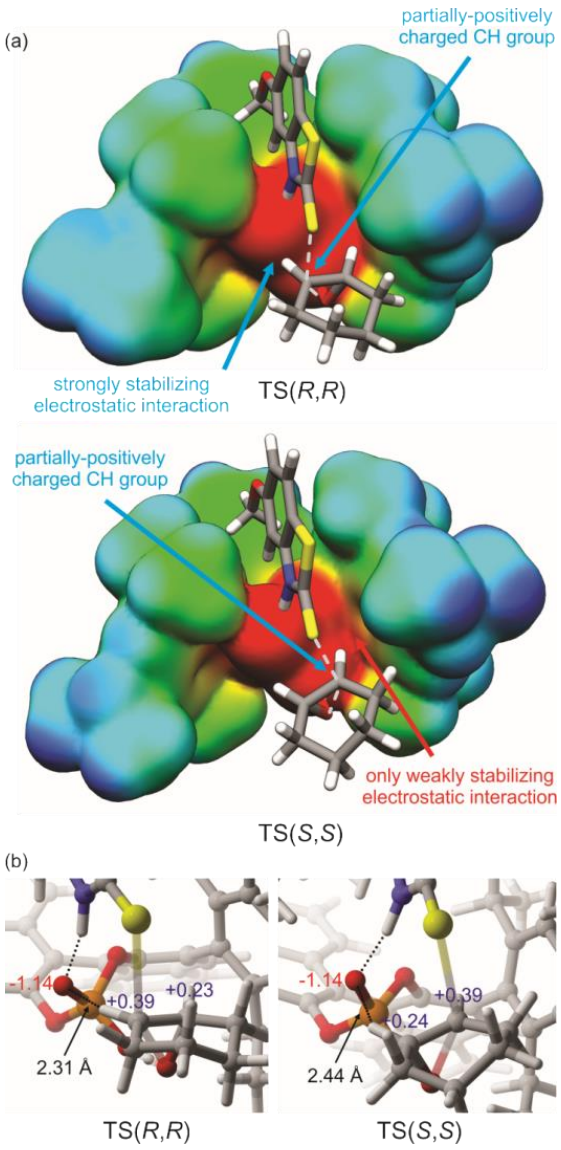

Figure III-4. (a) Electrostatic potentials (red: –100 kcal mol^{-1}; blue: -20 kcal mol^{-1}) mapped onto the electron density isosurface (ρ = 0.002 *e*/*au*^{3}) of the catalyst in the lowest-lying (*R*,*R*) and (*S*,*S*) transition state structures for equation 3.1 catalyzed by **PA-1A**. (b) Natural atomic charges on the CH groups of the epoxide and the phosphoryl oxygen of the catalyst in TS(*R*,*R*) and TS(*S*,*S*) for equation 3.1 catalyzed by **PA-1A**, as well as the distance (in Angstroms) between the H and O in the non-classical CH···O hydrogen bonds.

This exploitation of subtle electrostatic interactions within a confined and electrostatically-polarized binding site is characteristic of enzyme catalysts, and these chiral phosphoric acid catalysts represent a significant step toward the enzyme-like organocatalysts envisioned by Knowles and Jacobsen.[5a] In this regard, we note that epoxide hydrolases have been developed that exhibit high degrees of enantioselectivity in the ring-opening of *meso*-epoxides.[55] The stereoselectivities of these biocatalytic reactions, which served as inspiration for List's design of equation 3.2a, have previously been explained in terms of steric interactions.[55d, 56] However, based on the present results, as well as those of Ajitha and Huang,[46j] it might be prudent to also consider the impact of stabilizing electrostatic interactions with the chiral electrostatic environment of the enzyme on the enantioselectivity of these biocatalyzed epoxide ring-opening reactions.

From a broader perspective, the electrostatic interactions discussed above represent an underappreciated means of achieving stereoinduction in chiral phosphoric acid catalyzed reactions (see Figure III-5c). That is, in addition to the destabilization of the disfavored TS through steric interactions (Figure III-5a) and the stabilization of the favored TS through non-covalent interactions with the 3,3′-aryl groups (Figure III-5b), the preferred TS can be stabilized through electrostatic interactions with the phosphoryl oxygen of the catalyst (Figure III-5c).

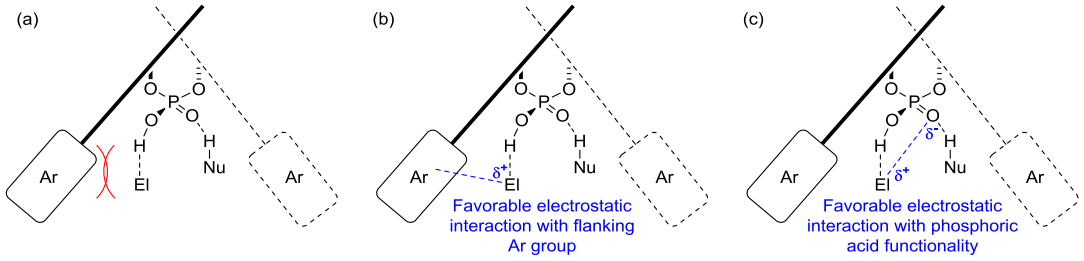

Figure III-5. Different means of achieving stereoinduction in chiral phosphoric acid catalysts: (a) steric interactions block access to the disfavored TS; (b) favorable non-covalent interactions of the substrate with the 3,3′-aryl groups of the catalyst stabilize the favored TS;[38] (c) preferential electrostatic stabilization of the favored TS through interactions with the phosphoric acid functionality.

Finally, we briefly address a distinguishing feature of Lists's catalytic synthesis of β-hydroxythiols, which is the intramolecular transesterification to form the free thiol (Scheme III-2).[41b] This latter step in the organocascade sequence requires an elevated temperature of 40 °C, and was shown not to proceed for five-membered cyclic epoxides. A computed reaction free energy profile with cyclohexene oxide and a model catalyst is presented in Figure III-6.[f] The analogous pathway for cyclopentene oxide is also shown. The thermodynamically most stable configuration of substrates is the heterodimer (**1a**), comprising the catalyst hydrogen bonded with the nucleophile, and epoxide at infinite separation. Complexation of the epoxide with this dimer gives complex **2**, in which both the epoxide and the thione tautomer of thiobenzoic acid are hydrogen-bonded to the catalyst. The free energy barrier for the initial thiocarboxylysis of cyclohexene oxide is 16.0 kcal mol^{-1} (**TS1** vs **1a** + **1b**). The corresponding free energy barrier for

[f] These computations employ a model catalyst for PA-1A, in which the three isopropyl substituents of the 3,3′-aryl groups are replaced with methyl groups and the binaphthyl backbone is replaced with biphenyl. These changes are not expected to impact the overal reaction profile.

cyclopentene oxide (**1c**) is only modestly higher at 18.1 kcal mol^{-1}. This transition state leads directly to complex **3**, in which the β-hydroxythioester is hydrogen-bonded to the catalyst. The remaining pathway is a stepwise process involving intramolecular C-O bond formation followed by C–S bond cleavage to form the free thiol. In each of the steps, protons are exchanged with the catalyst. Prior to traversing **TS2**, complex **3** must undergo conformational changes to bring the reactive functionalities closer together, most importantly by rotation of the S–C–C–O dihedral angle (see Figure III-6) during a cyclohexane ring flip. Following **TS2** is formation of the five-membered heterocycle **5**. Prior to **TS3**, in which the C–S bond is cleaved and the ring opened to form the free thiol, the site of hydrogen-bonding interaction from the catalyst hydroxyl group must switch from the oxygen (**5**) to the sulfur of the heterocycle (**6**). Following formation of the thiol (**7**), another ring flip yields the thermodynamically stable product **8**.

For cyclohexene oxide (**1b**), the activation free energy for the trans-esterification step (from **3** to **TS2**) is 19.0 kcal mol^{-1}. This is 3.0 kcal mol^{-1} higher than the barrier for the initial step in the cascade (**1a** + **1b** to **TS1**), which explains the need for elevated temperatures for the latter step. In the analogous pathway for cyclopentene oxide (**1c**), the activation free energy for the transesterification is 25.4 kcal mol^{-1}. This more substantial barrier prohibits formation of the thiol and completion of the organocascade sequence for this particular substrate. The larger reaction barrier for cyclpentene oxide arises primarily due to the high free energy of **TS2**, which is consistent with the model presented by List and co-workers[41b] since it is during this transition state that the bicyclic intermediate (**5**) is first formed. The energetic cost of forming this strained species is

evinced by the 9.2 kcal mol^{-1} difference in relative free energy between intermediate **5** for the cyclopentene oxide reaction and the cyclohexene oxide reaction.

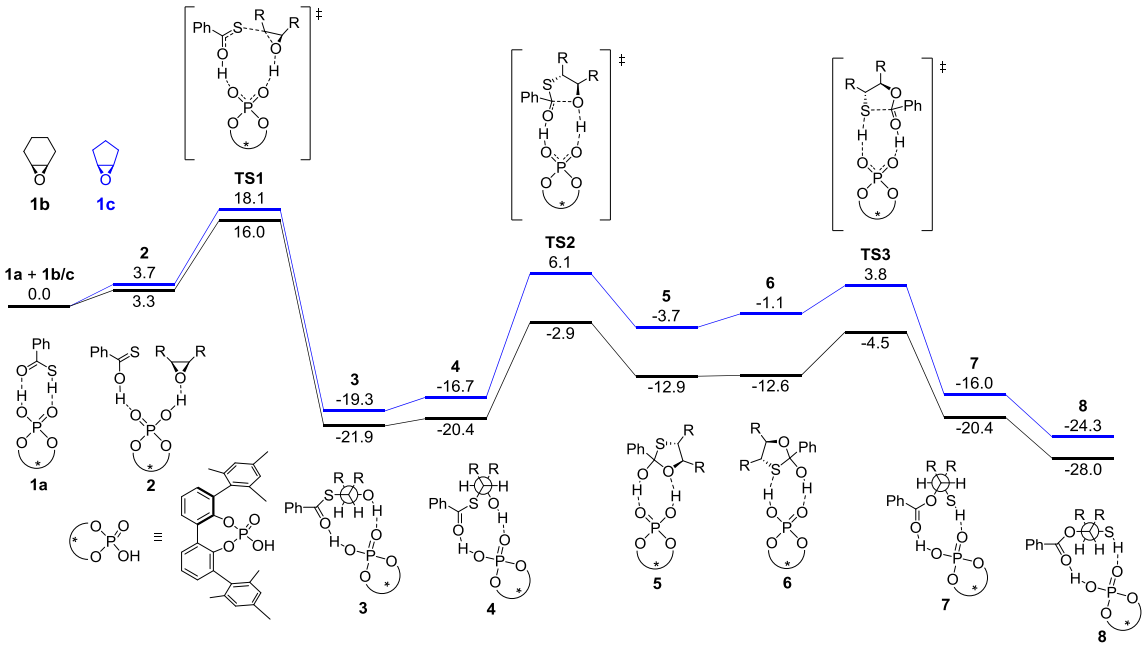

Figure III-6. Reaction free energy profile (kcal mol^{-1}) for the organocatalytic cascade shown in Scheme III-2 using the model catalyst pictured, relative to the separated nucleophile/catalyst complex (**1a**) and epoxide (**1b** or **1c**). The black lines depict the free energy for cyclohexene oxide (**1b**), whereas the blue lines are for cyclopentene oxide (**1c**).

3.4. Concluding Remarks

The design of chiral phosphoric acid catalysts has traditionally relied on conventional stereochemical models, in which the preferred transition state is the one that minimizes steric interactions with the chiral binding pocket of the catalyst. More recently, there has been growing appreciation of the role of non-covalent interactions in the stabilization of the preferred pathway, moving toward the vision of Jacobsen *et al.*[5a, 25c] that organocatalysts should function more like enzymes in this regard. Chief among the stereocontrolling elements discussed in the context of chiral phosphoric acid catalyzed reactions are non-covalent interactions of the substrate with the 3,3′-aryl substituents of the catalyst and non-classical CH···O interactions between the substrate and the phosphoric acid.

Herein, we showed that the enantioselectivity of each of the three recently published[40-41] chiral phosphoric acid catalyzed asymmetric ring-openings of *meso*-epoxides (Scheme III-1) arise in large part from favorable electrostatic interactions of one transition state with the highly polarized, chiral electrostatic environment of the phosphoric acid functionality itself. The 3,3′-aryl groups of the catalyst, although absolutely necessary for enantioselectivity, serve primarily to create a narrow, enzyme-like binding groove that controls the orientation of the nucleophile and electrophile within the chiral electrostatic environment of the phosphoric acid. This restricted orientation, along with the highly-charged atoms of the phosphoric acid, lead to the preferential electrostatic stabilization of only the favored TS structure. Ultimately, this electrostatic mode of stereoinduction provides a complementary means of differentiating

between sterically similar transition states and represents a step toward the design of organocatalysts that are truly enzyme-like in the origin of their stereoselectivity.

We also briefly examined the organocatalytic cascade leading of List and co-workers[41b] (scheme 2). The larger activation energy required for the transesterification explains the need to for increased reaction temperatures to facilitate the latter steps in this cascade sequence, and the large predicted reaction barrier in the case of cyclopentene oxide explains the incompatibility of this organocascade with five-membered cyclic epoxides.

CHAPTER IV

COMPETING NON-COVALENT INTERACTIONS CONTROL THE STEREOSELECTIVITY OF CHIRAL PHOSPHORIC ACID-CATALYZED RING OPENINGS OF 3-SUBSTITUTED OXETANES*

4.1. Introduction

Attractive non-covalent interactions can play pivotal roles in asymmetric organocatalytic reactions, sometimes overshadowing the impact of simple steric effects.[5a, 25b, 38, 39b, 57] The overall stereoselectivity of such reactions often hinges on the cumulative effect of numerous, competing non-covalent interactions, which can complicate the identification of a single factor that is responsible for stereoinduction across many instances of a given reaction. In 2013, Sun *et al*. introduced[58] the first intermolecular organocatalytic desymmetriziations of 3-substituted oxetanes (Scheme IV-1), which provide access to quaternary stereocenters that are key chiral building blocks of many complex chiral molecules.[59] In the presence of chiral phosphoric acids,[18a, 18b, 60] oxetanes bearing one or two substituents at the 3-position undergo ring-opening upon nucleophilic attack by mercaptobenzothiazoles to give the corresponding alcohols with high efficiency and enantioselectivity (see Table IV-1). More recent work from Sun *et al*.[61] has expanded this chemistry to other nucleophiles, providing access to even broader functionality through the nucleophilic opening of oxetanes.

---

* Adapted with permission from "Competing Non-Covalent Interactions Control the Stereoselectivity of Chiral Phosphoric Acid-Catalyzed Ring Openings of 3-Substituted Oxetanes" by T. J. Seguin and S. E. Wheeler, 2016. *ACS Catal.* **6**, 7222. Copyright 2016 American Chemical Society.

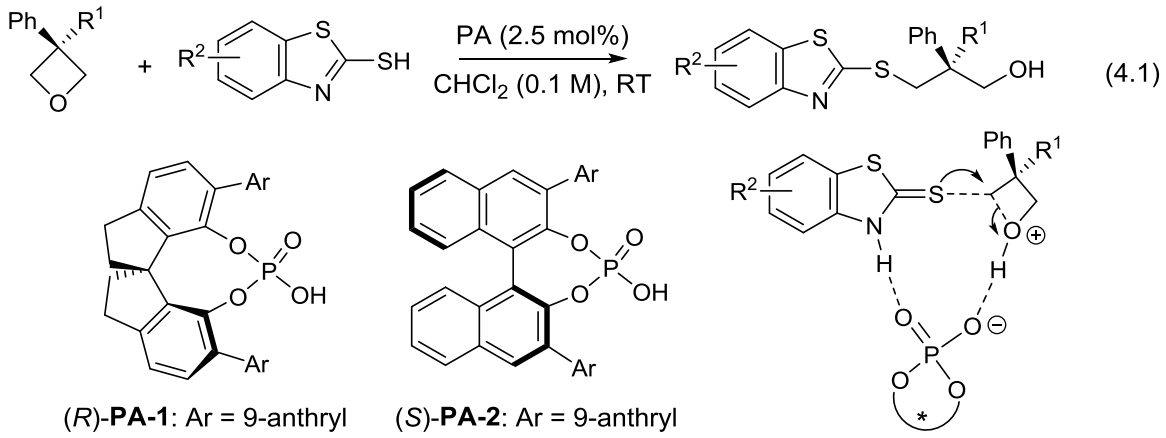

Scheme IV-1. Phosphoric acid catalyzed desymmetrization of 3-substituted oxetanes along with the stereocontrolling transition state (catalyst abbreviated for clarity).[58]

Sun's enantioselective oxetane ring-openings[58] are another entry in the bourgeoning field of chiral phosphoric acid catalysis.[18a, 18b, 60] In general, the often high levels of stereocontrol exhibited by these chiral diol-derived catalysts are thought to arise from stereospecific access of suitable substrates to a Brønsted acidic, chiral reactive site enclosed by tunable 3,3′-aryl substituents.[62] However, favorable cation-π, π-stacking, and CH···π interactions[33, 34d, 57e, 63] with the 3,3′-aryl groups have recently been identified as key elements of stereocontrol in many chiral phosphoric acid catalyzed reactions.[25b, 38, 57b-d, 57f] In addition, more general interactions of the substrates with the phosphoric acid functionality of these catalysts, including non-classical CH···O interactions,[25e] have proved pivotal in the stereoselectivity of a number of these

transformations.[25g, 28b, 29e, 45a, 46a-e, 46g-j, 64] For instance, we recently showed[65] that the enantioselectivities of chiral phosphoric acid catalyzed epoxide ring openings are driven by the stabilization of a fleeting positive charge in the transition state by the chiral electrostatic environment of the catalyst.

Table IV-1. Experimental *ee*'s and corresponding $\Delta\Delta G^{\ddagger}$ values (kcal mol^{-1}) for equation 4.1, along with the corresponding theoretical predictions.

Entry	Cat.	R^1	R^2	*ee* (exp.)[a]	$\Delta\Delta G^{\ddagger}$ (exp.)	*ee* (theor.)	$\Delta\Delta G^{\ddagger}$(theor.)
1	(*S*)-**PA-2**	H	H	44%	0.6	64%	0.9
2	(*R*)-**PA-1**	H	H	88%	1.6	87%	1.6
3	(*R*)-**PA-1**	Me	H	77%	1.2	77%	1.2
4	(*R*)-**PA-1**	OH	H	97%	2.5	>99%	4.3
5	(*R*)-**PA-1**	OH	5-OMe	>99%	>3.1	>99%	4.9

[a] Experimental data from Ref [58].

For Sun's oxetane openings,[58] catalyst screening yielded optimal enantioselectively with the SPINOL-derived **PA-1**;[66] BINOL-derived **PA-2**[60g, 67] proved far less selective. Sun *et al*.[58] proposed the TS model depicted in Figure IV-1, which is consistent with conventional stereochemical models of phosphoric acid catalyzed reactions.[2] In this model, the oxetane accepts a hydrogen bond from the phosphoric acid while the nucleophile donates a hydrogen bond to the catalyst. Meanwhile, the larger substituent at the 3-position of the oxetane (denoted "R_L" in Figure IV-1) is

preferentially oriented away from the flanking aryl groups of catalyst and the observed enantioselectivity was proposed to arise from favorable nucleophilic attack of the more accessible side of the oxetane. In other words, steric interactions in the disfavored transition state (TS) between the nucleophile and the catalyst were assumed to be responsible for enantioselectivity.

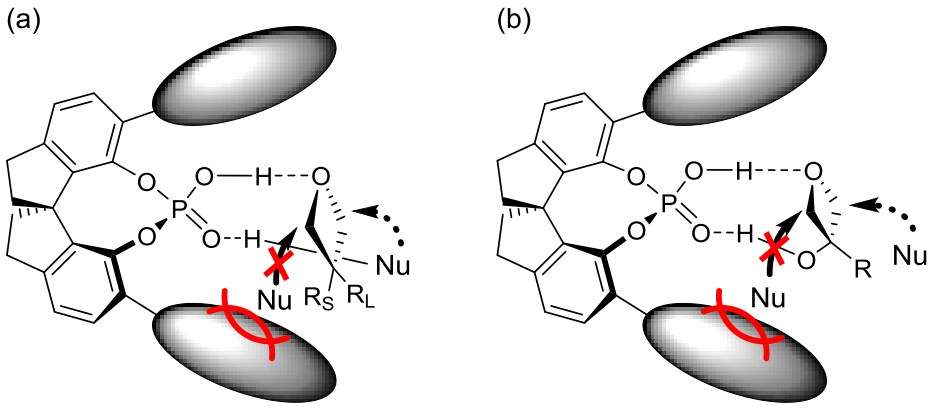

Figure IV-1. TS models proposed by Sun and co-workers[58] to explain the stereoselectivity of Equation (1) for (a) cases in which the oxetane contains alkyl substituents at the 3-position and (b) cases in which the oxetane contains an OH group at the 3-position.

One intriguing aspect of the enantioselectivity of equation 4.1 in Scheme IV-1 is the dependence not just on the catalyst but also on the substituents at the 3-position of the oxetane. For instance, **PA-1** provides excellent selectivity (*ee* = 88%) for R^1 = H

(Entry 2, Table IV-1), and similar *ee*'s were observed with a range of other substituents in place of the phenyl group (see Ref [58]). In disubstituted cases, where R^1 was varied, the *ee* was much more sensitive to the nature of the second substituent. For example, the *ee* was reduced to 77% for R^1 = Me (Entry 3, Table IV-1). However, when R^1=OH (Entry 4), a marked increase in selectivity was observed (*ee* = 97%). Supported by data from NMR studies, Sun *et al*.[58] postulated that the OH group stabilizes the favored transition state by hydrogen bonding to the catalyst, disrupting the hydrogen bond between nucleophile and catalyst (see Figure IV-1b). Incorporation of a 5-OMe substituent on the nucleophile further enhanced the selectivity (*ee* > 99%; Entry 5).

Herein, we quantify the myriad non-covalent interactions that control the enantioselectivity of these reactions, providing insight into the many avenues for achieving high degrees of stereoselectivity with phosphoric acid catalysts. Ultimately, we show that there is not a single stereochemical model for these reactions; instead, the mode of stereoinduction changes markedly with small variations in substrate and catalyst, which results from the interplay of many relatively modest non-covalent interactions.

4.2. Theoretical Methods

All computations were carried out using Gaussian 09.[51] Geometries, vibrational frequencies and thermal free energy corrections were computed at the B97-D/def2-TZVP level of theory.[8, 47] Transition state structures were verified based on the presence of a single imaginary vibrational frequency. Solvent effects (dichloromethane) were

accounted for with the SMD model.[68] Reported free energies (298K) were evaluated at the SMD-B97-D3/def2-TZVP//SMD-B97-D/def2-TZVP level,[8, 11a, 47] and include thermal free energy corrections based on the quasi-RRHO method of Grimme.[69] Predicted *ee*'s are based on the difference in free energy between the lowest-lying TS structure leading to the favored (TSX) and disfavored stereoisomer (TSX′), *i.e.* $\Delta\Delta G^{\ddagger} = G^{\ddagger}(TSX') - G^{\ddagger}(TSX)$, where X = 1 – 5 corresponds to the entry numbers from Table IV-1. Molecular structure figures were generated using CYLview.[70]

4.3. Results and Discussion

The rate-limiting transition state of equation 4.1 reflects an S_N2-like mechanism in which nucleophilic attack takes place simultaneously with opening of the oxetane ring (see Scheme IV-1). The proton is nearly completely transferred from the catalyst to the oxetane, rendering the catalyst and substrate an ion-pair in the transition state. As observed previously for phosphoric acid catalyzed epoxide ring openings,[65] the thione tautomer is the active form of the mercaptobenzothiazole nucleophile and donates a hydrogen bond to the phosphoryl oxygen of the catalyst in all low-lying TS structures. After the ring-opening step, the catalyst is regenerated by a subsequent proton transfer from the nucleophile. Extensive conformational searches were performed to identify the lowest-lying TS structures for Entries 1-5 of Table IV-1 (see Appendix C for more details). Only the lowest-lying TS structures leading to the major and minor enantiomers, denoted by TSX and TSX′, respectively, are discussed.

Overall, the predicted enantioselectivities are in excellent agreement with the experimental data,[58] providing not only the correct trend in selectivity but near quantitative reproduction of many of the experimental *ee*'s. In some cases, TSX and TSX′ are structurally similar; however, in other cases, the substrate conformations in TSX and TSX′ differ substantially, complicating comparisons across different Entries in Table IV-1. In order to unravel the mode of stereoinduction in Entries 1-5, the gas-phase energy difference between TSX and TSX′ ($\Delta\Delta E^{\ddagger}$) was decomposed into the difference in energy required to distort the substrate ($\Delta\Delta E_{sub}$) and catalyst ($\Delta\Delta E_{cat}$) into the TS geometries, as well as the difference in interaction energies between these distorted species ($\Delta\Delta E_{int}$),[57f]

$$\Delta\Delta E^{\ddagger} = \Delta\Delta E_{sub} + \Delta\Delta E_{cat} + \Delta\Delta E_{int}.$$

These data for entries 1-5 are provided in Table IV-2 and plotted in Figure IV-3a. Here, $\Delta\Delta E_{int}$ quantifies the contribution of non-covalent interactions between the catalyst and substrate to the energy separation between TSX and TSX′; $\Delta\Delta E_{cat}$ and $\Delta\Delta E_{sub}$ quantify the relative distortion energies of each of these species. In some cases, $\Delta\Delta E_{cat}$ and $\Delta\Delta E_{sub}$ are impacted by intramolecular non-covalent interactions, which are identified and discussed below. We also note that the contribution to the energy separation between TSX and TSX′ arising from differences in forming and breaking covalent bonds will be a component of $\Delta\Delta E_{sub}$ in this analysis.

Non-covalent interactions between the substrates and catalyst are ubiquitous in chiral phosphoric acid catalyzed reactions,[57b, 57c, 57f, 65, 71] and the reactions in Scheme IV-1 are no exception. We considered a series of truncated model systems (M1 – M4,

Figure IV-2) to quantify the impact of particular non-covalent interactions on the energy of TSX′ relative to TSX for Entries 1-5. In each case, we started with the lowest-lying TS structures and replaced key structural components with hydrogen atoms, whose positions were then optimized while keeping all other atoms fixed. The interaction energy of the resulting complex was then evaluated. The introduction of these hydrogen atoms is expected to minimally perturb the corresponding non-covalent interactions, and these individual contributions to $\Delta\Delta E_{int}$ sum to the value for the intact system within a few tenths of a kcal mol^{-1} in each case (see Table IV-2).[g] Models M1 and M2 quantify the impact of non-covalent interactions of the substrates with the 9-anthryl groups. The interaction energies for M1 and M2 were evaluated as the interaction between an anthracene as one fragment and the substrate and the phosphoric acid as the other fragment. For M3, the catalyst was reduced to the core phosphoric acid functionality. $\Delta\Delta E_{int}$(M3) is defined as the interaction energy between the protonated substrate and the phosphate anion, and primarily reflects the contribution of interactions between the protonated substrate and the catalyst phosphate oxygens in the TS structure. Finally, M4 consists of only the nucleophile and the scaffold of the catalyst (either BINOL or SPINOL), capturing the impact of differential interactions between the nucleophile and catalyst backbone. These contributions to $\Delta\Delta E_{int}$ are plotted in Figure IV-3b.

[g] This decomposition is certainly not unique, and we explored many other approaches. However, these all led to more significant discrepancies between the total difference in interaction energies and the sum of individual contributions.

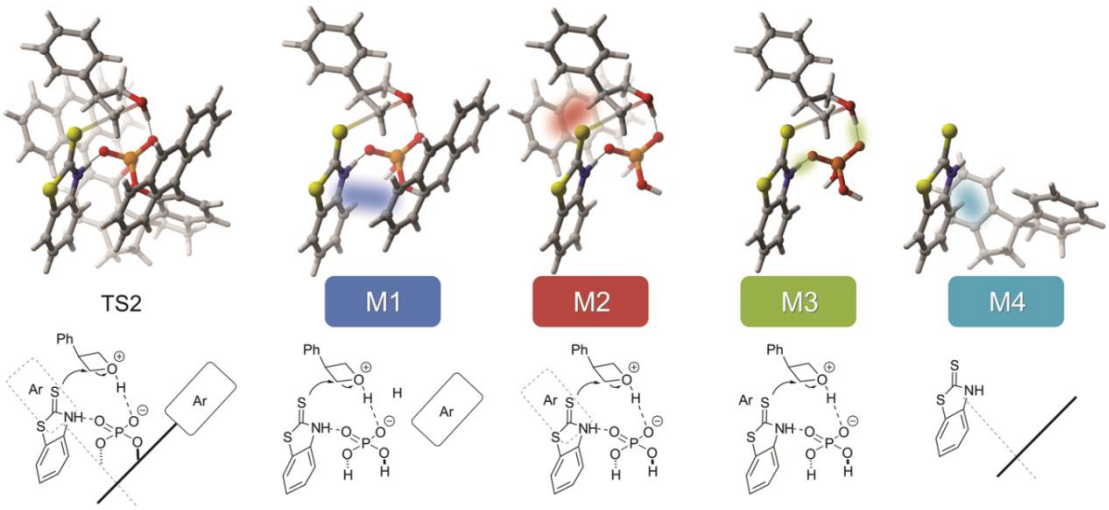

Figure IV-2. Representative TS structure (TS2) and the corresponding truncated models (M1-M4) used to quantify the contribution of different non-covalent interactions to the energy difference between TSX and TSX′.

For monosubstituted oxetanes (R^1 = H), the SPINOL-derived catalyst **PA-1** (Entry 2, Table IV-1) provides enhanced enantioselectivities compared to BINOL-derived **PA-2** (Entry 1). This can be understood in terms of the operative non-covalent interactions. For **PA-2**, the predicted *ee* (64%) is in good agreement with the experimental value of 44%. The computed $\Delta\Delta G^{\ddagger}$ and $\Delta\Delta E^{\ddagger}$ values are 0.9 and 1.5 kcal mol^{-1}, respectively. The contributions to $\Delta\Delta E^{\ddagger}$ show that distortions of the substrate and catalyst ($\Delta\Delta E_{sub}$ and $\Delta\Delta E_{cat}$, which are 4.7 and 1.9 kcal mol^{-1}, respectively) strongly favor TS1. The difference in substrate structure consists primarily of the inversion of the phenyl and hydrogen substituents at the 3-position of the oxetane. As a result, in TS1 the phenyl ring engages in a π-stacking interaction with the incoming nucleophile, while

there is no such interaction in TS1′. The contribution of this interaction to $\Delta\Delta E_{sub}$ was quantified by replacing the phenyl group of the substrate with a hydrogen atom that was optimized while keeping all other atoms fixed. The difference in energy for the substrate fell to 0.7 kcal mol^{-1}. Therefore, this intramolecular π-stacking interaction between the substrates contributes approximately 4 kcal mol^{-1} to $\Delta\Delta E^{‡}$. This is largely offset by $\Delta\Delta E_{int}$, which strongly favors TS1′. The truncated models (M1 – M4) indicate that interactions of the substrates with the 9-anthryl and phosphoric acid groups of the catalyst are somewhat balanced in TS1 and TS1′. Instead, the largely negative $\Delta\Delta E_{int}$ value is primary due to CH···π interactions of the nucleophile with the catalyst BINOL backbone [$\Delta\Delta E_{int}$(M4) = -5.2 kcal mol^{-1}]. This is a consequence of the smaller distance between the nucleophile and catalyst backbone in TS1′ compared to TS1. Thus, overall, the modest degree of enantioselectivity in Entry 1 arises from the compensating effects of the nucleophile-catalyst CH···π interactions that stabilize TS1′ and the π-stacking interactions that stabilize TS1 (see Figure IV-4a).

Table IV-2. Gas-phase $\Delta\Delta E^{‡}$, $\Delta\Delta E_{cat}$, $\Delta\Delta E_{sub}$, and $\Delta\Delta E_{int}$ for Entries 1-5 of Table IV-1, along with $\Delta\Delta E_{int}$ for model systems M1-M4, in kcal mol^{-1}.

Entry	$\Delta\Delta E^{‡}$	$\Delta\Delta E_{cat}$	$\Delta\Delta E_{sub}$	$\Delta\Delta E_{int}$	$\Delta\Delta E_{int}$(M1)	$\Delta\Delta E_{int}$(M2)	$\Delta\Delta E_{int}$(M3)	$\Delta\Delta E_{int}$(M4)
1	1.5	1.9	4.7	-5.1	1.8	-0.9	-1.0	-5.2
2	3.3	0.3	-0.7	3.7	-0.2	-0.8	0.0	4.4
3	1.0	0.7	-0.4	0.8	-0.1	-0.4	1.0	0.0
4	5.0	0.1	-1.2	6.1	-0.4	-2.5	9.2	0.0
5	5.6	1.9	-0.5	4.3	-1.9	2.9	3.4	0.2

For **PA-1**, the predicted *ee* of 87% is in even better agreement with the experimental value (88%). Unlike Entry 1, in this case TS2 and TS2′ adopt qualitatively different conformations, which leads to qualitative differences in the operative non-covalent interactions. The solution-phase free energy difference between TS2 and TS2′ is 1.6 kcal mol^{-1}; in the gas-phase, this energy difference is 3.3 kcal mol^{-1}, indicating that solvent and entropy effects degrade the enantioselectivity of this particular reaction. The contribution of the catalyst and substrate distortion energies are relatively small, and mostly cancel ($\Delta\Delta E_{cat}$ = 0.3 and $\Delta\Delta E_{sub}$ = -0.7 kcal mol^{-1}). Consequently, the stereoselectivity is primarily due to $\Delta\Delta E_{int}$ (3.7 kcal mol^{-1}). Models M1 - M4 indicate that the majority of this energy difference arises from CH···π interactions of the nucleophile with the SPINOL backbone of the catalyst [$\Delta\Delta E_{int}$(M4) = 4.4 kcal mol^{-1}]. However, unlike Entry 1, in this case these CH···π interactions preferentially stabilize TS2 significantly, enhancing the enantioselectivity. This effect is compensated slightly by solvent and entropy effects, as well as π-stacking and CH···π interactions between the substrates and 9-anthryl groups (which favor TS2′), resulting in the appreciable level of stereoselectivity observed for this system (see Figure IV-4b).

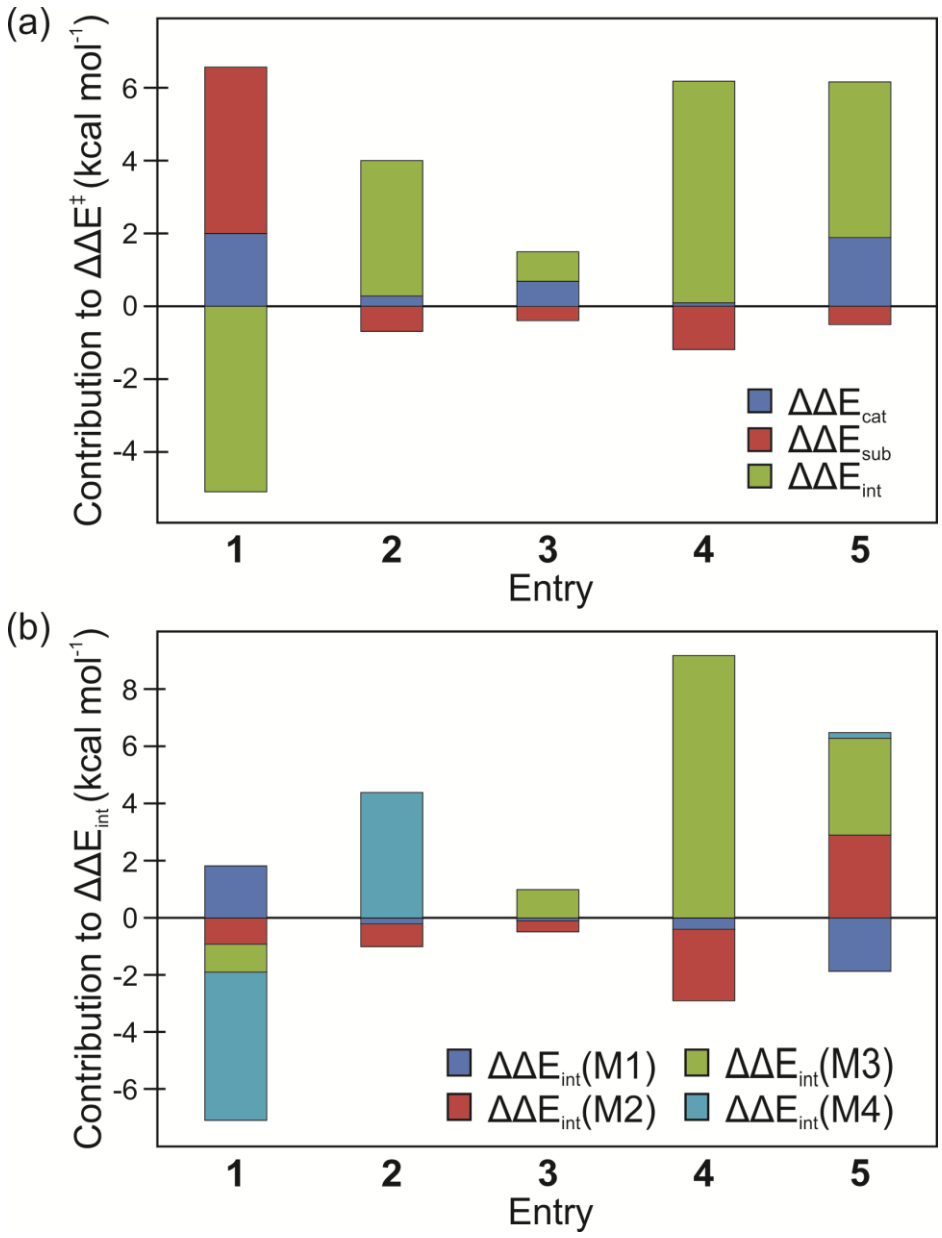

Figure IV-3. (a) Contributions to $\Delta\Delta E^{‡}$ for entries **1**-**5**; (b) Approximate contributions to $\Delta\Delta E_{int}$ for entries **1**-**5** based on models **M1** – **M4**.

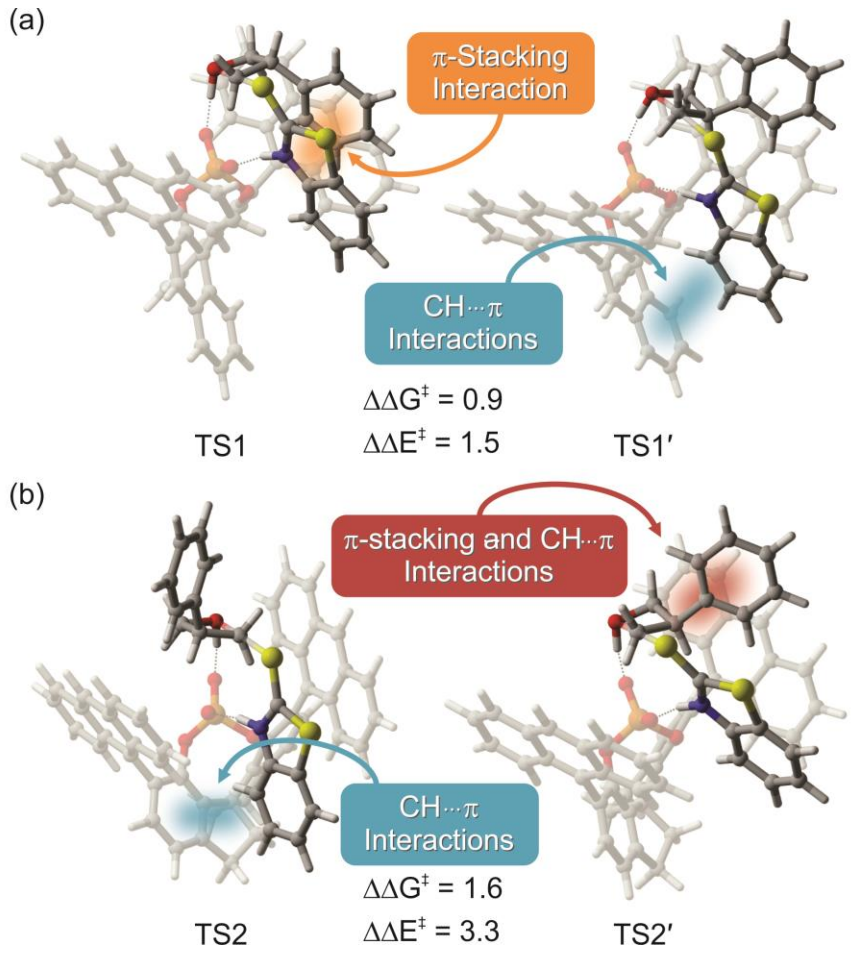

Figure IV-4. Non-covalent interactions primarily responsible for the enantioselectivity of (a) Entry 1 and (b) Entry 2. Free energy and energy differences are in kcal mol^{-1}.

The addition of a second substituent at the 3-position of the oxetane can either increase or decrease the enantioselectivity. For instance, with R^1 = Me and **PA-1** (Entry 3 of Table IV-1, 77% for both experimental and theoretical *ee*) the enantioselectivity is reduced slightly compared to the corresponding monosubstituted case (Entry 2). For Entry 3, the gas-phase energy difference ($\Delta\Delta E^{\ddagger}$ = 1.0 kcal mol^{-1}) and solution phase free energy difference (1.2 kcal $mole^{-1}$) are nearly identical. The catalyst distortion energy

($\Delta\Delta E_{cat}$ = 0.7 kcal mol^{-1}) and substrate distortion energy ($\Delta\Delta E_{sub}$ = -0.4 kcal mol^{-1}) again largely cancel, and the energy difference between TS3 and TS3′ arises primarily from $\Delta\Delta E_{int}$. From the truncated model systems, the largest contribution to $\Delta\Delta E_{int}$ is 1.0 kcal mol^{-1} from $\Delta\Delta E_{int}$(M3). In this case, $\Delta\Delta E_{int}$(M3) is due to favorable CH···O interactions between the methyl group at R^1 and the phosphoric acid in TS3 (see Figure IV-5). In support of this view, a modified M3 model in which this methyl group was replaced with a hydrogen reduces $\Delta\Delta E_{int}$(M3) to 0.4 kcal mol^{-1}. Notably, $\Delta\Delta E_{int}$(M4) is 0.0 kcal mol^{-1}, showing that CH···π interactions between the nucleophile and SPINOL scaffold are perfectly balanced in TS3 and TS3′. This is in stark contrast to the monosubstituted oxetane systems, in which these interactions played a major role in the selectivity. Thus, the introduction of a simple Me substitutent at the 3-position of the oxetane changes the relative importance of the operative non-covalent interactions, leading to a marked shift in the mode of stereoinduction.

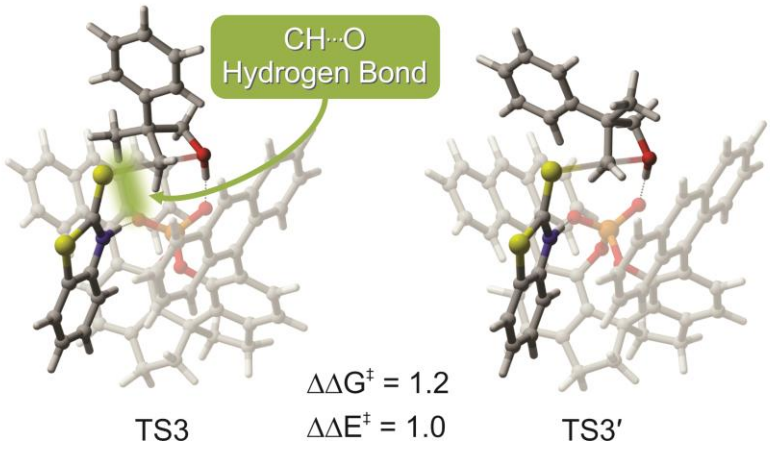

Figure IV-5. Non-covalent interactions primarily responsible for the enantioselectivity of Entry 3. Free energy and energy differences are in kcal mol^{-1}.

Experimentally, excellent selectivity was observed for oxetanes bearing a hydroxyl group at the R^1 position.[58] For Entry 4, the experimental and theoretical *ee*'s are 97% and >99%, respectively. Somewhat surprisingly, TS4 and TS4′ are structurally nearly identical to TS3 and TS3′, respectively, despite the presence of an additional hydrogen-bonding group on the oxetane in Entry 4. In TS4, the hydroxyl group at R^1 hydrogen bonds to the phosphoric acid oxygen, as proposed by Sun and co-workers (Figure IV-1);[58] however, in contrast to their TS model, the hydrogen bond between the catalyst and nucleophile remains intact in the favored TS. Although this same hydrogen bonding arrangement was present in some TS conformations leading to the disfavored enantiomer, these are all at least 0.4 kcal mol^{-1} higher in free energy than TS4′, in which this OH group is engaged in an OH···π interaction with one of the 9-anthryl groups of the catalyst (see Figure IV-6a). The total $\Delta\Delta E_{int}$ for TS4 and TS4′ is 6.1 kcal mol^{-1}. A significant contribution to $\Delta\Delta E_{int}$ arises from differences in hydrogen bonding interactions; these are quantified in $\Delta\Delta E_{int}$(M3) and $\Delta\Delta E_{int}$(M2), which are 9.2 and -2.5 kcal mol^{-1}, respectively. To extract the contribution of the hydroxyl group interactions from these models, modified versions of the models were considered in which the hydroxyl group was replaced with a hydrogen atom while keeping all other atoms fixed. The resulting values for $\Delta\Delta E_{int}$(M3) and $\Delta\Delta E_{int}$(M2) were 0.6 and -0.4 kcal mol^{-1}, respectively. Comparing these and the corresponding values for the intact M3 and M2 models, an approximate relative interaction energy for the hydroxyl group can be found as 9.2 – 0.6 + [–2.5 – (–0.4)] = 6.5 kcal mol^{-1}. That is, the OH···O hydrogen bonding interaction in TS4 is 6.5 kcal mol^{-1} more favorable than the OH···π interaction in TS4′.

The remaining contributions to $\Delta\Delta E_{int}$ are relatively insignificant. These effects are tempered somewhat by $\Delta\Delta E_{sub}$ (-1.2 kcal mol^{-1}), leading to the final energy difference between TS4 and TS4′ of 5.0 kcal mol^{-1}. Thus, the high degree of enantioselectivity for Entry 4 can be ascribed almost entirely to the greater favorability of the OH···O interaction in TS4 compared to the OH···π interaction in TS4′.

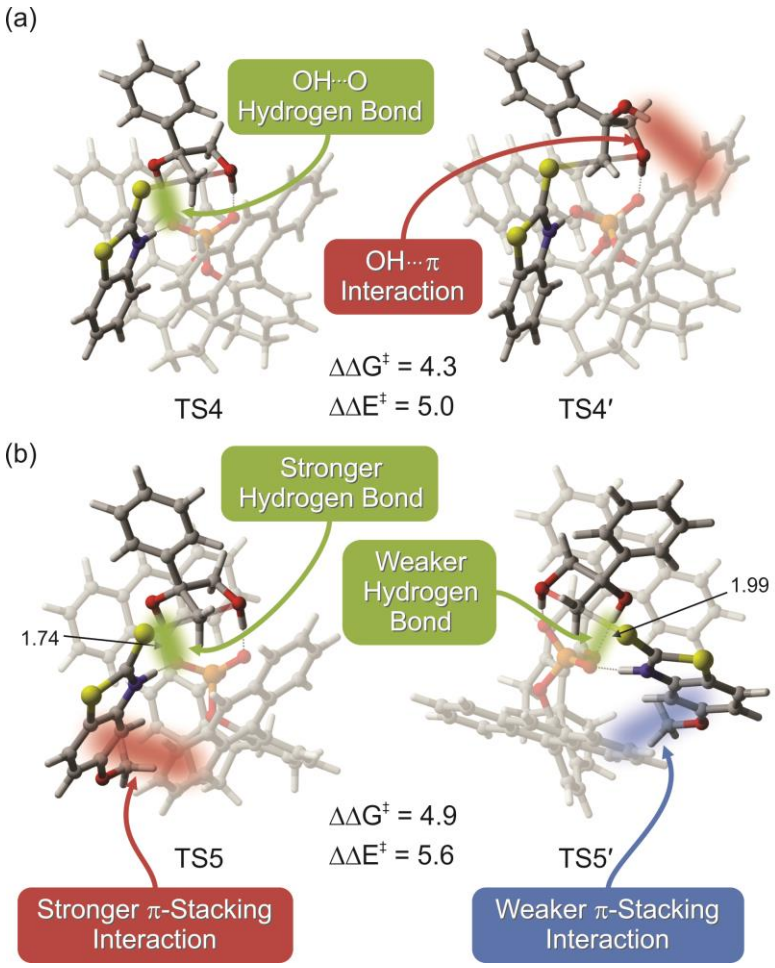

Figure IV-6. Non-covalent interactions primarily responsible for the enantioselectivity of (a) Entry 4 and (b) Entry 5. Free energy and energy differences are in kcal mol^{-1}.

Selectivity is further improved for this oxetane when the mercaptobenzothiazole nucleophile has a methoxy group at the 5-position (>99% *ee* for both experiment and theory). Our data reproduce this enhancement in enantioselectivity ($\Delta\Delta G^{\ddagger}$ = 4.3 and 4.9 kcal mol^{-1} for Entries 4 and 5, respectively, of Table IV-1). Like TS4, TS5 features an OH···O hydrogen bond involving the hydroxyl substituent at R^1, and is structurally similar to TS4. The 5-OMe engages in CH···π interactions with the catalyst SPINOL backbone. Unlike Entry 4, TS5 and TS5′ exhibit the same hydrogen bonding and CH···π interactions (see Figure IV-6b); indeed, the substrates in these two TS structures are near perfect mirror images of each other! For this system, $\Delta\Delta E^{\ddagger}$ = 5.6 kcal mol^{-1}. This comprises 1.9 kcal mol^{-1} from the distortion of the catalyst, -0.5 kcal mol^{-1} from the distortion of the substrate, and 4.3 kcal mol^{-1} from $\Delta\Delta E_{int}$. The large contribution of $\Delta\Delta E_{cat}$ in this case is consistent with conventional models of phosphoric acid catalysts; the accommodation of the substrate into the chiral bonding pocket of the catalyst requires less distortion in the favored TS5 than the disfavored TS5′. However, differences in non-covalent interactions also play a key role in the enantioselectivity of this reaction.

A key point of interest for Entry 5 is the contribution of the hydrogen bonding interaction between the R^1 hydroxyl group and phosphoric acid, which appear qualitatively similar in TS5 and TS5′. $\Delta\Delta E_{int}$(M3) = 3.4 kcal mol^{-1}, although this reflects not only the difference in hydrogen bond strength of the R^1 hydroxyl group but also the other interactions between the substrates and phosphoric acid functionality. The corresponding O-H···O bond distances and angles are 1.74 Å and 164.7° in TS5, and

1.99 Å and 162.7° in TS5′, which is consistent with a more favorable hydrogen bond in TS5. In order to estimate the contribution of the hydrogen bond from the OH group at R^1, M3 was modified by replacing this hydroxyl group with a hydrogen atom; $\Delta\Delta E_{int}$ decreased to 2.0 kcal mol^{-1}, suggesting a difference in this hydrogen bond strength of approximately 1.4 kcal mol^{-1} between TS5 and TS5′.[h] Thus, even though this hydrogen bonding interaction is present in both TS5 and TS5′, it is far weaker in the latter case. This is further supported by the existence of another TS structure leading to the disfavored stereoisomer (TS5″, see Appendix C Figure C-1) that is less than 0.1 kcal mol^{-1} higher in energy than TS5′. In TS5″, the hydroxyl group at R^1 is oriented toward the nearby 9-anthryl group of the catalyst. That is, in TS5′, the OH···O interaction between the R^1 hydroxyl and the catalyst is only slightly more favorable than an OH···π interaction, and considerably weaker than the OH···O interaction in TS5. There is also a contribution to $\Delta\Delta E_{int}$ from interactions of the substrates with the 9-anthryl groups, as captured by models M1 and M2. The sum of the contributions from these interactions, 1.0 kcal mol^{-1}, is largely unchanged when the oxetane and phosphate anion are removed (0.8 kcal mol^{-1}). Thus, the π-stacking interaction between the nucleophile and one of the 9-anthryl groups is approximately 0.8 kcal mol^{-1} more favorable in TS5 than in TS5′, contributing to the overall high degree of enantioselectivity.

[h] The remaining 2.0 kcal mol-1 is difficult to pinpoint, but is likely due to the accumulation of small effects arising from CH···O interactions between the electrophile and catalyst phosphate oxygens, the NH···O hydrogen bond of the nucleophile to a catalyst phosphate oxygen, and the hydrogen bond between the protonated oxetane oxygen and the catalyst.

While Entry 4 and Entry 5 differ only in the addition of a remote OMe group to the nucleophile in the latter case, this results in significant differences in the operative TS structures and modes of stereoinduction. While the enantioselectivity of Entry 4 arises from the greater favorability of a conventional OH···O hydrogen bond compared to an OH···π interaction, the enantioselectivity of Entry 5 is primarily a consequence of more favorable hydrogen bonding and π-stacking interactions in TS5 compared to TS5′.

4.4. Summary and Concluding Remarks

The role of non-covalent interactions on the enantioselectivity of the first organocatalytic oxetane ring-openings[58] were examined using DFT, focusing on the impact of catalyst and substrate structure on the enantioselectivity. Five variations of this transformation were considered, with *ee*'s ranging from 44% to >99%. Theoretical *ee* values are in excellent agreement with experiment. In contrast to the proposed TS model from Sun and co-workers[58] (Figure IV-1), we find that the enantioselectivity of these reactions is not primarily steric in origin. Moreover, the mode of stereoinduction differs markedly depending on the nature of the substrate. For monosubstituted oxetanes, CH···π interactions of the nucleophile with the catalyst backbone are a common driving force selectivity, reducing the selectivity for **PA-2** (Entry 1 of Table IV-1) and enhancing the selectivity for **PA-1** (Entry 2). For disubstituted oxetanes with **PA-1**, these CH···π are balanced in the competing TS structures and do not impact the enantioselectivity; instead, the selectivity is dependent on a number of other non-

covalent interactions. Notably, the particular non-covalent interactions that prove pivotal are sensitive to even remote changes in the substrates.

It is interesting to note that the modes of stereoinduction in these oxetane ring openings are distinct from that identified for chiral phosphoric acid catalyzed epoxide ring openings,[65] despite the outward similarity of these two reactions. In particular, we previously found that the enantioselectivity of *meso*-epoxide ring openings using the same mercaptobenzothiazole nucleophile was controlled primarily by the preferential electrostatic stabilization of a fleeting positive charge in the preferred TS structure; non-covalent interactions with the flanking aryl groups of the catalyst proved relatively unimportant, apart from restricting the orientation of the reacting substrates within the chiral electrostatic environment of the catalyst. It will be interesting to explore whether the stereoselectivity in other phosphoric acid catalyzed oxetane ring openings[61] will arise from the factors identified above or the electrostatic-based picture presented for epoxide ring openings.[65]

Overall, the observed changes in the modes of stereoinduction resulting from small changes in the substrate should serve as a clarion warning against the overgeneralization of stereochemical models, particularly in systems in which a multitude of competing non-covalent interactions are operative. As seen above, small substrate changes can shift the balance of non-covalent interactions, highlighting the difficulty of simultaneously harnessing the power of many competing non-covalent interactions within a complex molecular system.

CHAPTER V

STACKING AND ELECTROSTATIC INTERACTIONS DRIVE THE STEREOSELECTIVITY OF SILYLIUM ION-ASYMMETRIC COUNTERANION DIRECTED CATALYSIS[*]

Chiral anion-directed ion-pairing catalysis (*e.g*. asymmetric counteranion directed catalysis, ACDC)[3c, 72] has opened up vast new avenues for the development of highly effective catalysts.[3a, 73] However, theoretical work on the stereoselectivities of such transformations has lagged behind these experimental developments. Although modern computational methods have emerged as powerful tools for unravelling the mode of stereoinduction in asymmetric catalysis,[5b, 25a, 62c, 74] many conventional computational approaches are impotent in the face of ion-pairing catalysis due to the challenge of identifying the most favourable configuration of the ion-pair from among the 1000s of potential structures.[57e] These problems are exacerbated in cases in which the counteranion lacks clear recognition sites with which to engage with the substrate. Milo *et al*.[39b] circumvented this problem by marrying traditional physical organic and computational chemistry techniques with modern data analysis methods. Herein, we directly tackle a recent example of ion-pairing catalysis using computations, studying the silylium ion-ACDC of the Diels-Alder cycloaddition of cinnamate esters with

---

[*] T. J. Seguin and S. E. Wheeler: "Stacking and Electrostatic Interactions Drive the Stereoselectivity of Silylium Ion-Asymmetric Counteranion Directed Catalysis". *Angew. Chem. Int. Ed.*. 2016. Just Accepted Manuscript, DOI: 10.1002/anie.201609095R2. Copyright Wiley-VCH Verlag GmbH & Co. KGaA. Reproduced with permission.

cyclopentadiene (CP).[75] The results pinpoint electrostatic and dispersion-driven π-stacking interactions that underlie the enantio- and diastereoselectivities, and demonstrate the power of modern computational methods to tackle challenging problems in asymmetric organocatalysis.

List *et al.*[75] recently described a novel approach to asymmetric Diels-Alder cycloadditions of CP to ordinarily unreactive cinnamates[76] catalysed by chiral C-H acid **2** (see Scheme V-1). The active, anionic form of **2** forms an ion-pair with a silylium ion to create potent Lewis acid catalysts. List *et al.*[75] reported high *er* and *dr* for **2c** in the reaction using a TMS-substituted silyl ketene acetal with CP and fluorenylmethyl cinnamate ester **1** (see Table V-1). The *er* and *dr* were even higher with the more bulky TBS group (see Table V-1). Intriguingly, other catalysts surveyed produced nearly racemic mixtures of the *endo* product, but with relatively high *dr* values. Understanding the high enantio- and diastereoselectivities for catalyst **2c**, the lack of enantioselectivity for **2a** and **2b**, and the requirement of fluorenylmethyl esters for high stereoselectivities is central to the further development of this methodology.

The proposed catalytic cycle for the reaction in Scheme V-1 is depicted in Scheme V-2.[75] The active catalytic anion is the conjugate base of **2**, formed by a proton transfer to the silyl ketene acetal. An exchange of the Lewis base then forms an ion-pair consisting of the silylated cinnamate and binaphthyl-allyl-tetrasulfone (BALT) anion. The stereoselective Diels-Alder cycloaddition with CP in the chiral environment of the BALT anion, followed by exchange of the Lewis base, furnishes the enantiopure product.

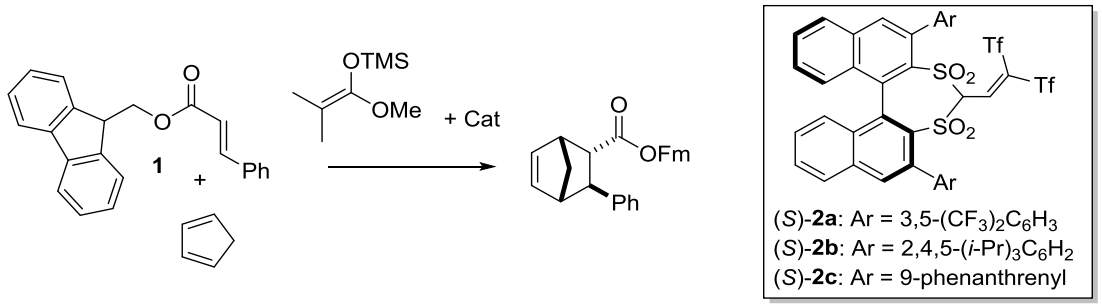

Scheme V-1. Silylium-ion ACDC of the Diels-Alder cycloaddition of cyclopentadiene to cinnamates.[75]

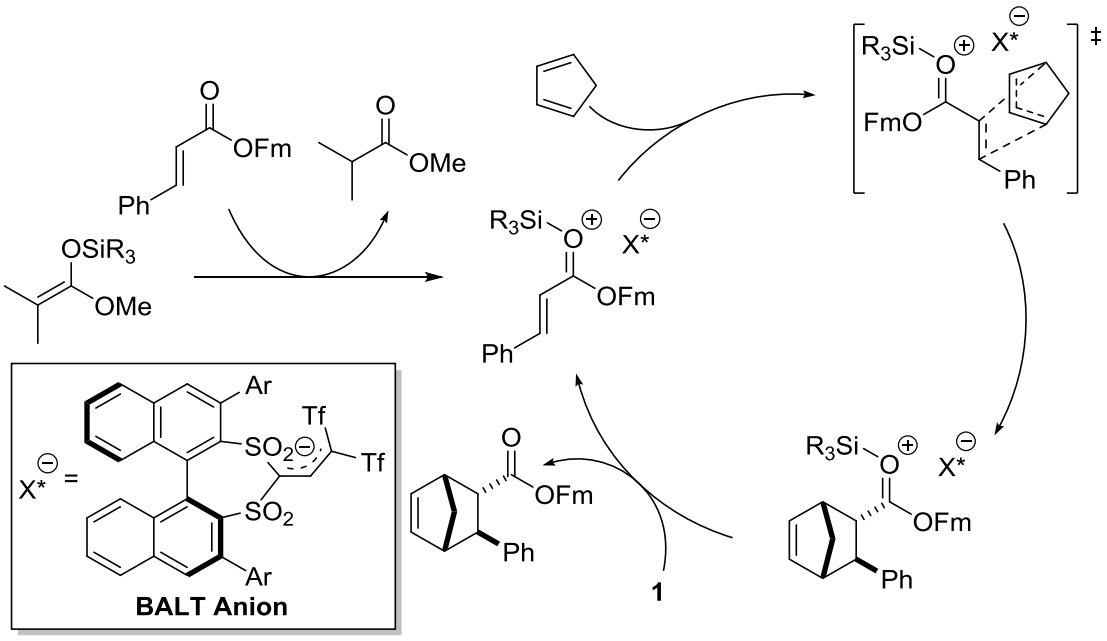

Scheme V-2. Catalytic cycle for the reaction in Scheme V-1, along with the active form of the catalyst (Tf: SO_2CF_3).

We have computed both the enantioselectivity and diastereoselectivity of four reactions for which List *et al*.[75] provided data (see Table V-1). Relative free energies were computed at the PCM-M06-2X/6-311G(d,p)//PCM-M06-2X/6-31G(d) level of theory[12, 48] using Gaussian 09[77] and an ultrafine integration grid.[78] Thermal corrections were computed within the quasi-RRHO approximation.[79] Computed *er* and *dr* values were based on the relative free energies of the corresponding TS structures, under the assumption that these reactions are under Curtin-Hammett control. The theoretical data is in very good agreement with experiment both in terms of *er* and *dr*. These stereochemical determinations required the identification of the lowest-lying transition state (TS) structures leading to the four potential stereoisomeric products arising from the *endo* and *exo* addition of CP to the two faces of the silylated cinnamate. Given the non-directional nature of the ion-pair formed by the highly delocalized anionic catalyst and cationic substrate[73g] as well as the conformational flexibility of both the dienophile and catalyst, identifying the most favourable orientation of the reacting substrates relative to the chiral counteranion was non-trivial. We sampled 1000s of low-lying conformations of the operative TSstructures leading to both enantiomers of the *endo* product (see Appendix D for details). After considerable effort, a TS structure leading to the disfavoured *endo* enantiomer, **TS(3′)$_{endo}$**, was identified as a particularly low-lying structure, exhibiting favourable shape and electrostatic complementarity between the substrates and counteranion. This configuration is also stabilized by CH···O hydrogen bonds[25e] and π-stacking interactions. Starting from this TS structure, we explored related conformations for TS structures leading to the four stereoisomers of the four entries in

Table V-1. The final enantiodetermining TS structures for Entry 3, which are representative of the stereocontrolling TS structures for most of the entries in Table V-1, are shown in Figure V-1a.[i]

Table V-1. Experimental and theoretical *er* and *dr* values and corresponding $\Delta\Delta G^{\ddagger}$ values, in kcal mol^{-1}. All reactions were run in toluene at 25 °C, except where noted (TMS: trimethylsilyl; TBS: tert-butyldimethylsilyl).

Entry	Cat.	Silyl Group	Exp.		Theor.		Exp.		Theor.	
			er	$\Delta\Delta G^{\ddagger}$	*er*	$\Delta\Delta G^{\ddagger}$	*dr*	$\Delta\Delta G^{\ddagger}$	*dr*	$\Delta\Delta G^{\ddagger}$
1	(*S*)-**2a**	TMS	56:44	0.1	62.9:37.1	0.3	13:1	1.5	16:1	1.6
2	(*S*)-**2b**	TMS	56.5:43.5	0.2	43.3:56.7	-0.2	13:1	1.5	116:1	2.8
3	(*S*)-**2c**	TMS	86.5:13.5	1.1	>99:1	4.5	18:1	1.7	57:1	2.4
4[a]	(*S*)-**2c**	TBS	97:3	1.7	>99:1	5.5	>25:1	>1.9	219:1	2.7

[a] Temperature was -20 °C and Et_2O was used as solvent.

[i] TS structures are named based on the corresponding Entry in Table V-1, whether the TS leads to the favoured or disfavoured (denoted by a prime) enantiomer, and whether the TS leads to the endo or exo adduct. For instance, TS(3)endo is the lower-lying endo TS for entry 3, whereas TS(3')endo is the most favourable endo TS leading to the disfavoured enantiomer for this entry.

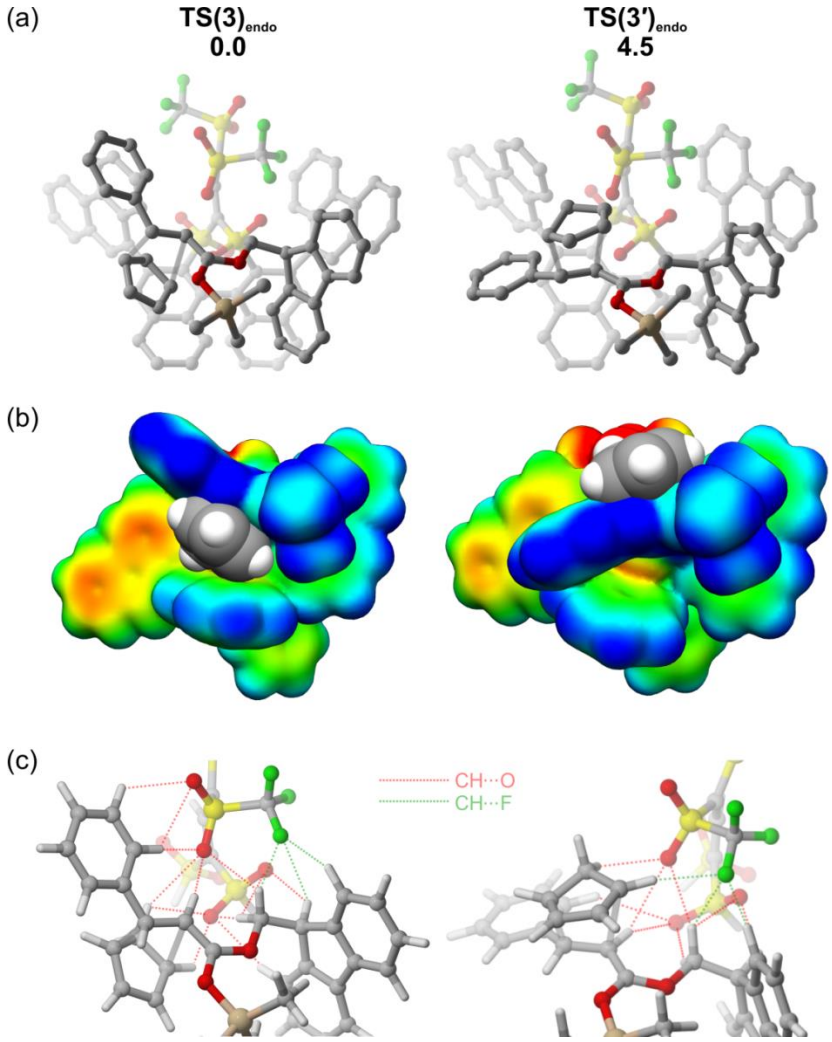

Figure V-1. (a) Enantiodetermining TS structures for Entry 3 of Table V-1, along with the relative free energies in kcal mol^{-1} (hydrogens have been removed for clarity). (b) ESPs of **TS(3)$_{endo}$** and **TS(3′)$_{endo}$** in the absence of the CP (red = -30 kcal mol^{-1}; blue = +30 kcal mol^{-1}), along with the VDW representation of the CP. (c) Closer view of CH···O and CH···F interactions in these TS structures (the phenanthrenyl groups have been removed for clarity). Interaction distances less than 3 Å are shown.

In the enantiodetermining TS structures, the substrates bind through a network of CH···O and CH···F interactions as well as π-stacking interactions, most notably between the fluorenylmethyl functionality (OFm) on the substrate and a phenanthryl substituent

of the catalyst. Unexpectedly, the preferred TS structure, **TS(3)$_{endo}$**, features the addition of CP to the buried face of the cinnamate (see Figure V-1a); the TS for *endo* addition of CP to the exposed face, **TS(3′)$_{endo}$**, lies 4.5 kcal mol^{-1} higher in free energy. To probe the origin of this free energy difference and to explain the preferential addition to the hindered face of the dienophile, the difference in gas-phase energies of these TS structures was decomposed into the difference in energy of the substrates ($\Delta\Delta E_{sub}$) and the catalyst ($\Delta\Delta E_{cat}$) in the TS geometries, as well as the difference in interaction energy between the distorted catalyst and the substrates ($\Delta\Delta E_{int}$), $\Delta\Delta E^{\ddagger} = \Delta\Delta E_{sub} + \Delta\Delta E_{cat} + \Delta\Delta E_{int}$.[17, 45c] These data are presented in Table V-2. The contributions of individual noncovalent interactions to $\Delta\Delta E_{int}$ were approximately quantified using a series of truncated model systems (see Appendix D Figure D-1). The corresponding data is available in Appendix D Table V-S1.

The large energy separation between the enantiocontrolling TS structures for Entries 3 and 4 arises primarily from differences in noncovalent interactions ($\Delta\Delta E_{int}$ = 6.2 and 5.9 kcal mol^{-1}, respectively). The favoured TS structure in both cases is nearly identical, and features the CP nestled within a cleft formed by the interface of the silylated cinnamate and catalyst (see Figure V-1b). This results in stabilizing stacking interactions between the CP and the catalyst in **TS(3)$_{endo}$** and **TS(4)$_{endo}$**,[80] which apparently outweigh dispersion interactions between the exposed CP and solvent (either toluene or Et_2O) in the disfavoured *endo* TS. Indeed, the experimental observation of enhanced *er* values using Et_2O rather than toluene is consistent with dispersion

interactions of the CP with the solvent partially stabilizing the disfavoured TS.[j] Complementing these interactions are stronger CH···O interactions that also preferentially stabilize **TS(3)$_{endo}$** and **TS(4)$_{endo}$**, while CH···F interactions between a triflate CF_3 group and the repositioned CP as well as the OFm group of the substrate reduce the overall enantioselectivity slightly by preferentially stabilizing **TS(3′)$_{endo}$** and **TS(4′)$_{endo}$** (see Figure V-1c; see Appendix D for more details).

With regard to the non-enantioselective catalysts (Entries 1 and 2), the binding modes in **TS(1)$_{endo}$** and **TS(2)$_{endo}$** are qualitatively similar to those in **TS(3)$_{endo}$** and **TS(4)$_{endo}$**. However, **TS(1′)$_{endo}$** and **TS(2′)$_{endo}$** exhibit a binding mode in which the fluorenyl group of the substrate stacks with the binaphthyl backbone of the catalyst (see Appendix D Figure D-2), rather than with the 9-phenanthrenyl group as in **TS(3′)$_{endo}$** and **TS(4′)$_{endo}$**. That is, for catalysts lacking the 9-phenanthrenyl group, the crucial π-stacking interactions between this group and the fluorenylmethyl group are lost. The origin of the small energy differences between the two *endo* TS structures for Entries 1 and 2 was again examined through distortion/interaction analysis. For Entry 1, the –0.7 kcal mol^{-1} energy difference between **TS(1)$_{endo}$** and **TS(1′)$_{endo}$** is due to nearly balanced differences in catalyst distortion energy [favouring **TS(1)$_{endo}$**] and the interaction energy [favouring **TS(1′)$_{endo}$**)]. The former arises primarily from the unfavourable geometry of the binaphthyl group in **TS(1′)$_{endo}$**, while the largest contributions to the latter are stabilizing CH···π and CH···F interactions between the fluorenyl group and a 3,5-

[j] Et_2O is less polarizable than toluene, so will engage in weaker dispersion interactions with the exposed CP in transition states such as TS(3')endo. The inability of continuum solvent models to fully account for such interactions likely contributes to the overestimation of stereoselectivities of these reactions.

$(CF_3)_2C_6H_3$ group of the catalyst (see Figure V-2a; for more details, see Appendix D). For Entry 2, the gas-phase energy difference, 1.8 kcal mol^{-1}, reflects the offsetting impact of catalyst and substrate distortion [favouring **TS(2′)$_{endo}$**] and the difference in interaction energies that favour **TS(2)$_{endo}$**. The catalyst geometry in **TS(2′)$_{endo}$** is more favourable than in **TS(2)$_{endo}$** due to the presence of intramolecular CH···F/O interactions between the ^{i}Pr groups and sulfonate oxygens and triflate CF_3 groups in the former case. The interaction energies favour **TS(2)$_{endo}$** due to the presence of stabilizing CH···π interactions between the phenyl group of the dienophile and an ^{i}Pr group of the catalyst and between the fluorenyl group of the dienophile and another catalyst ^{i}Pr group. Another component of the difference in interaction energy is a difference in CH···O and CH···F hydrogen bonds, where, similarly to Entries 3 and 4, a characteristic of the weaker electrostatic interactions with the core of the catalyst in **TS(2′)$_{endo}$** is the exchange of some CH···O hydrogen bonds for CH···F hydrogen bonds (see Appendix D).

Table V-2. Gas phase difference in energy ($\Delta\Delta E^{\ddagger}$), difference in substrate energy ($\Delta\Delta E_{sub}$), difference in catalyst energy ($\Delta\Delta E_{cat}$), and difference in interaction energy ($\Delta\Delta E_{int}$) for the lowest-lying *endo* TSs for Entries 1-4 of Table V-1, in kcal mol^{-1}.

Entry	$\Delta\Delta E^{\ddagger}$	$\Delta\Delta E_{cat}$	$\Delta\Delta E_{sub}$	$\Delta\Delta E_{int}$
1	-0.7	6.1	0.0	-6.8
2	1.8	-5.0	-1.6	8.4
3	5.1	-0.7	-0.4	6.2
4	5.3	-1.1	0.5	5.9

The diastereoselectivities of these reactions exceed 13:1 for all four systems regardless of the *er* value for the *endo* products, implying at least a 1.5 kcal mol^{-1} gap in free energy between the lowest lying *exo* and *endo* TS structures. We located *exo* transition state structures by starting from conformers of the *endo* TS structures and rotating the CP by 180°. For Entries 1, 3 and 4, the conformation of the lowest-lying *exo* TS was the same as the lowest-lying *endo* TS, but with the CP rotated. That is, in both diastereocontrolling TS structures, the CP ring sits within the cleft formed by the catalyst and dienophile. Despite this, distortion/interaction analysis of Entries 3 and 4 indicate that the differences in gas phase energies are due primarily to differences in interaction energies (see Table V-3). Analyses of the truncated models (see Appendix D) reveal that these differences are a consequence of the orientation of the CP within the chiral electrostatic environment of the catalyst. The partial charges on the CP hydrogens are not uniformly distributed, with the CH_2 hydrogens bearing more substantial positive charge than their sp^2-hybridized counterparts (see Figure V-2b). Concurrently, the electrostatic environment of the CP ring, arising from the electrostatic potential (ESP) of the dienophile and counteranion, is highly inhomogeneous. In the *endo* TS structures, the CH_2 hydrogens are in a more favourable electrostatic environment than they are in the *exo* TS structures (see Figure V-2b). Consequently, the $CH_2 \cdots O$ hydrogen bonds in the *endo* TS structures are electrostatically more favourable than the corresponding $CH \cdots O$ hydrogen bonds in the *exo* TS structures. Such an electrostatic mode of stereoinduction, in which stereoselectivity arises from changes in the orientation of a substrate within the

highly inhomogeneous electrostatic environment of a catalyst, has been observed previously.[52, 81]

For Entry 1, which is less diastereoselective, similar electrostatic interactions are operative. However, in this case the difference in interaction energies is dominated by the competition between CH···F interactions between a CH_2 hydrogen on CP with a CF_3 group on the catalyst aryl substituent that preferentially stabilize **TS(1)$_{endo}$** as well as stronger π-stacking interactions between CP and the binaphthyl backbone that favour **TS(1)$_{exo}$**. For Entry 2, the lowest-lying *exo* TS structure is qualitatively different from the lowest-lying *endo* TS structure, complicating the isolation of a particular origin of the diastereoselectivity (see Appendix D).

The correct identification of these stereocontrolling TS structures required considerable computational expense. Such a brute force approach was necessitated by the conformational flexibilities of the dienophile and catalyst and the lack of reasonable intuition regarding their probable binding modes. Examining the ESPs of the separated substrates and catalyst in their geometries from **TS(3)$_{endo}$** (Figure V-2c), it is clear that areas of relatively low ESP on the catalyst are paired with regions of relatively high ESP on the reacting substrates, and one can rationalize this binding mode based on the underlying electrostatic interactions. However, it is equally clear that there are many other binding modes expected to maximize such electrostatic interactions due to the delocalized regions of negative ESP associated with the catalyst. Instead, the geometry of the preferred binding mode, which underlies both the enantio- and diastereoselectivity, is dependent on the formation of favourable π-stacking interactions

between the fluorenyl and Ph groups of the substrate and the 9-anthryl groups of the catalyst. This explains the dependence of the reaction in Scheme V-1 on the presence of this fluorenyl group in order to achieve high stereoselectivities, and suggests that an alternative approach will be required to extend this reaction to other cinnamate esters.

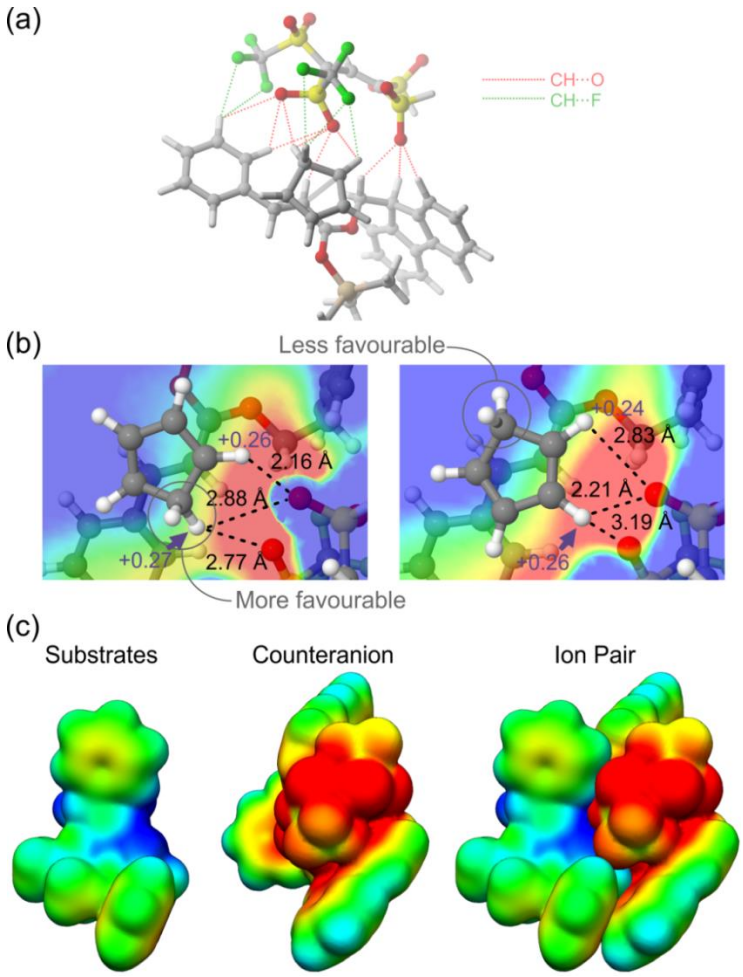

Figure V-2. (a) Electrostatic binding mode of **TS(1′)$_{endo}$** [**TS(2′)$_{endo}$** is very similar]. Interaction distances less than 3 Å are shown. (b) Electrostatic potential (red = -15 kcal mol^{-1}; blue = +15 kcal mol^{-1}) due to the catalyst and dienophile in the plane of key CP hydrogen atoms, along with natural atomic charges for selected H atoms and interaction distances for the CH···O hydrogen bonds in the diastereoselectivity-determining **TS(3)$_{endo}$** and **TS(3)$_{exo}$**. (c) ESPs of the reacting substrates (red = +20 kcal mol^{-1}; blue = +94 kcal mol^{-1}) and catalyst (red = -75 kcal mol^{-1}; blue = -20 kcal mol^{-1}), along with the two ESPs superimposed in the geometry of **TS(3)$_{endo}$**.

In conclusion, we have presented the first computational analysis of silylium ion-ACDC.[75] Results show that in the most favourable TS structure, the ion-pair formed by the silylated cinnamate ester and BALT anion creates a cleft that perfectly accommodates the reacting CP. Stacking interactions preferentially stabilize this TS structure, in which the diene adds to the more hindered face of the dienophile. This, complemented by electrostatic interactions, leads to the preferred enantiomer of the *endo* product. The *endo*:*exo* selectivity, on the other hand, results from the interaction of the cyclopentadiene with the chiral electrostatic environment of the counteranion, which favours the *endo* TS. The requirement of fluorenylmethyl esters for high stereoselectivities can be attributed to stabilizing π-stacking interactions between the fluorenyl group and the 9-phenanthrenyl substituent of the most stereoselective catalyst. Overall, these computational data not only explain the stereoselectivity of these silylium-ion-ACDC Diels-Alder reactions, but should guide the development of more effective ion-pairing asymmetric organocatalysts.

Table V-3. Gas phase difference in energy ($\Delta\Delta E^{\ddagger}$), difference in substrate energy ($\Delta\Delta E_{sub}$), difference in catalyst energy ($\Delta\Delta E_{cat}$), and difference in interaction energy ($\Delta\Delta E_{int}$) between the lowest-lying *endo* and *exo* TSs for Entries 1-4 of Table V-1, in kcal mol^{-1}.

Entry	$\Delta\Delta E^{\ddagger}$	$\Delta\Delta E_{cat}$	$\Delta\Delta E_{sub}$	$\Delta\Delta E_{int}$
1	1.6	0.1	0.5	1.0
2	0.6	2.0	2.7	-4.1
3	2.0	0.6	-0.1	1.4
4	2.4	0.5	-0.1	2.0

CHAPTER VI

CONCLUSIONS

This dissertation highlights the importance of non-covalent interactions in the observed stereoselectivities of several asymmetric organocatalytic reactions. DFT calculations are an invaluable tool in characterizing these interactions as well as other factors that may govern stereoselectivity. Overall, the computed stereoselectivities are in very good agreement with the experimental data, showcasing the power of modern computational quantum chemistry to describe complex organocatalytic reactions. In all the reactions studied here, the origins of stereoselectivity are traced to differences in specific types of non-covalent interactions in the competing transition states. Other contributions, like differential distortion energies, either play a minor role or only become important in cases of less stereoselective catalysts.

First, it has been shown in the first example of an asymmetric catalytic Fischer indolization that CH/π interactions are responsible for the stability of the favored transition state corresponding to the major observed enantiomer product. These effects overshadow π- stacking interactions, which stabilize the transition state corresponding to the minor observed enantiomer. Calculations on catalysts exhibiting lower selectivities show diminished differences in interaction energy between competing transition states, and instead differences in relative distortion energies play a more important role.

Second, it has been shown, through modelling of nine instances of enantioselective chiral phosphoric acid-catalyzed *meso*-epoxide ring openings, that

stereoselectivity is due to a favorable electrostatic CH···O interaction involving a methylene group in the partially opened epoxide ring interacting with a nearby phosphoryl oxygen of the catalyst. This interaction is not present in the disfavored transition state due to restricted orientation of the substrates in the chiral cavity of the catalyst. A general model for the stereoselectivity of this type of reaction is devised on this basis.

Third, it has been shown in a series of enantioselective chiral phosphoric acid-catalyzed 3-substituted oxetane ring openings that differential interaction energies play the dominant role in the selectivities. However, unlike the epoxide ring opening reactions, these differential interaction energies manifest in the form of various non-covalent interactions which are highly dependent on the exact configuration of the catalytic system. In instances of oxetanes that are monosubstituted in the 3-position, CH/π interactions between the mercaptobenzothiazole nucleophile and the aromatic backbone of the catalyst play a critical role in the selectivity, while in 3,3-disubstituted oxetanes, the nature of interactions between the substituents and the catalyst play a more important role, especially if one of the substituents is a hydroxyl group.

Finally, it has been shown in a recent example of asymmetric ion-pairing catalysis of a Diels-Alder reaction that differences in both dispersion and electrostatic-driven interactions are involved in the observed enantioselectivity of the *endo* product. In the preferred transition state of the most stereoselective catalyst, cyclopentadiene unexpectedly adds to the more hindered face of the dienophile due to favorable dispersion-driven interactions with the aromatic binaphthyl backbone of the catalyst.

This is paired with stronger electrostatic-based CH···O interactions between the cationic substrate and anionic catalyst core to produce the observed stereoselectivity. The *endo:exo* selectivity is due to differences in CH···O interactions between cyclopentadiene and the catalyst sulfonate oxygens, similar to those observed for the asymmetric epoxide ring openings. In this case, the CH_2 hydrogens of cyclopentadiene bear a slightly greater positive charge than the hydrogens bound to the sp^2 carbons, and the *endo* transition state is more stabilized than the *exo* transition state by interacting with the catalyst sulfonate oxygens through the CH_2 hydrogens rather than the sp^2 counterparts in the *exo* transition state.

REFERENCES

(1) (a) List, B. *Chem. Rev.* **2007,** *107*, 5413-5415. (b) MacMillan, D. W. C. *Nature* **2008,** *455*, 304-308. (c) Seayad, J.; List, B. *Org. Biomol. Chem.* **2005,** *3*, 719-724.

(2) Parmar, D.; Sugiono, E.; Raja, S.; Rueping, M. *Chem. Rev.* **2014,** *114*, 9047-9153.

(3) (a) Mahlau, M.; Garcia-Garcia, P.; List, B. *Chem. Eur. J* **2012,** *18*, 16283-16287. (b) Mahlau, M.; List, B. *Angew. Chem. Int. Ed.* **2013,** *52*, 518-533. (c) Mayer, S.; List, B. *Angew. Chem. Int. Ed.* **2006,** *45*, 4193-4195.

(4) Calais, J.-L. *Int. J. Quantum Chem.* **1993,** *47*, 101-101.

(5) (a) Knowles, R. R.; Jacobsen, E. N. *Proc. Natl. Acad. Sci. USA* **2010,** *107*, 20678-20685. (b) Wheeler, S. E.; Seguin, T. J.; Guan, Y.; Doney, A. C. *Acc. Chem. Res.* **2016,** *49*, 1061-1069.

(6) Gu, Y.; Kar, T.; Scheiner, S. *J. Am. Chem. Soc.* **1999,** *121*, 9411-9422.

(7) (a) Tsuzuki, S.; Lüthi, H. P. *J. Chem. Phys.* **2001,** *114*, 3949-3957. (b) Cerny, J.; Hobza, P. *Phys Chem Chem Phys* **2005,** *7*, 1624-1626. (c) Johnson, E. R.; Wolkow, R. A.; DiLabio, G. A. *Chem. Phys. Lett.* **2004,** *394*, 334-338.

(8) Grimme, S. *J. Comp. Chem.* **2006,** *27*, 1787-1799.

(9) Chai, J.-D.; Head-Gordon, M. *J. Chem. Phys.* **2008,** *128*, 084106.

(10) Goerigk, L.; Grimme, S. *Phys Chem Chem Phys* **2011,** *13*, 6670-6688.

(11) (a) Grimme, S.; Antony, J.; Ehrlich, S.; Krieg, H. *J. Chem. Phys.* **2010,** *132*, 154104. (b) Goerigk, L.; Kruse, H.; Grimme, S. *ChemPhysChem* **2011,** *12*, 3421-3433.

(12) Zhao, Y.; Truhlar, D. G. *Theor. Chem. Acc.* **2008,** *120*, 215-241.

(13) (a) Peverati, R.; Truhlar, D. G. *J. Phys. Chem. Lett.* **2011,** *2*, 2810-2817. (b) Grimme, S. *WIREs Comput Mol. Sci.* **2011,** *1*, 211-228.

(14) Curtin, D. Y. *Rec. Chem. Prog.* **1954,** *15*, 111−128.

(15) Eyring, H. *J. Chem. Phys.* **1935,** *3*, 107-115.

(16) Schrödinger Release 2016-3: MacroModel, v., Schrödinger, LLC, New York, NY, 2016.

(17) (a) Ess, D. H.; Houk, K. N. *J. Am. Chem. Soc.* **2007,** *129*, 10646-10647. (b) Bickelhaupt, F. M.; van Zeist, W. J. *Org. Biomol. Chem.* **2010,** *8*, 3118-3127.

(18) (a) Akiyama, T. *Chem. Rev.* **2007,** *107*, 5744-5758. (b) Kampen, D.; Reisinger, C. M.; List, B. *Top. Curr. Chem.* **2010,** *291*, 395-456. (c) Tereda, M. *Synthesis* **2010,** 1929-1982.

(19) Müller, S.; Webber, M. J.; List, B. *J. Am. Chem. Soc.* **2011,** *133*, 18534-18437.

(20) (a) Fischer, E.; Jourdan, F. *Ber. Dtsch. Chem. Ges.* **1883,** *16*, 2241-2245. (b) Fischer, E.; Hess, O. *O. Ber. Dtsch. Chem. Ges.* **1884,** *17*, 559-568.

(21) (a) Gribble, G. W. *J. Chem. Soc. , Perkin Trans. 1* **2000,** 1045-1075. (b) Humprey, G. R.; Kuethe, J. T. *Chem. Rev.* **2006,** *106*, 2875-2911.

(22) (a) Xu, F.; Huang, D.; Han, C.; Shen, W.; Lin, X.; Wang, Y. *J. Org. Chem.* **2010,** *75*, 8677-8680. (b) Čorić, I.; Müller, S.; List, B. *J. Am. Chem. Soc.* **2010,** *132*,

17370-17373. (c) Xing, C.-H.; Liao, Y.-X.; Ng, J.; Hu, Q.-S. *J. Org. Chem.* **2011,** *76*, 4125-4131.

(23) Martínez, A.; Webber, M. J.; Müller, S.; List, B. *Angew. Chem. Int. Ed.* **2013,** *52*, 9486-9490.

(24) Kötzner, L.; Martínez, A.; De Fusco, C.; List, B. *Angew. Chem. Int. Ed.* **2014,** *53*, 5202-5205.

(25) (a) Houk, K. N.; Cheong, P. H.-Y. *Nature* **2008,** *455*, 309-313. (b) Krenske, E. H.; Houk, K. N. *Acc. Chem. Res.* **2013,** *46*, 979-989. (c) Uyeda, C.; Jacobsen, E. N. *J. Am. Chem. Soc.* **2011,** *133*, 5062-5075. (d) Holland, M. C.; Paul, S.; Schweizer, W. B.; Bergander, K.; Mück-Lichtenfeld, C.; Lakhdar, S.; Mayr, H.; Gilmour, R. *Angew. Chem. Int. Ed.* **2013,** *52*, 7967-7971. (e) Johnston, R. C.; Cheong, P. H.-Y. *Org. Biomol. Chem.* **2013,** *11*, 5057-5064. (f) Allen, S. E.; Mahatthananchai, J.; Bode, J. W.; Kozlowski, M. C. *J. Am. Chem. Soc.* **2012,** *134*, 12098-12103. (g) Jindal, G.; Sunoj, R. B. *Angew. Chem. Int. Ed.* **2014,** *53*, 4432-4436. (h) Odagi, M.; Furukori, K.; Yamamoto, Y.; Sato, M.; Iida, K.; Yamanaka, M.; Nagasawa, K. *J. Am. Chem. Soc.* **2015,** *137*, 1909-1915.

(26) (a) Lu, T.; Zhu, R.; An, Y.; Wheeler, S. E. *J. Am. Chem. Soc.* **2012,** *134*, 3095-3102. (b) Johnston, C. P.; Kothari, A.; Sergeieva, T.; Okovytyy, S. I.; Jackson, K. E.; Paton, R. S.; Smith, M. D. *Nat. Chem.* **2015,** *7*, 171-177. (c) Carrillo, R.; López-Rodríguez, M.; Martín, V. S.; Martín, T. *Angew. Chem. Int. Ed.* **2009,** *48*, 7803-7808.

(27) Çelebi-Ölçüm, N.; Boal, B. W.; Huters, A. D.; Garg, N. K.; Houk, K. N. *J. Am. Chem. Soc.* **2011,** *133*, 5752-5755.

(28) (a) Li, G.-Q.; Gao, H.; Keene, C.; Devonas, M.; Ess, D. H.; Kürti, L. *J. Am. Chem. Soc.* **2013,** *135*, 7414-7417. (b) Maity, P.; Pemberton, R. P.; Tantillo, D. J.; Tambar, U. K. *J. Am. Chem. Soc.* **2013,** *135*, 16380-16383.

(29) (a) Simón, L.; Goodman, J. M. *J. Am. Chem. Soc.* **2008,** *130*, 8741-8747. (b) Simón, L.; Goodman, J. M. *J. Am. Chem. Soc.* **2009,** *131*, 4070-4077. (c) Simón, L.; Goodman, J. M. *J. Org. Chem.* **2010,** *75*, 589-597. (d) Simón, L.; Goodman, J. M. *J. Org. Chem.* **2011,** *76*, 1775-1788. (e) Grayson, M. N.; Pellegrinet, S. C.; Goodman, J. M. *J. Am. Chem. Soc.* **2012,** *134*, 2716-2722. (f) Overvoorde, L. M.; Grayson, M. N.; Luo, Y.; Goodman, J. M. *J. Org. Chem.* **2015,** *80*, 2634-2640.

(30) Robinson, G. M.; Robinson, R. *J. Chem. Soc. Trans.* **1924,** *125*, 827-840.

(31) Holland, M. C.; Gilmour, R. *Angew. Chem. Int. Ed.* **2015,** *54*, 3862-3871.

(32) (a) Barone, V.; Cossi, M. *J. Phys. Chem. A* **1998,** *102*, 1995-2001. (b) Cossi, M.; Rega, N.; Scalmani, G.; Barone, V. *J. Comp. Chem.* **2003,** *24*, 669-681.

(33) (a) Wheeler, S. E. *Acc. Chem. Res.* **2013,** *46*, 1029-1038. (b) Wheeler, S. E.; Bloom, J. W. G. *J. Phys. Chem. A* **2014,** *118*, 6133-6147.

(34) (a) Meyer, E. A.; Castellano, R. K.; Diederich, F. *Angew. Chem. Int. Ed.* **2003,** *42*, 1210-1250. (b) Salonen, L. M.; Ellermann, M.; Diederich, F. *Angew. Chem. Int. Ed.* **2011,** *50*, 4808-4842. (c) Raju, R. K.; Bloom, J. W. G.; An, Y.; Wheeler, S. E. *ChemPhysChem* **2011,** *12*, 3116-3130. (d) Bloom, J. W. G.; Raju, R. K.; Wheeler, S. E. *J. Chem. Theory and Comput.* **2012,** *8*, 3167-3174. (e) Wheeler,

S. E.; Houk, K. N. *Mol. Phys.* **2009,** *107*, 749-760. (f) Plevin, M. J.; Bryce, D. L.; Boisbouvier, J. *Nat. Chem.* **2010,** *2*, 466-471.

(35) Johnson, E. R.; Keinan, S.; Mori-Sánchez, P.; Contreras-García; Cohen, A. J.; Yang, W. *J. Am. Chem. Soc.* **2010,** *132*, 6498-6506.

(36) Liao, S.; Čorić, I.; Wang, Q.; List, B. *J. Am. Chem. Soc.* **2012,** *134*, 10765-10768.

(37) Warshel, A.; Sharma, P. K.; Kato, M.; Xiang, Y.; Liu, H.; Olsson, M. H. M. *Chem. Rev.* **2006,** *106*, 3210-3235.

(38) Neel, A. J.; Hehn, J. P.; Tripet, P. F.; Toste, F. D. *J. Am. Chem. Soc.* **2013,** *135*, 14044-14047.

(39) (a) Milo, A.; Bess, E. N.; Sigman, M. S. *Nature* **2014,** *507*, 210-214. (b) Milo, A.; Neel, A. J.; Toste, F. D.; Sigman, M. S. *Science* **2015,** *347*, 737-743.

(40) Wang, Z.; Law, W. K.; Sun, J. *Org. Lett.* **2013,** *15*, 5964-5966.

(41) (a) Monaco, M. R.; Prévost, S.; List, B. *Angew. Chem. Int. Ed.* **2014,** *53*, 8142-8145. (b) Monaco, M. R.; Prévost, S.; List, B. *J. Am. Chem. Soc.* **2014,** *136*, 16982-16985.

(42) (a) Jacobsen, E. N. *Acc. Chem. Res.* **2000,** *33*, 421-431. (b) Matsunaga, S. *Comprehensive Chirality* **2012,** *5*, 534-580. (c) Jacobsen, E. N.; Kakiuchi, F.; Konsler, R. G.; Larrow, J. F.; Tokunaga, M. *Tetrahedron Lett.* **1997,** *38*, 773-776. (d) Tokunaga, M.; Larrow, J. F.; Kakiuchi, F.; Jacobsen, E. N. *Science* **1997,** *277*, 936-938. (e) Ready, J. R.; Jacobsen, E. N. *Angew. Chem. Int. Ed.* **2002,** *41*, 1374-1377.

(43) (a) Kolb, H. C.; VanNieuwenhze, M. S.; Sharpless, K. B. *Chem. Rev.* **1994,** *94*, 2483-2547. (b) Schneider, C. *Synthesis* **2006,** 3919-3944.

(44) (a) Grayson, M. N.; Goodman, J. M. *J. Org. Chem.* **2013,** *78*, 8796-8801. (b) Grayson, M. N.; Goodman, J. M. *J. Org. Chem.* **2015,** *80*, 2056-2061.

(45) (a) Kanomata, K.; Toda, Y.; Shibata, Y.; Yamanaka, M.; Tsuzuki, S.; Gridnev, I. D.; Terada, M. *Chem. Sci.* **2014,** *5*, 3515-3523. (b) Calleja, J.; González-Pérez, A. B.; de Lera, A. R.; Álvarez, R.; Fañanás, F. J.; Rodríguez, F. *Chem. Sci.* **2014,** *5*, 996-1007. (c) Seguin, T. J.; Lu, T.; Wheeler, S. E. *Org. Lett.* **2015,** *17*, 3066-3069.

(46) (a) Terada, M.; Soga, K.; Momiyama, N. *Angew. Chem. Int. Ed.* **2008,** *47*, 4122-4125. (b) Terada, M.; Tanaka, H.; Sorimachi, K. *J. Am. Chem. Soc.* **2009,** *131*, 3430-3431. (c) Momiyama, N.; Tabuse, H.; Terada, M. *J. Am. Chem. Soc.* **2009,** *131*, 12882-12883. (d) Čorić, I.; Vellalath, S.; List, B. *J. Am. Chem. Soc.* **2010,** *132*, 8536-8537. (e) Reddy, L. R. *Org. Lett.* **2012,** *14*, 1142-1145. (f) Wang, Q.; Leutzsch, M.; van Gemmeren, M.; List, B. *J. Am. Chem. Soc.* **2013,** *135*, 15334-15337. (g) Grayson, M. N.; Goodman, J. M. *J. Am. Chem. Soc.* **2013,** *135*, 6142-6148. (h) Overvoorde, L. M.; Grayson, M. N.; Luo, L.; Goodman, J. M. *J. Org. Chem.* **2015,** *80*, 2634-2640. (i) Grayson, M. N.; Krische, M. J.; Houk, K. N. *J. Am. Chem. Soc.* **2015,** *137*, 8838-8850. (j) Ajitha, M. J.; Huang, K.-W. *Org. Biomol. Chem.* **2015,** *13*, 10981-10985.

(47) (a) Becke, A. *J. Chem. Phys.* **1997,** *107*, 8554-8560. (b) Weigend, F.; Ahlrichs, R. *Phys Chem Chem Phys* **2005,** *7*, 3297-3305.

(48) (a) Miertus, S.; Scrocco, E.; Tomasi, J. *Chem. Phys.* **1981,** *55*, 117-129. (b) Tomasi, J.; Mennucci, B.; Cammi, R. *Chem. Rev.* **2005,** *105*, 2999-3093.

(49) Grimme, S. *Chem. Eur. J.* **2012,** *18*, 9955-9964.

(50) Reed, A. E.; Weinstock, R. B.; Weinhold, F. *J. Chem. Phys.* **1985,** *83*, 735-746.

(51) *Gaussian 09, Revision D.01, Frisch, M. J.; Trucks, G. W.; Schlegel, H. B.; Scuseria, G. E.; Robb, M. A.; Cheeseman, J. R.; Scalmani, G.; Barone, V.; Mennucci, B.; Petersson, G. A.; Nakatsuji, H.; Caricato, M.; Li, X.; Hratchian, H. P.; Izmaylov, A. F.; Bloino, J.; Zheng, G.; Sonnenberg, J. L.; Hada, M.; Ehara, M.; Toyota, K.; Fukuda, R.; Hasegawa, J.; Ishida, M.; Nakajima, T.; Honda, Y.; Kitao, O.; Nakai, H.; Vreven, T.; Montgomery, Jr., J. A.; Peralta, J. E.; Ogliaro, F.; Bearpark, M.; Heyd, J. J.; Brothers, E.; Kudin, K. N.; Staroverov, V. N.; Kobayashi, R.; Normand, J.; Raghavachari, K.; Rendell, A.; Burant, J. C.; Iyengar, S. S.; Tomasi, J.; Cossi, M.; Rega, N.; Millam, N. J.; Klene, M.; Knox, J. E.; Cross, J. B.; Bakken, V.; Adamo, C.; Jaramillo, J.; Gomperts, R.; Stratmann, R. E.; Yazyev, O.; Austin, A. J.; Cammi, R.; Pomelli, C.; Ochterski, J. W.; Martin, R. L.; Morokuma, K.; Zakrzewski, V. G.; Voth, G. A.; Salvador, P.; Dannenberg, J. J.; Dapprich, S.; Daniels, A. D.; Farkas, Ö.; Foresman, J. B.; Ortiz, J. V.; Cioslowski, J.; Fox, D. J. Gaussian, Inc., Wallingford CT, 2009.*

(52) Johnston, R. C.; Cohen, D. T.; Eichman, C. C.; Scheidt, K. A.; Cheong, P. H.-Y. *Chem. Sci.* **2014,** *5*, 1974-1982.

(53) (a) Corey, E. J.; Lee, T. W. *Chem. Commun.* **2001,** 1321-1329. (b) Corey, E. J. *Angew. Chem. Int. Ed.* **2002,** *41*, 1650-1667. (c) Corey, E. J. *Angew. Chem. Int. Ed.* **2009,** *48*, 2100-2117.

(54) (a) Sepúlveda, D.; Lu, T.; Wheeler, S. E. *Org. Biomol. Chem.* **2014,** *12*. (b) Rooks, B. J.; Haas, M. R.; Sepúlveda, D.; Lu, T.; Wheeler, S. E. *ACS Catal.* **2015,** *5*, 272-280.

(55) (a) Beetham, J. K.; Grant, D.; Arand, M.; Garbarino, J.; Kiosue, T.; Pinot, F.; Oesch, F.; Belknap, W. R.; Shinozaki, K.; Hammock, B. D. *DNA and Cell Biology* **1995,** *14*, 61-71. (b) Newman, J. W.; Morisseau, C.; Hammock, B. D. *Progress in Lipid Research* **2005,** *44*, 1-51. (c) Reetz, M. T.; Torre, C.; Eipper, A.; Lohmer, R.; Hermes, M.; Brunner, B.; Maichele, A.; Bocola, M.; Arand, M.; Cronin, A.; Genzel, Y.; Archelas, A.; Furstoss, R. *Org. Lett.* **2004,** *6*, 177-180. (d) Reetz, M. T.; Bocola, M.; Wang, L.-W.; Sanchis, J.; Cronin, A.; Arand, M.; Zou, J.; Archelas, A.; Bottalla, A. L.; Naworyta, A.; Mowbray, S. L. *J. Am. Chem. Soc.* **2009,** *131*, 7334-7343.

(56) Lind, M. E. S.; Himo, F. *Angew. Chem. Int. Ed.* **2013,** *52*, 4563-4567.

(57) (a) Copeland, G. T.; Miller, S. J. *J. Am. Chem. Soc.* **2001,** *123*, 6495-6502. (b) Kanomata, K.; Toda, Y.; Shibata, Y.; Yamanaka, M.; Tsuzuki, S.; Gridnev, I. D.; Terada, M. *Chem. Sci.* **2014,** *5*, 3515-3523. (c) Meng, S.-S.; Liang, Y.; Cao, K.-S.; Zou, L.; Lin, X.-B.; Yang, H.; Houk, K. N.; Zheng, W.-H. *J. Am. Chem. Soc.* **2014,** *136*, 12249-12252. (d) Jindal, G.; Sunoj, R. B. *Angew. Chem., Int. Ed.*

Engl. **2014,** *53*, 4432-4436. (e) Lu, T.; Wheeler, S. E. *Science* **2015,** *347*, 719-720. (f) Seguin, T. J.; Lu, T.; Wheeler, S. E. *Org. Lett.* **2015,** *17*, 3066-3069.

(58) Wang, Z.; Chen, Z.; Sun, J. *Angew. Chem. Int. Ed.* **2013,** *52*, 6685-6688.

(59) (a) Quasdorf, K. W.; Overman, L. E. *Nature* **2014,** *516*, 181-191. (b) Christoffers, J.; Mann, A. *Angew. Chem. Int. Ed.* **2001,** *40*, 4591-4597. (c) Douglas, C. J.; Overman, L. E. *Proc. Natl. Acad. Sci. U.S.A.* **2004,** *101*, 5363-5367.

(60) (a) Akiyama, T.; Itoh, J.; Fuchibe. *Adv. Synth. Catal.* **2006,** *348*, 999-1010. (b) Connon, S. J. *Angew. Chem. Int. Ed.* **2006,** *45*, 3909-3912. (c) Terada, M. *Chem. Commun.* **2008,** 4097-4112. (d) Terada, M. *Bull. Chem. Soc. Jpn.* **2010,** *83*, 101-119. (e) Terada, M. *Synthesis* **2010,** 1929-1982. (f) Zamfir, A.; Schenker, S.; Freund, M.; Tsogoeva, S. B. *Org. Biomol. Chem.* **2010,** *8*, 5262-5276. (g) Schenker, S.; Zamfir, A.; Freund, M.; Tsogoeva, S. B. *Eur. J. Org. Chem.* **2011,** 2209. (h) Parmar, D.; Sugiono, E.; Raja, S.; Rueping, M. *Chem. Rev.* **2014,** *114*, 9047-9153. (i) Terada, M. *Curr Org Chem* **2011,** *15*, 2227-2256. (j) Adair, G.; Mukherjee, S.; List, B. *Aldrichimica Acta* **2008,** *42*, 31-39. (k) You, S.-L.; Cai, Q.; Zeng, M. *Chem. Soc. Rev.* **2009,** *38*, 2190-2201. (l) Yu, J.; Shi, F.; Gong, L.-Z. *Acc. Chem. Res.* **2011,** *44*, 1156-1171. (m) Rueping, M.; Kuenkel, A.; Atodiresei, I. *Chem. Soc. Rev.* **2011,** *40*, 4539-4549.

(61) (a) Wang, Z.; Chen, Z.; Sun, J. *Org. Biomol. Chem.* **2014,** *12*, 6028-6032. (b) Yang, W.; Wang, Z.; Sun, J. *Angew. Chem. Int. Ed.* **2016,** *55*, 6954-6958. (c) Yang, W.; Sun, J. *Angew. Chem. Int. Ed.* **2016,** *55*, 1868-1871.

(62) (a) Marcelli, T.; Hammar, P.; Himo, F. *Chem. Eur. J.* **2008,** *14*, 8562-8571. (b) Simón, L.; Goodman, J. M. *J. Am. Chem. Soc.* **2008,** *130*, 8741-8747. (c) Reid, J. P.; Simón, L.; Goodman, J. M. *Acc. Chem. Res.* **2016,** *49*, 1029-1041.

(63) Wheeler, S. E.; Seguin, T. J.; Guan, Y.; Doney, A. C. *Acc. Chem. Res.* **2016,** *49*, 1061-1069.

(64) Wang, H.; Jain, P.; Antilla, J. C.; Houk, K. N. *J. Org. Chem.* **2013,** *78*, 1208-1215.

(65) Seguin, T. J.; Wheeler, S. E. *ACS Catal.* **2016,** *6*, 2681-2688.

(66) Birman, V. B.; Rheingold, A. L.; Lam, K.-C. *Tetrahedron: Asymmetry* **1999,** *10*, 125-131.

(67) (a) Cai, D.; Hughes, D. L.; Verhoeven, T. R.; Reider, P. J. *Tetrahedron Lett.* **1995,** *36*, 7991-7994. (b) Chen, Y.; Yekta, S.; Yudin, A. K. *Chem. REv.* **2003,** *103*, 3155-3211. (c) Shibasaki, M.; Matsunaga, S. *Chem. Soc. Rev.* **2006,** *35*, 269-279.

(68) Marenich, A. V.; Cramer, C. J.; Truhlar, D. G. *J. Phys. Chem. B* **2009,** *113*, 6378-6396.

(69) Grimme, S. *Chem.--Eur. J.* **2012,** *18*, 9955-9964.

(70) Legault, C. Y. *CYLview, 1.0b*, Université de Sherbrooke: 2009.

(71) (a) Jindal, G.; Sunoj, R. B. *Angew. Chem. Int. Ed.* **2014,** *53*, 4432-4436. (b) Liu, C.; Besora, M.; Maseras, F. *Chem Asian J* **2016,** *11*, 411-416. (c) Simon, L.; Paton, R. S. *Org. Biomol. Chem.* **2016,** *14*, 3031-3039. (d) Rodríguez, E.;

Grayson, M. N.; Asensio, A.; Barrio, P.; Houk, K. N.; Fustero, S. *ACS Catal.* **2016,** *6*, 2506-2514.

(72) Mahlau, M.; List, B. *Angew. Chem. Int. Ed.* **2013,** *52*, 518-533.

(73) (a) Hamilton, G. L.; Kang, E. J.; Mba, M.; Toste, F. D. *Science* **2007,** *317*, 496-499. (b) Hamilton, G. L.; Kanai, T.; Toste, F. D. *J. Am. Chem. Soc.* **2008,** *130*, 14984-14986. (c) García-García, P.; Lay, F.; García-García, P.; Rabalakos, C.; List, B. *Angew. Chem. Int. Ed.* **2009,** *48*, 4363-4366. (d) Rauniyar, V.; Lackner, A. D.; Hamilton, G. L.; Toste, F. D. *Science* **2011,** *334*, 1681-1684. (e) Jiang, G.; List, B. *Angew. Chem. Int. Ed.* **2011,** *50*, 9471-9474. (f) Phipps, R. J.; Hamilton, G. L.; Toste, F. D. *Nat. Chem.* **2012,** *4*, 603-614. (g) Brak, K.; Jacobsen, E. N. *Angew. Chem. Int. Ed.* **2013,** *52*, 534-561. (h) Neel, A. J.; Hehn, J. P.; Tripet, P. F.; Toste, F. D. *J. Am. Chem. Soc.* **2013,** *135*, 14044-14047. (i) Chen, W.; Hartwig, J. F. *J. Am. Chem. Soc.* **2013,** *135*, 2068-2071. (j) Wang, Q.; Leutzsch, M.; van Gemmeren, M.; List, B. *J. Am. Chem. Soc.* **2013,** *135*, 15334-15337. (k) Yang, X.; Phipps, R. J.; Toste, F. D. *J. Am. Chem. Soc.* **2014,** *136*, 5225-5228. (l) Wang, P.-S.; Lin, H.-C.; Zhai, Y.-J.; Han, Z.-Y.; Gong, L.-Z. *Angew. Chem.* **2014,** *126*, 12414-12417. (m) Zhang, Z.; Bae, H. Y.; Guin, J.; Rabalakos, C.; van Gemmeren, M.; Leutzsch, M.; Klussmann, M.; List, B. *Nat. Commun.* **2016,** *7*. (n) Hiramatsu, K.; Honjo, T.; Rauniyar, V.; Toste, F. D. *ACS Catal.* **2016,** *6*, 151-154.

(74) (a) Cheong, P. H.-Y.; Legault, C. Y.; Um, J. M.; Çelebi-Olçüm, N.; Houk, K. N. *Chem. Rev.* **2011,** *111*, 5042–5137. (b) Sunoj, R. B. *Acc. Chem. Res.* **2016,** *49*,

1019-1028. (c) Walden, D. M.; Ogba, O. M.; Johnston, R. C.; Cheong, P. H.-Y. *Acc. Chem. Res.* **2016,** *49*, 1279-1291. (d) Lam, Y.; Grayson, M. N.; Holland, M. C.; Simon, A.; Houk, K. N. *Acc. Chem. Res.* **2016,** *49*, 750-762. (e) Halskov, K. S.; Donslund, B. S.; Paz, B. M.; Jørgensen, K. A. *Acc. Chem. Res.* **2016,** *49*, 974-986. (f) Peng, Q.; Paton, R. S. *Acc. Chem. Res.* **2016,** *49*, 1042-1051.

(75) Gatzenmeier, T.; van Gemmeren, M.; Xie, Y.; Höfler, D.; Leutzsch, M.; List, B. *Science* **2016,** *351*, 949-952.

(76) Mathieu, B.; de Fays, L.; Ghosez, L. *Tetrahedron Lett.* **2000,** *41*, 9561-9564.

(77) Connon, S. J. *Angew. Chem. Int. Ed.* **2006,** *45*, 3909-3912.

(78) Wheeler, S. E.; Houk, K. N. *J. Chem. Theory Comput.* **2010,** *6*, 395-404.

(79) Grimme, S. *Chemistry – A European Journal* **2012,** *18*, 9955-9964.

(80) Wagner, J. P.; Schreiner, P. R. *Angew. Chem. Int. Ed.* **2015,** *54*, 12274-12296.

(81) (a) Seguin, T. J.; Wheeler, S. E. *ACS Catal.* **2016,** *6*, 2681-2688. (b) Doney, A. C.; Rooks, B. R.; Lu, T.; Wheeler, S. E. *ACS Catal.* **2016,** *Just Accepted Manuscript, DOI: 10.1021/acscatal.6b02366*.

APPENDIX A

Performance of wB97X-D/6-311+G(d,p)//wB97X-D/6-31G(d) for Acid-catalyzed Fischer Indole Reactions

Houk and co-workers recently presented gas-phase reaction barriers and thermochemistry for a model acid-catalyzed Fischer indole reaction, including high-accuracy CBS-QB3 data (*J. Am. Chem. Soc.* **2011**, 133, 5752–5755). Below are CBS-QB3 free energy barriers for the rate-limiting [3,3]-sigmatropic rearrangement, along with predicted barriers from various methods tested by Houk. Also included are predictions using wB97X-D/6-31G(d) and wB97X-D/6-311G+(d,p)//wB97X-D/6-31G(d). wB97X-D/6-311G+(d,p)//wB97X-D/6-31G(d) provides much more accurate barrier heights, compared to CBS-QB3, than the other DFT methods. The results are comparable to those provided by SCS-MP2. Based on this, as well as the well-established ability of wB97X-D to capture non-covalent interactions, we expect this approach to perform well for the asymmetric catalytic Fischer indolizations examined in this work.

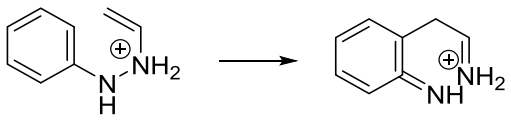

Figure A-1. Model system for comparison of computed [3,3]-sigmatropic rearrangement free energy barriers.

Table A-1. Predicted free energy barriers ($\Delta G^{\ddagger}$) for the acid-promoted [3,3]-sigmatropic rearrangement depicted above, as well as errors relative to CBS-QB3 (kcal/mol).

Method	**$\Delta G^{\ddagger}$**	**Error**
CBS-QB3	10.1	
B3LYP/cbsb7	3.6	-6.5
B3LYP/6-31G(d)	5.0	-5.1
MP2/6-31G(d)	8.7	-1.4
SCS-MP2/6-31G(d)	12.1	2.0
M06-2X/6-31G(d)	14.7	4.6
wB97XD/6-31G(d)	12.3	2.2
wB97XD/6-311+G(d,p)// wB97XD/6-31G(d)	12.4	2.3

Quantifying Non-covalent Interactions in TS(*S*) and TS(*R*) for Catalyst 1a

The gas-phase energy of TS(*R*), relative to TS(*S*), $\Delta\Delta E^{\ddagger}$, was decomposed as follows:

$$\Delta\Delta E^{\ddagger} = \Delta\Delta E_{sub} + \Delta\Delta E_{cat} + \Delta\Delta E_{int}$$

where $\Delta\Delta E_{sub}$ is the difference in energy between the protonated ene-hydrazine substrate in the TS(*R*) and TS(*S*) geometries; $\Delta\Delta E_{cat}$ is the difference in energy between the catalyst geometries in these two TS structures; and $\Delta\Delta E_{int}$ is the difference in interaction energies between the catalyst and substrate in the TS(*R*) and TS(*S*) geometries. In the latter case, the interaction energy is calculated as the difference in energy between the catalyst-substrate complex and separated species at the TS geometry.

This interaction energy was approximately decomposed into contributions from interactions of the substrate with different fragments of the catalyst as follows. For both TS(*S*) and TS(*R*), we considered the interaction of the substrate with three three main

components of the catalyst: the phosphoric acid "core", and the two 9-anthracenyl groups. This was accomplished by severing the highlighted bonds to generate three separate dimers, as demonstrated here for TS(S):

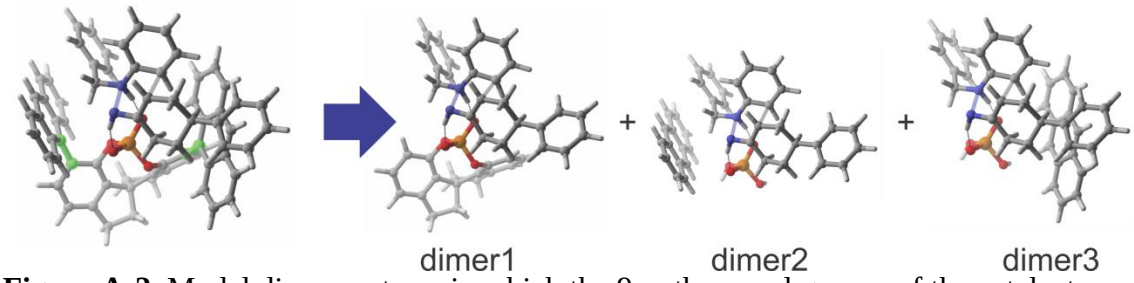

Figure A-2. Model dimer systems in which the 9-anthracenyl groups of the catalyst are removed (dimer 1) or the SPINOL backbone and one of the 9-anthracenyl groups are removed (dimers 2 and 3).

In the case of dimer2 and dimer3, the phosphoric acid functionality remains hydrogen bonded to the substrate to account for the partial sharing of the proton. In all three dimers, any open valences resulting from the severed bonds were replaced with hydrogens and the positions of these hydrogens optimized with the remainder of the atoms fixed in space.

We then evaluated the interaction energy for each complex as the difference in energy of the dimer and the separated monomers, all at fixed geometries and at the wB97X-D/6-311+G(d,p)//wB97X-D/6-31G(d) level of theory (gas-phase).

The resulting interaction energies (kcal mol^{-1}) were as follows for $TS_{1a}(S)$ and $TS_{1a}(R)$:

Table A-2. Absolute and relative interaction energies for model dimers 1-3 for $TS_{1a}(S)$ and $TS_{1a}(R)$.

	dimer1	dimer2	dimer3
$TS_{1a}(S)$	-107.1	-9.8	-15.7
$TS_{1a}(R)$	-104.5	-12.3	-10.8
difference	2.6	-2.4	5.0

Energies in kcal/mol

Qualitatively, the interaction energy in dimer 1 corresponds to the hydrogen bonding interactions of the substrate with the catalyst, dimer 2 the π-stacking interaction of the substrate with one of the 9-anthracenyl groups of the catalyst, and dimer 3 the CH/π interactions between substrate and "other" 9-anthracenyl group. The differences in these values are reported in Figure II-1 of Chapter II.

The interaction energies are quite large, particularly for dimer1, due to the fact that this is an ion pair. Moreover, the sum of these differences (3.4 kcal mol^{-1}) is quite different than the 5.5 kcal mol^{-1} difference in interaction energy for the intact system. As noted in Chapter II, this indicates a large amount of cooperativity among the interactions in this system. This, in turn, likely arises because there is substantial charge delocalization between the protonated substrate and the deprotonated phosphoric acid in the intact complex (ie: there is partial sharing of the proton). This delocalization is clearly missing in dimers2 and 3. Regardless, this decomposition should provide at least a qualitative guide to the impact of CH/π and π-stacking interactions on the enantioselectivity of this reaction.

We also explored models in which the phosphoric acid is neglected in dimer2 and dimer3. This makes no difference on the interaction energy difference for dimer3, but changes the interaction energies for dimer2 slightly:

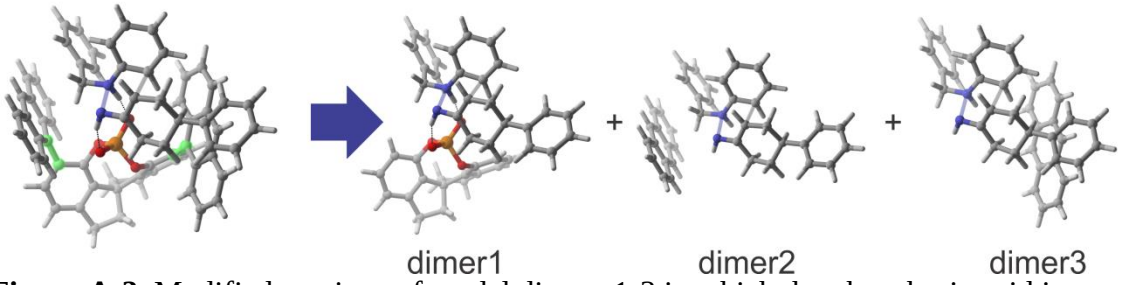

Figure A-3. Modified versions of model dimers 1-3 in which the phosphoric acid is neglected in dimers 2 and 3.

Table A-3. Absolute and relative interaction energies for model dimers 1-3, where the phosphoric acid is neglected in dimers 2 and 3, for $TS_{1a}(S)$ and $TS_{1a}(R)$.

	dimer1	dimer2	dimer3
$TS_{1a}(S)$	-107.1	-14.9	-20.0
$TS_{1a}(R)$	-104.5	-16.1	-14.7
difference	2.6	-1.2	5.3

Energies in kcal/mol

NCI Analyses of TS(S) and TS(R)

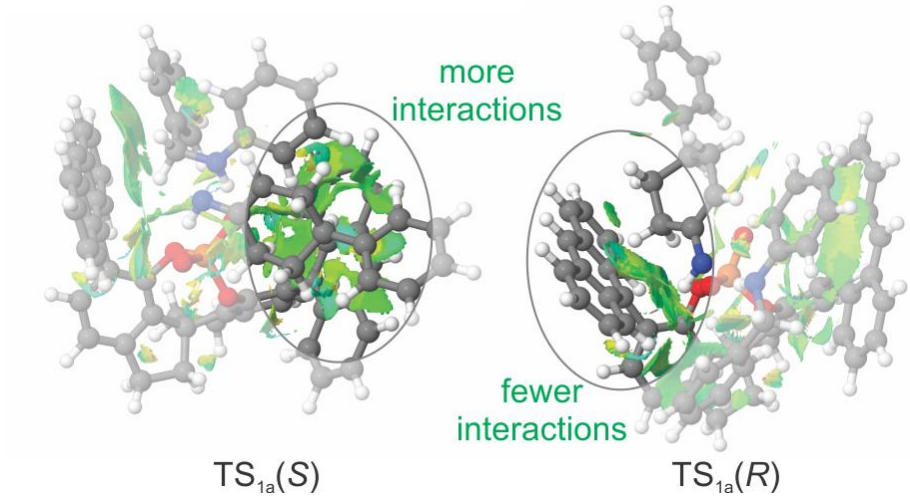

Figure A-4. NCI analyses for $TS_{1a}(S)$ and $TS_{1a}(R)$, showing the more extensive dispersion-like interactions operative in $TS_{1a}(S)$.

Substrate Conformations

One of the major differneces between the substrate conformations in $TS_{1a}(S)$ and $TS_{1a}(R)$. In particular, in TS(*S*), the benzyl group adopts a *gauche* conformation, whereas it is in an anti configration in TS(*R*). These conformations are shown in the figures below more clearly. For each TS, the image on the right is a Newman projection along the C-N bond of the benzyl group.

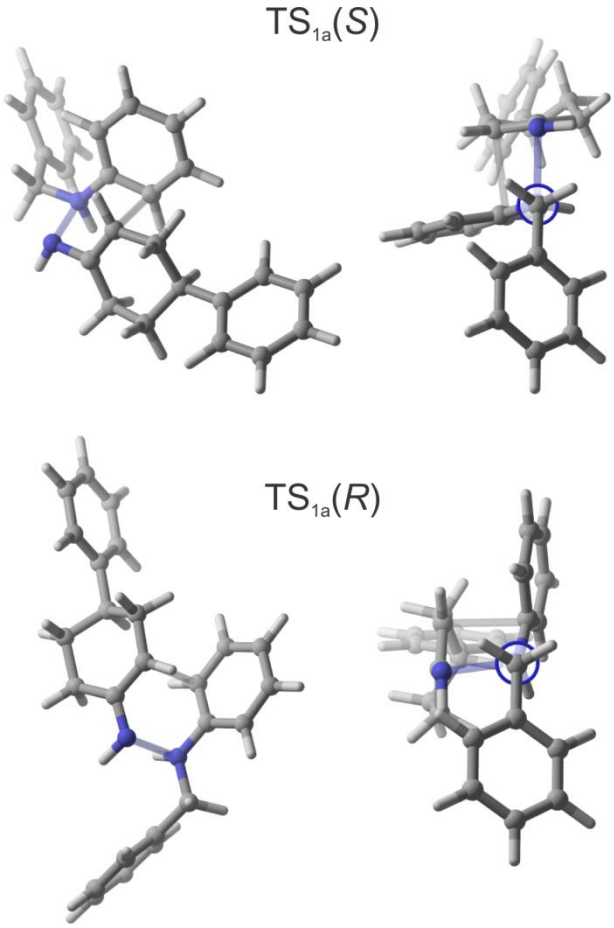

Figure A-5. Newman projections of $TS_{1a}(S)$ and $TS_{1a}(R)$.

TS Structures for Catalysts 1b, 1c, 2b, and 2c

Low-lying TS structures for catalysts **1b**, **1c**, **2b**, and **2c** are depicted below. The TS structures for **2c** are the only ones that are both structurally similar to those for **1a.**

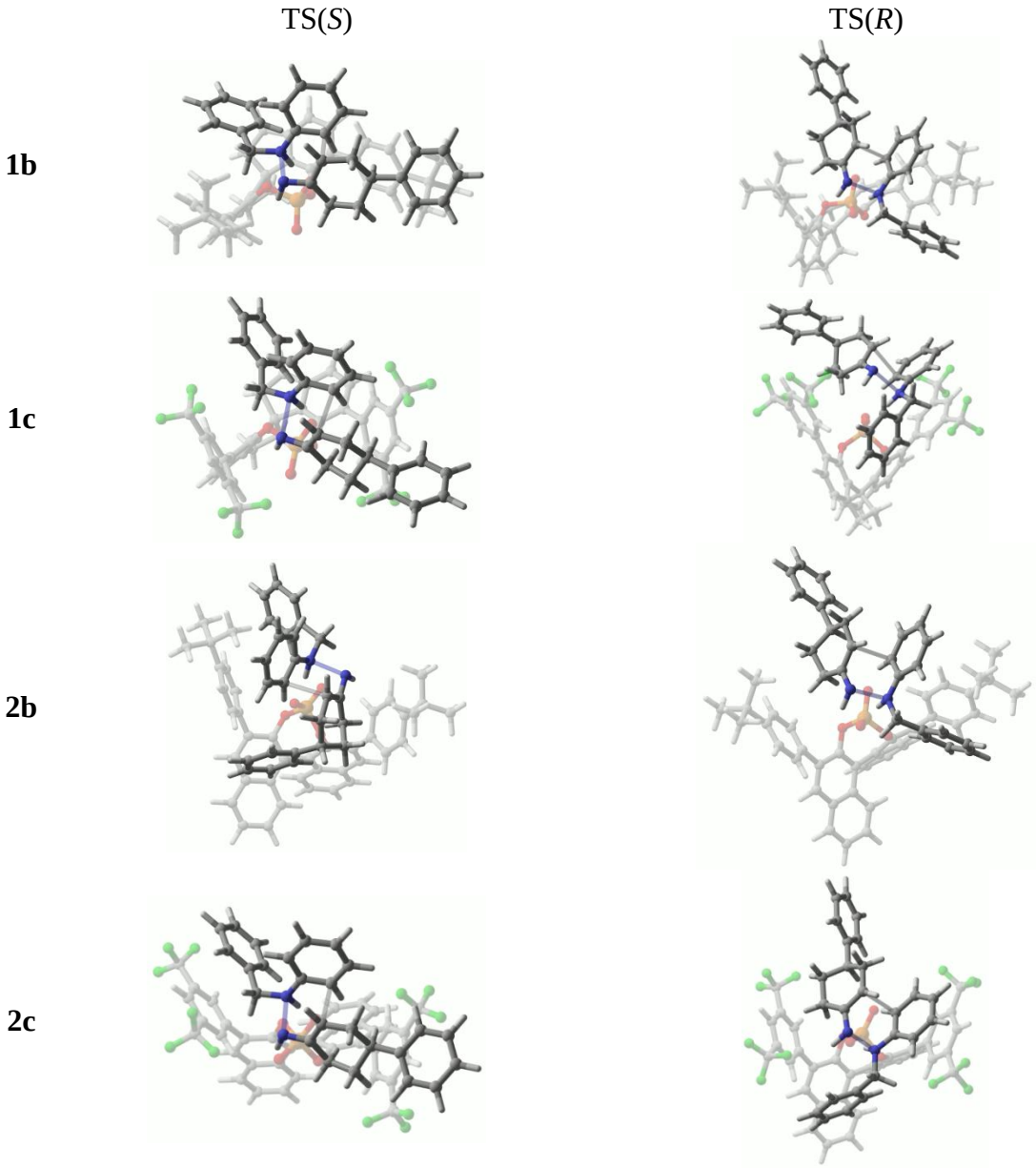

Figure A-6. Low-lying TS structures for catalysts **1b**, **1c**, **2b**, and **2c**.

APPENDIX B

Conformational Searches for Lowest-lying Transition States

For each reaction/catalyst combination, we considered all reasonable conformations in order to identify the lowest-lying (R,R) and (S,S) transition states. First, for each of the catalysts there are a number of conformational possibilities. For instance, **PA-2** exhibits in different conformations depending on whether the hydrogenated aromatic rings on the BINOL scaffold exist in either a twisted or boat-like conformation. There are two possible twisted and two possible boat conformations for each ring, resulting in 16 total possible **PA-2** conformations. For **PA-1A**, a number of conformations arise from rotations of the sigma bond to the three isopropyl groups. In general, we found that the 2- and 6-isopropyl groups favor rotamers in which the C-C-C-H dihedral angle from the 1-position of the phenyl ring to the hydrogen bound to the secondary carbon of the isopropyl group is close to zero. The orientation of the 4-isopropyl group varied for each transition state, and we present results for the lowest-energy conformer located in each case.

Similarly, the 5-OMe substituent of the nucleophile in equation 3.1 can exist in two conformations, both of which were considered for each transition state for each catalyst.

Finally, there are a number of ways of orientating the nucleophile and electrophile within the binding site of the catalyst. That is, in addition to the most favorable orientation depicted in Figure III-2 of Chapter III, additional TS(S,S)

configurations were considered in which the substrates were rotated 90 degrees to take advantage of the same electrostatic stabilization discussed in the paper. However, these orientations were always less favorable.

Comparison of Predicted er Values from Different DFT Methods

Data presented in Chapter III were computed at the B97-D3/def2-TZVP//PCM-B97-D/def2-TZVP level of theory using quasi-RRHO free energy corrections. However, for comparisons, we also predicted er values for the reaction/catalyst combinations for which experimental data are available using wB97X-D/6-311+G(d,p)//wB97X-D/6-31G(d) and M06-2X/6-311+G(d,p)//M06-2X/6-31G(d) using both RRHO and quasi-RRHO free energy corrections. The corresponding data is listed below, where "B97D" denotes B97-D3/def2-TZVP//PCM-B97-D/def2-TZVP, "wB97XD" denotes wB97X-D/6-311+G(d,p)//wB97X-D/6-31G(d), and "M06-2X" denotes M06-2X/6-311+G(d,p)//M06-2X/6-31G(d). All computations used PCM to account for solvent effects.

Table B-1. Comparison of predicted vs experimental er values for 6 reaction/catalyst combinations using B97D, wB97XD, and M06-2X paired with either RRHO or quasi-RRHO based thermochemical corrections.

Eq	Cat	*er* (Exp)	*er* (B97D)	*er* (wB97XD)	*er* (M06-2X)
RRHO (298.15K)					
1	1a	80.5:19.5	94.5:5.5	95.5:4.5	81.4:18.6
1	1b	54.5:45.5	22.8:77.2	92.5:7.5	25.3:74.7
2a	1a	78.5:21.5	35.5:64.5	74.4:25.6	78.1:21.9
2a	2	91.5:8.5	97.9:2.1	90.9:9.1	79.3:20.7
2b	1a	80.5:19.5	64:36	66.8:33.2	23.3:76.7
2b	2	90.0:10.0	94.7:5.3	95:5	93.1:6.9
Quasi-RRHO (298.15K)					
1	1a	80.5:19.5	84.1:15.9	92.9:7.1	80.8:19.2
1	1b	54.5:45.5	36.4:63.6	89.6:10.4	40.8:59.2
2a	1a	78.5:21.5	70.6:29.4	82.7:17.3	77:23
2a	2	91.5:8.5	94.5:5.5	93:7	83.1:16.9
2b	1a	80.5:19.5	80.8:19.2	65.4:34.6	26:74
2b	2	90.0:10.0	91.4:8.6	93:7	91.7:8.3

Exploration of Impact of CH···O Interaction on Barrier Height Differences

The CH···O distance is consistently shorter in TS(R,R) than in TS(S,S) for all reaction/catalyst combinations studied, suggesting that this CH···O interaction is responsible for the preferential stabilization of TS(R,R) over TS(S,S). To find out whether this CH···O interaction is the cause of the energy difference, or simply a common effect of other causes, we examined H_3PO_4 as a model catalyst for equation 3.1. This simple model catalyst results in a free energy difference between TS(S,S) and TS(R,R) of 0.6 kcal mol^{-1}. Moreover, the CH···O distance is 0.13 Å longer in TS(S,S) than in TS(R,R), consistent with the distance difference for the real catalysts (see Figure III-4b in Chapter III). However, re-optimization of TS(S,S) with the CH···O distance constrained to match that in TS(R,R) results in *a* slight increase in relative free energy.

Apparently, the difference in CH···O distances do not cause the preferential stabilization of TS(R,R) over TS(S,S), but instead reflect other differences between these two TS structures. As noted in Chapter III, we attribute this difference to the different electrostatic environments of the two CH groups of the epoxide.

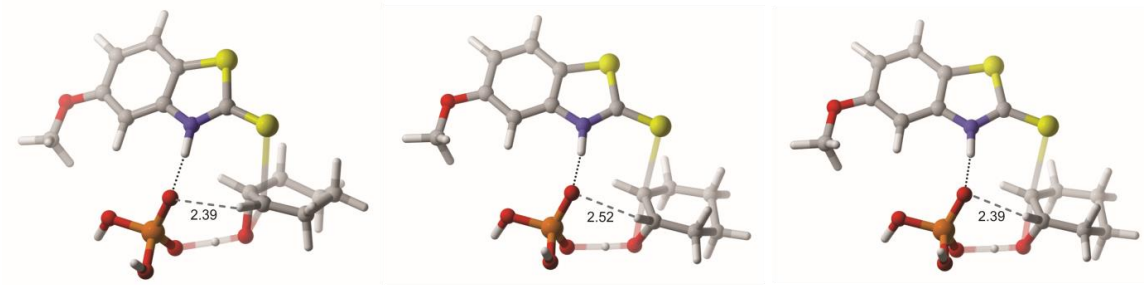

Figure B-1. Computed TS structures for H_3PO_4 as a model catalyst for equation 3.1. In the rightmost structure, the CH···O distance in TS(S,S) is constrained to match that in TS(R,R). Relative free energies are provided in kcal mol–1; CH···O distances are provide in Angstroms.

APPENDIX C

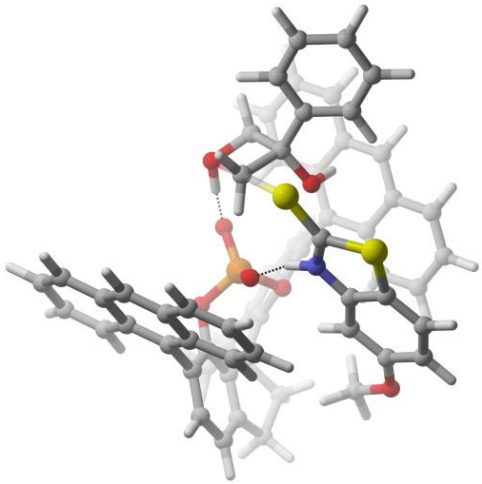

Figure C-1. TS5″, in which the R1 OH group is engaged in an OH···π interaction rather than the weak OH···O hydrogen bond found in TS5′.

Transition State Conformation Searches

Conformational searches were based on structures where the mercaptobenzothiazole nucleophile and protonated oxetane were hydrogen bonded to separate oxygens of the phosphoric acid functionality of the catalyst. To find all reasonable structures, it was born in mind that for every positioning of the oxetane on the catalyst, the nucleophile could attack either of the two electrophilic carbons of the oxetane and there were two possible configurations of the substituents at the 3- position of the oxetane, and the chirality of the product depended on both of these considerations.

For Entries 4 and 5, we considered three rotamers of the hydroxyl group at R_1. Similarly, for Entry 5 we considered two rotamers of the 5-OMe group attached to the nucleophile.

APPENDIX D

Theoretical Methods

Low-lying conformations of the stereocontrolling TS structures were identified using a combination of molecular mechanics (MM) and DFT optimizations. First, MacroModel was used to generate 300-500 unique conformations (using a 0.3 Å cutoff based on RMSD and the OPLS_2005 force field) for each enantiomer of the *endo* product for all four entries of Table V-1. For these conformation searches, the maximum number of steps was set to 1000. This search was repeated several times using different starting geometries, generating 1000s of possible conformations of the Diels-Alder cycloadducts (since these searches were performed independently, with RMSD checks only performed within each search, many conformers were likely redundant. This prevents us from providing a concrete value for the number of conformers considered at this stage of the search process).

The forming C-C bonds in these adducts were lengthened and the resulting structures optimized to the corresponding TS structures using DFT. Initially, ωB97X-D/3-21G geometry optimizations were used to eliminate very unfavorable conformations, and the remaining structures were optimized at the B97-D/6-31G(d) level of theory. This led to the identification of one structure [**TS(3′)$_{endo}$** in Chapter V] that was particularly favourable. Based on this and other low-lying structures, we optimized additional, analogous structures at the B97-D/6-31G(d) level of theory, resulting in 337 total unique structures (spread across both enantiomers of the endo product across all

four entries). Several of the lowest-lying structures from this set were re-optimized at the M06-2X/6-31G(d) level of theory to determine the stereocontrolling TS structures for all four entries of Table V-1.

To probe the suitability of M06-2X to describe these TS structures, including the sundry non-covalent interactions that are operative, we computed single point energies at a number of levels of theory, including those with –D3 dispersion corrections that should exhibit the proper asymptotic behavior.

As seen in the table below, all of these methods lead to similar *er* and *dr* values. Ultimately, we focus on the M06-2X results in Chapter V due to the slightly better agreement with experimental *er* values for Entries 1 and 2.

Table D-1. Computed $\Delta\Delta G^{\ddagger}$ for entries 1-4 of Table V-1 for PCM-"X"/6-311G(d,p)//PCM-M06-2X/6-31G(d), where "X" is the DFT functional given.

Entry	*er*				*dr*			
	wB97X-D	B3LYP-D3	M06-2X-D3	M06-2X	wB97X-D	B3LYP-D3	M06-2X-D3	M06-2X
1	0.9	0.8	0.3	0.3	1.6	0.0	1.6	1.6
2	1.5	-0.7	0.8	-0.2	3.1	1.6	2.3	2.8
3	4.5	3.7	4.8	4.5	2.4	1.2	2.5	2.4
4	5.2	4.5	5.5	5.5	2.6	1.4	2.9	2.7

To assess the impact of different continuum solvent models, we also computed single point energies at the SMD-M06-2X/6-311G(d,p) and SMD-M06-2X-D3/6-311G(d,p) levels of theory. This resulted in modest changes in computed relative free energies compared to the PCM data presented in Chapter V.

Table D-2. Computed $\Delta\Delta G^{\ddagger}$ for entries 1-4 of Table V-1 for "X"/6-311G(d,p)//PCM-M06-2X/6-31G(d), where "X" is the DFT functional given.

Entry	*er*			*dr*		
	SMD-M06-2X	SMD-M06-2X-D3	PCM-M06-2X	SMD-M06-2X	SMD-M06-2X-D3	PCM-M06-2X
1	0.9	0.9	0.3	1.9	1.9	1.6
2	-1.1	-0.2	-0.2	4.0	2.8	2.3
3	3.6	3.9	4.5	2.6	2.7	2.5
4	4.9	5.1	5.5	3.1	3.2	2.9

Finally, to assess the importance of polarization functions on hydrogens on the TS geometries and corresponding relative free energies, we optimized **TS(3)$_{\mathbf{endo}}$** and **TS(3′)endo** at the PCM-M06-2X/6-31G(d,p) level of theory. The corresponding difference in free energy (4.6 kcal/mol) was essentially unchanged compared to the data from PCM-M06-2X/6-31G(d) level of theory (4.5 kcal/mol).

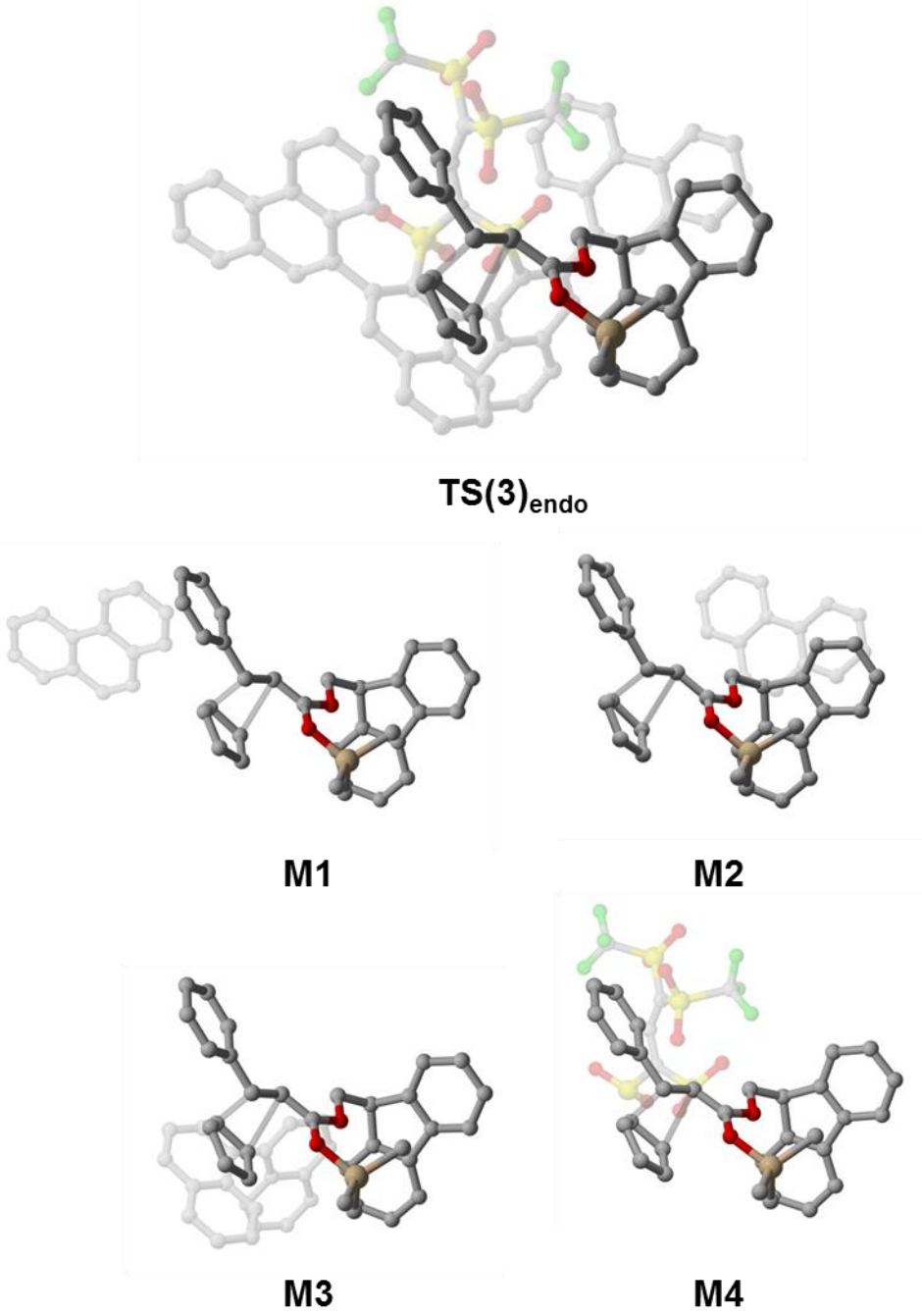

Figure D-1. Truncated models M1-M4, used to quantify the impact of various non-covalent interactions on $\Delta\Delta E_{int}$.

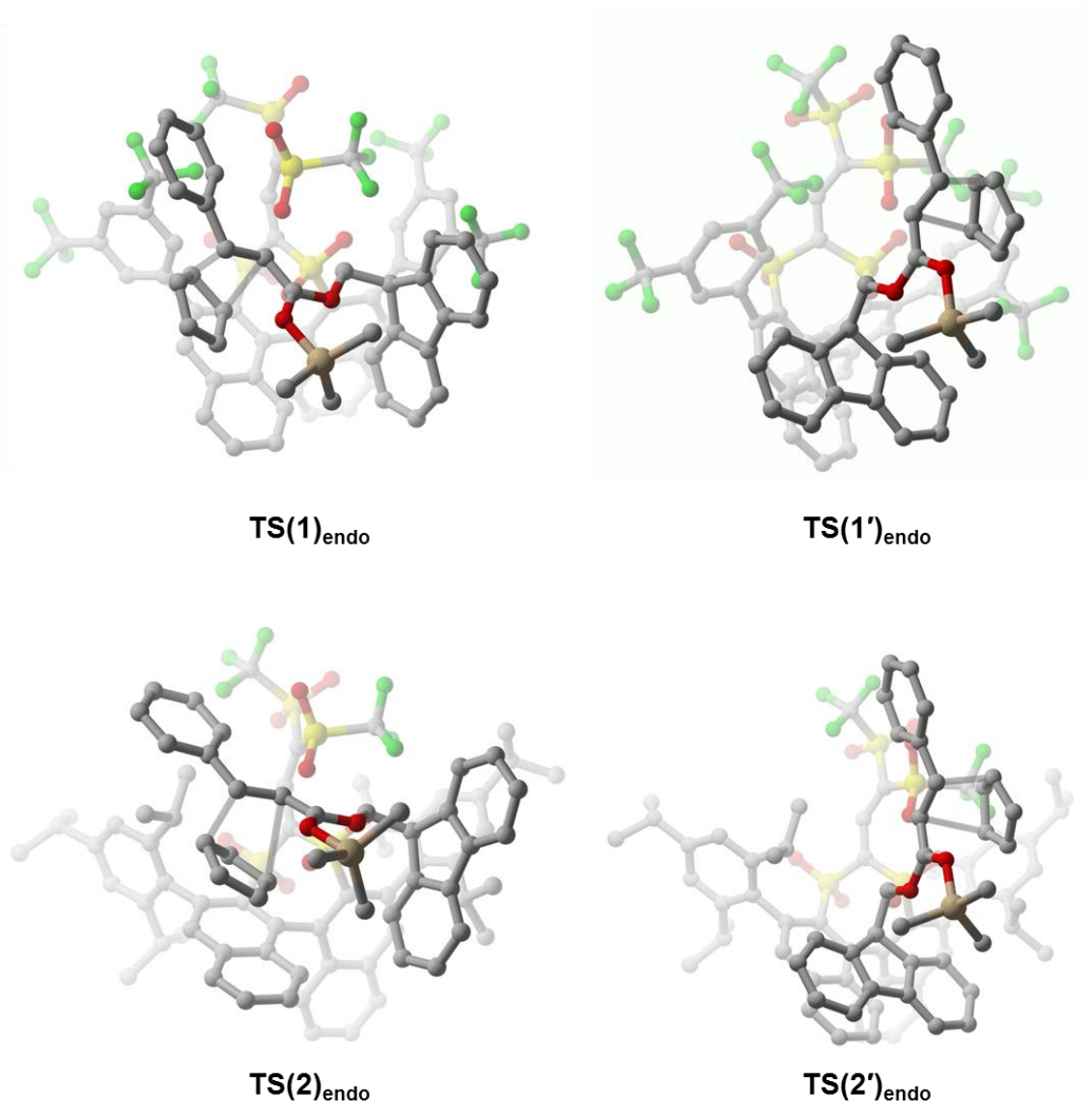

Figure D-2. Computed low-lying *endo* TS structures for Entries 1-2 of Table V-1. Hydrogens are omitted for clarity.

Origin of Enantioselectivity

Table D-3. Gas phase difference in interaction energy for models M1-M4 for the lowest-lying *endo* TSs of Entries 1-4, in kcal mol^{-1}.

Entry	$\Delta\Delta E_{int}$(M1)	$\Delta\Delta E_{int}$(M2)	$\Delta\Delta E_{int}$(M3)	$\Delta\Delta E_{int}$(M4)
1	-5.6	-0.8	-1.9	2.3
2	3.1	2.7	0.3	2.5
3	-0.9	0.1	4.8	2.9
4	-0.9	0.0	4.6	2.9

The importance of dispersion-driven stacking interactions between CP and the catalyst in the enantioselectivity for Entries 3 and 4 can be seen from the value of $\Delta\Delta E_{int}$(M3), which captures differences in non-covalent interactions between the CP and BINOL backbond of the catalyst. To further quantify the impact of different effects on this energy difference, SAPT0/jun-cc-pVDZ energies were computed, which decompose this energy difference into contributions from electrostatic interactions (Elec), exchange-repulsions (Exch), induction (Ind), and dispersion (Disp), as shown in Table S2. For Entries 3 and 4, the largest favourable contribution is from dispersion interactions, as is typical for stacking interactions involving non-heteroatom containing rings.

Table D-4. SAPT0/jun-cc-pVDZ components of $\Delta\Delta E_{int}$(M3) for Entries 1-4, in kcal mol^{-1}.

Entry	Elec	Exch	Ind	Disp	E(SAPT0)
1	-2.7	9.6	-0.3	-7.8	-1.3
2	-1.0	3.7	0.9	-3.4	0.2
3	3.1	-5.4	1.6	5.2	4.6
4	2.8	-4.4	1.5	4.3	4.2

Finally, the importance of dispersion interactions in the energy difference between **TS(3)$_{endo}$** and **TS(3′)endo** can be seen in the NCI Plot figures shown below. There are clearly much more favourably dispersion-driven interactions between the CP and the catalyst in **TS(3)$_{endo}$** than in **TS(3′)endo**.

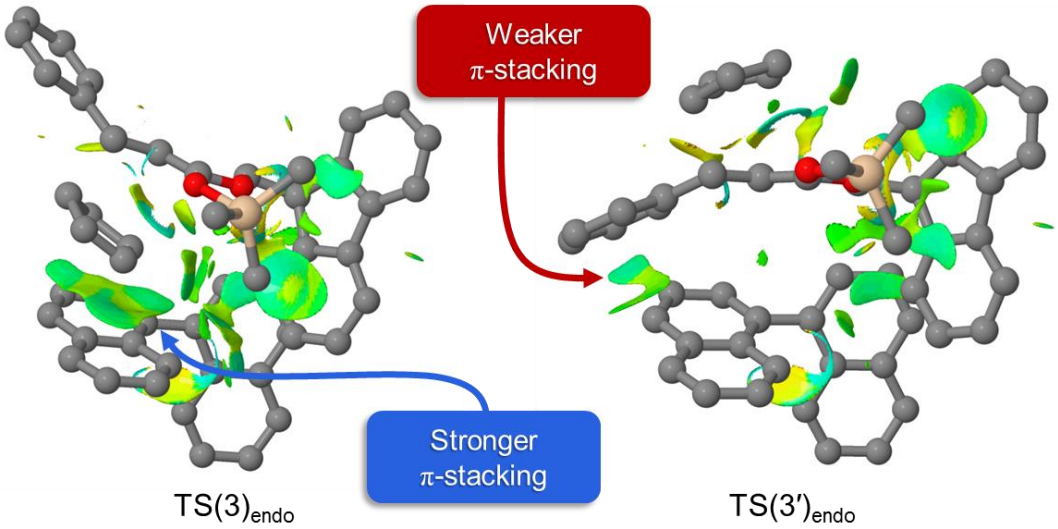

Figure D-3. NCI Plot analysis of **TS(3)$_{endo}$** and **TS(3′)endo** showing a greater stacking interaction between CP and the aromatic catalyst backbone in **TS(3)$_{endo}$**.

For Entry 1, the small value for $\Delta\Delta E^{\ddagger}$, -0.7 kcal mol^{-1}, is due to nearly balanced differences in catalyst distortion energy ($\Delta\Delta E_{cat}$ = 6.1 kcal mol^{-1}) and interaction energy ($\Delta\Delta E_{cat}$ = -6.8 kcal mol^{-1}). The difference in catalyst distortion energy can be traced partially to the difference in energy of the binaphthyl backbones from the M3 models (2.8 kcal mol^{-1}), as well as the anionic catalyst core from the M4 models (1.2 kcal mol^{-1}). The last contribution can be found from different extents of interaction/repulsion

between the bulky CF_3 groups on the aryl groups and the anionic catalyst core. To determine this, the CF_3 groups on the catalyst aryl substituents in both **TS(1)$_{endo}$** and **TS(1′)$_{endo}$** were replaced with hydrogens which were optimized while keeping all other atoms fixed. The difference in catalyst energy then became 4.4 kcal mol^{-1}, implying a contribution to $\Delta\Delta E_{cat}$ involving these CF_3 groups of about 1.7 kcal mol^{-1}. The sum of each of these terms, 5.7 kcal mol^{-1}, nearly equals the difference in energy of the intact catalyst (6.1 kcal mol^{-1}). The difference in interaction energy shows a slightly favourable effect on the selectivity from electrostatic interactions with the catalyst core [$\Delta\Delta$Eint(M4) = 2.3; see Figure 2a in Chapter V for the binding in **TS(1′)$_{endo}$**]. The "core level" electrostatic binding mode of **TS(1)$_{endo}$** is similar to that of **TS(3)$_{endo}$** and **TS(4)$_{endo}$**. In **TS(1′)$_{endo}$**, the substrates appear to engage in more CH···F interactions and less CH···O interactions than in **TS(1)$_{endo}$**. When modifying M4 to a model which replaces each of the CF_3 groups with a hydrogen atom, the interaction energy becomes 3.7 kcal mol^{-1}, implying a contribution to the total interaction energy of -1.4 kcal mol^{-1} due to these groups. More interestingly however, is a modified version of M4 where the terminal SO_2H group nearest the substrates is replaced by a hydrogen atom, which changes the difference in interaction energy to -1.5 kcal mol^{-1}. This implies a contribution to the total difference in interaction energy involving these oxygens of 3.8 kcal mol^{-1}. In other words, superior contact with these oxygens in **TS(1)$_{endo}$**, as CH···O interactions, contributes 3.8 kcal mol^{-1} to the total difference in interaction energy. Similarly to Entries 3 and 4, this suggests that an electrostatic basis contributes to the enantioselectivity involving a difference in overall strength of CH···O interactions,

where the inferior "core level" binding mode can be characterized by an exchange of CH···O interactions for weaker CH···F interactions. However, for Entry 1, the difference in interaction energy with the anionic catalyst core is more than offset by the differences in interaction with the other areas of the catalyst. The π-stacking between the fluorenyl group and the catalyst backbone in **TS(1′)$_{endo}$** is actually stronger than the stacking interaction involving CP in **TS(1)$_{endo}$**, as reflected by $\Delta\Delta E_{int}$(M3), which is -1.9 kcal mol^{-1}. The remainder of $\Delta\Delta E_{int}$ for Entry 1 comes mostly from $\Delta\Delta E_{int}$(M1), which is -5.6 kcal mol^{-1}. The difference in interaction with the other aryl group is only -0.8 kcal mol^{-1} from the M2 model. In **TS(1′)$_{endo}$**, the fluorenyl group of the substrate is oriented perpendicularly to a nearby catalyst aryl group and engages in CH···π interactions. However, the full nature of the interactions with these aryl groups is complicated by the presence of the CF_3 groups. To extract an effect of the CF_3 groups on the interaction energy, M1 and M2 were remade with the CF_3 groups replaced by hydrogens. $\Delta\Delta E_{int}$ for these models then became -4.1 and 1.2 kcal mol^{-1}, respectively. This implies that interactions with the CF_3 groups are more favorable to **TS(1′)$_{endo}$** in the form of CH···F interactions, which are absent in **TS(1)$_{endo}$** because the fluorines are instead facing the aromatic faces of the phenyl and fluorenyl groups of the dienophile and engaging in less favourable lone pair···π interactions.

For Entry 2, the difference in gas-phase energy ($\Delta\Delta E^{\ddagger}$), 1.8 kcal mol^{-1}, consists mostly of a large difference in catalyst energy (-5.0 kcal mol^{-1}) and interaction energy (8.4 kcal mol^{-1}), with also a smaller but significant contribution from the difference in substrate energy (-1.6 kcal mol^{-1}). The relative catalyst energy can be partially sourced to

a difference in the binaphthyl energies from the M3 models (-0.9 kcal mol^{-1}) and the aryl group of the M2 models (-0.6 kcal mol^{-1}). The remaining difference in catalyst energy can be found from differences in intramolecular interactions. The ^{i}Pr groups are apt to interact with the anionic catalyst core by their own CH···X interactions. To probe this, the ^{i}Pr groups of each catalyst were replaced with hydrogens which were optimized while keeping all other atoms fixed. The relative catalyst energy then fell to only -0.1 kcal mol^{-1}. Therefore, the majority of the difference in catalyst energy for Entry 2 is actually due to a difference in intramolecular CH···X interactions involving the ^{i}Pr groups. The large value for $\Delta\Delta E_{int}$, 8.4 kcal mol^{-1}, is partially due to, in **TS(2)$_{endo}$**, favourable CH···π interactions between the phenyl group of the dienophile with a catalyst ^{i}Pr group ($\Delta\Delta E_{int}$(M1) = 3.1 kcal mol^{-1}) and CH···π interactions between the fluorenyl group of the dienophile with another ^{i}Pr group ($\Delta\Delta E_{int}$(M2) = 2.7 kcal mol^{-1}). Though the fluorenyl group is posited similarly in **TS(2′)$_{endo}$** and **TS(1′)$_{endo}$**, it cannot engage in CH···π interactions with the nearby catalyst aryl group in **TS(2′)$_{endo}$**, unlike in **TS(1′)$_{endo}$**, due to being blocked by an ^{i}Pr group. There is stronger electrostatic binding with the anionic catalyst core in **TS(2)$_{endo}$** ($\Delta\Delta E_{int}$(M4) = 2.5 kcal mol^{-1}) for similar reasons to Entry 1, as these two Entries have similar "core level" electrostatic binding modes for the lowest-lying transition states.

Origin of Diastereoselectivity

Table D-5. Gas phase difference in interaction energy for models M1-M4 between the lowest-lying *endo* and *exo* TSs of Entries 1-4, in kcal mol^{-1}.

Entry	$\Delta\Delta E_{int}$(M1)	$\Delta\Delta E_{int}$(M2)	$\Delta\Delta E_{int}$(M3)	$\Delta\Delta E_{int}$(M4)
1	1.3	0.4	-1.7	0.7
2	0.3	-9.8	7.6	-1.3
3	0.0	0.0	-0.1	1.6
4	-0.1	0.1	0.0	2.0

TS(2)$_{exo}$ has a qualitatively different conformation from any of the other structures discussed in Chapter V:

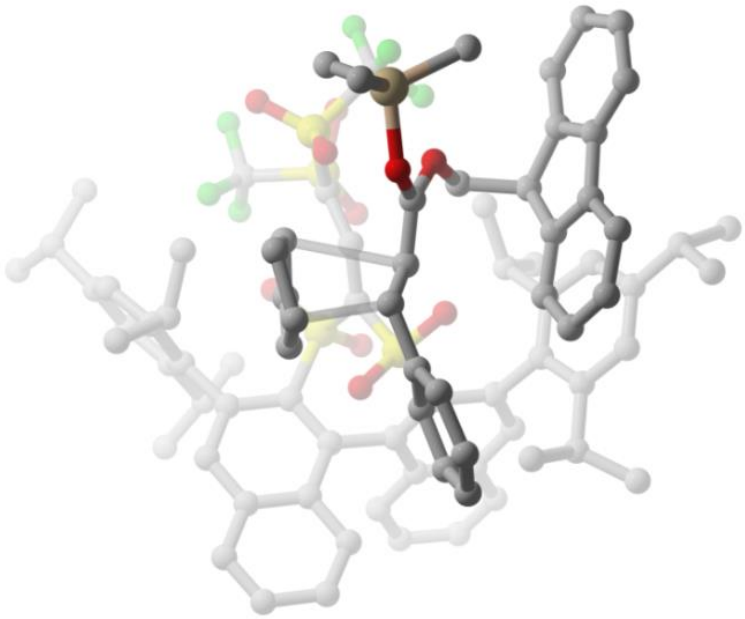

Figure D-4. Lowest-lying TS corresponding to the *exo* adduct of Entry 2, **TS(2)$_{exo}$**.

As shown in Table V-1 of Chapter V, this structure is higher than **TS(2)$_{endo}$** by 2.4 kcal mol^{-1}. The gas phase difference in energy is only 0.6 kcal mol^{-1}, indicating that the free energy difference is mostly due to solvent or entropy effects. The gas phase difference in energy is due to the difference in substrate and catalyst energies ($\Delta\Delta E_{sub}$ = 2.7 kcal mol^{-1} and $\Delta\Delta E_{cat}$ = 2.0 kcal mol^{-1}) being nearly balanced with the difference in interaction energy ($\Delta\Delta E_{int}$ = -4.1 kcal mol^{-1}). The difference in interaction energy is due to the advantageous dispersion-driven interactions of CP with the binaphthyl backbone in **TS(2)$_{endo}$** ($\Delta\Delta E_{int}$(M3) = 7.6 kcal mol^{-1}) being overshadowed, in **TS(2)$_{exo}$**, by stronger dispersion-based CH$\cdots\pi$ and π-stacking interactions of the substrate with the nearby catalyst aryl group ($\Delta\Delta E_{int}$(M2) = -9.8 kcal mol^{-1}) and slightly stronger electrostatic CH$\cdots$X interactions with the negatively charged region of the catalyst ($\Delta\Delta E_{int}$(M4) = -1.3 kcal mol^{-1}).

The next lowest-lying *exo* TS, only 0.3 kcal mol^{-1} higher in energy, is very similar to **TS(2)$_{endo}$** with CP rotated about its plane and rotation of some catalyst ^{i}Pr groups. A comparison between **TS(2)$_{endo}$** and this structure is in the following Table.

Table D-6. SAPT0/jun-cc-pVDZ components of $\Delta\Delta E_{int}$(M3) for Entries 1-4, in kcal mol^{-1}.

$\Delta\Delta E^{\ddagger}$	$\Delta\Delta E_{cat}$	$\Delta\Delta E_{sub}$	$\Delta\Delta E_{int}$	$\Delta\Delta E_{int}$(M1)	$\Delta\Delta E_{int}$(M2)	$\Delta\Delta E_{int}$(M3)	$\Delta\Delta E_{int}$(M4)
2.6	1.2	1.2	0.2	-1.3	-0.1	0.1	1.5

There is a difference in $\Delta\Delta E_{int}$(M4) associated with different strengths of CH$\cdots$O hydrogen bonds due to the CP rotation (1.5 kcal mol^{-1}), though this is largely cancelled

by different strengths of dispersion-based interactions with a catalyst aryl group ($\Delta\Delta E_{int}$(M1) = -1.3 kcal mol^{-1}).